FORCED CONVECTION HEAT TRANSFER IN TWO-DIMENSIONAL RIBBED CHANNELS

FORCED CONVECTION HEAT TRANSFER IN TWO-DIMENSIONAL RIBBED CHANNELS

By

HAMIDREZA MORTAZAVI

B.Sc., M.Sc.

A Thesis

Submitted to the School of Graduate Studies

in Partial Fulfillment of the Requirements

for the Degree

Master of Applied Science

McMaster University

MASTER OF APLLIED SCIENCE (2006) McMaster University

(Mechanical Engineering) Hamilton, Ontario, Canada

TITLE: Forced Convection Heat Transfer in Two-Dimensional Ribbed Channels

AUTHOR: Hamidreza Mortazavi, B.Sc. (Azad University, Tehran, Iran), M.Sc. (Bahonar University, Kerman, Iran)

SUPERVISOR: Dr. Mohamed S. Hamed

CO-SUPERVISOR: Dr. Ehab Elsaadawy

NUMBER OF PAGES: xv , 148

Abstract

The progress of technology in the electronic components industry has been rapidly growing. The evolution of various techniques has made it possible for this industry to grow and diversify with the market demand. Thus, the development of electronic component products over a short span of time requires having highly efficient tools for design and manufacturing. Advances in commercial Computational Fluid Dynamics (CFD) softwares and computational power have enabled modeling to a high level of architectural details. Nowadays, computer aided design becomes an essential design tool in the engineering environment. Computer analysis reduces both the time development cycle and the prototyping costs in the early to intermediate design phases. The accuracy of the computational prediction of heat transfer rates depends mostly on the correct choice of turbulent model. Although many turbulent models, rather than a universal turbulent model, have been developed during the last two decades, there is usually one model that performs better than others for certain flow conditions.

In the present research, a turbulence model is selected from amongst a few candidates, namely standard $k-\varepsilon$, RNG $k-\varepsilon$, shear stress transport (SST), and Reynolds Stress Model (RSM), based on comparisons with experimental data and direct numerical simulation (DNS) results from previous work. The SST turbulence model shows excellent agreement with the DNS results and, hence, is considered an appropriate turbulence model for thermal analysis of electronic packages with elements that have almost the same heights. Moreover, the average Nusselt number of array of obstacles is obtained numerically using commercial code ANSYS-CFX 10.0. The effects upon the mean Nusselt number arising from parameteric changes in Reynolds number, element height, element width, and element-to-element distance are compared and discussed. Finally, the parametric study has offered a set of correlations for the mean Nusselt number of arrays of mounted obstacles in the channel flow.

Acknowledgments

My sincere thanks go to my supervisor, Associate Professor, Dr. M. Hamed. I am very grateful for his advice, guidance, encouragement, kindness and efforts in facilitating my thesis research. I am also very grateful to my co-supervisor, Dr. E. Elsaadawy for his effort in advising my research, and for his constant encouragement and guidance.

Also, I would like to thank the department of mechanical engineering at McMaster University; Professor R. L. Judd , Professor Samir Ziada, Dr. Marilyn Lightstone , Dr. Joseph R. McDermid, Dr. Chan Y. Ching, Professor Brian Latto, Dr. Stephen Tullis, Dr. Sumanth Shankar, and Dr. Saeid Habibi.

Finally, I would like to give an unconditional and appreciative acknowledgment to my family for supporting me through this work.

Table of Content

Chapter Three **Choosing a Turbulence Model**

Chapter Four **Result and Discussion**

List of Figures

List of Tables

Nomenclature

A Channel cross section

A_{top} Top surface area of element

C Clearance height of channel, $C = H - e$

C_p Constant pressure specific heat capacity

D_h Hydraulic diameter, $D_h = 2WH/(W + H)$

e Element height

Gr Grashof number, ratio of buoyancy to viscous forces, $Gr = \beta g \Delta T L^3 / \upsilon^2$

H Channel height, $H = 2\delta$

h Convective heat transfer coefficient, $h = \dfrac{q_c}{(T_w - T_{ref})}$

I Turbulent intensity

K Thermal conductivity of working fluid

k Turbulent kinetic energy

l Turbulent length scale

M Molecular weight of gas

Nu Local Nusselt number, $Nu = \dfrac{h\ H}{K}$

Nu_m Average Nusselt number, $Nu_m = \dfrac{\int_{A_{top}} Nu\ dx}{A_{top}}$

P Pressure

P_{ref} Reference pressure, $P_{ref} = 1\ atm$

P_k Shear production of turbulent

$\bar{P}$ Time average mean component of pressure

Nomenclature-Continued

Pr	Prandtl number, $\mathrm{Pr} = C_p \mu / K$
q_c	Convective heat transfer rate
q_w	Wall heat flux
R_0	Universal gas constant
Re_τ	Reynolds number, $\mathrm{Re}_\tau = \rho u_\tau \delta / \mu$
Re_{Dh}	Reynolds number, $\mathrm{Re}_{Dh} = \rho U_m D_h / \mu$
S_{ij}	Strain rate tensor, $S_{ij} = (\nabla \bar{U} + (\nabla \bar{U})^T)$
S	Absolute value of the strain rate, $S = \sqrt{S_{ij} S_{ij}}$
s	Gap/Distance between two successive ribs (Pitch)
T	Temperature
T^+	Dimensionless temperature, $T^+ = \dfrac{\rho \, C_P \, u_\tau \, (T_w - T)}{q_w}$
T_{inlet}	Inlet temperature
T_{ref}	Reference temperature
T_w	Local surface temperature
U	Velocity
$\bar{U}$	Time average mean component of velocity
u	Turbulent fluctuating component of velocity
u_τ	Friction velocity, $u_\tau = \sqrt{\tau_w / \rho}$
U_c	Centreline velocity of channel
U_m	Bulk mean velocity
U^+	Dimensionless velocity, $U^+ = \overline{U} / u_\tau$

Nomenclature-Continued

W	Width of channel
w	Element stream wise length
X, Y	Cartesian Coordinates
Δy	Distance to the next point away from the wall
y_w	Distance from the wall
y^+	Dimensionless length scale, $y^+ = \rho\, u_\tau y_w / \mu$

Greek symbols

ρ	Density
κ	Von Karman's constant, $\kappa = 0.41$
μ	Laminar dynamic viscosity
μ_t	Turbulent dynamic viscosity
ε	Turbulent dissipation rate
ξ	Unheated length measured from plate edge
δ^*	Displacement thickness, $\delta^* = \int_0^\infty (1 - \frac{U}{U_e}) dy$
δ_{ij}	Kronecker delta, $\delta_{ij} = 1$ if $i = j$ and $\delta_{ij} = 0$ if $i \neq j$
σ_k	Turbulent Prandtl number
β	Gas thermal expansion, $\beta = 1/T$
ν	Kinematic viscosity
ϑ	Turbulent velocity scale
δ	Half of channel height
τ_w	Average wall shear stress on lower ribbed and upper smooth wall
τ_{wall}	Wall shear stress

Chapter One

Introduction, Background, and Literature Survey

1.1 Introduction

The investigation of forced convection in two-dimensional ribbed channels attracts many interests for its wide range of applications, such as electronic cooling, heat exchangers, and nuclear rectors [1]. This study is mainly focusing on the cooling of electronic equipments. Electronics are at the heart of any modern new equipment, and are now so common that we can rarely find any high-technical devices that are fully mechanical. In addition, they are included in the most permeating equipments affecting our everyday life. Electronics is one of the major areas of application of heat transfer technology. Temperature control of electronic equipments has long been investigated, and many advances in reliability, higher power intensity, and physical miniaturization of electronic equipment over the past decades are indebted to thermal control and better thermal design of electronic systems [2]. Based on Moore's law, which was suggested by Gordon Moore, founder of Intel Corporation, semiconductor performance will double every 18 months, and this law has proven valid over the last 25 years. Scientists suggest that this law will continue to be valid for the next 12 to 15 years [3]. Figure 1.1 shows Moore's law trend since 1970 [4].

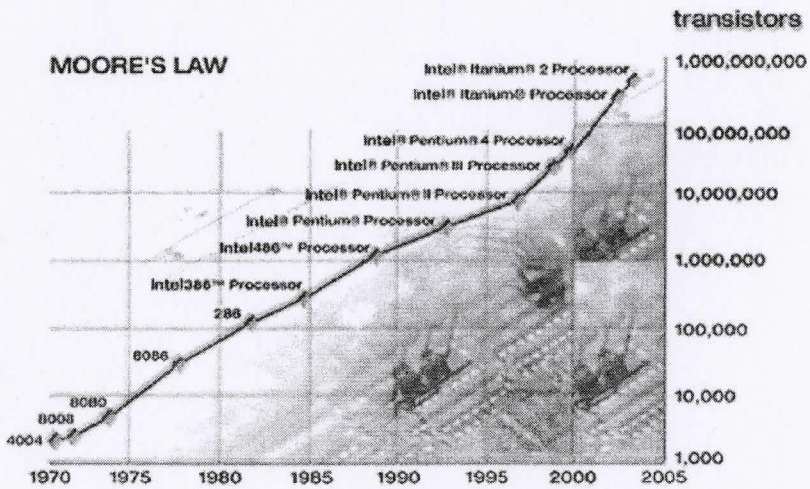

Figure 1.1 Moore's law trend [4]

For many years, cooling technologies have facilitated new discoveries and the advent of modern packaging. Air-cooling has been an important technological approach for its performance, reliability, reasonable cost, space occupation, and low power consumption [5]. Air-cooling technology has gained a top ranking among electronic cooling techniques [3], but the perception is that it has reached its upper limits. An example of this is that the heat fluxes that can be achieved today using air-cooling were achievable in 1980s only by means of liquid cooling [5]. An extension to air-cooling limits concerns many design aspects. Such designs should consider integrated circuit design layout (IC), packaging material development, thermal contact resistance minimizing, heat spreading technologies, aerodynamic fan improvements, air flow optimization, architecture of thermal design, thermal load monitoring, and many others [5]. In electronic equipment, individual devices such as transistors have become more efficient and less heat dissipative. However, advanced circuit and component technologies have miniaturized circuits, so the number of components on a single chip has greatly increased, with the net result that chip intensity has intensified. This development started from small-scale integration (SSI), followed by very-large-scale integration (VLSI), ultra-large-scale integration (USI), wafer scale integration (WSI), and today is continuing to miniaturize electronics [2] and [6]. Figures 1.2 and 1.3 depict the development of such integrations [6] and a typical integrated circuit package (IC), respectively [7].

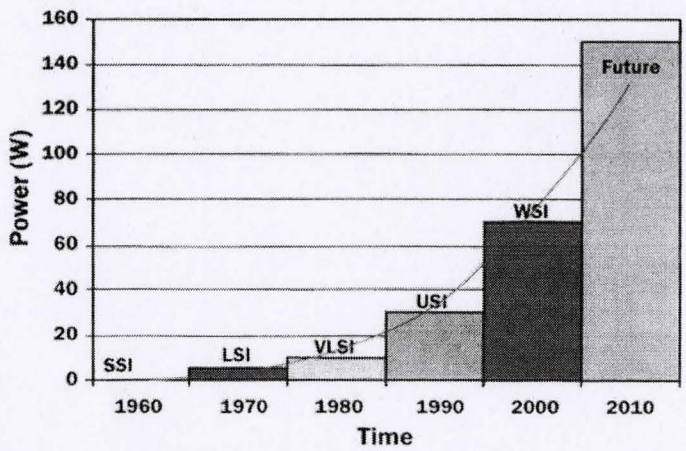

Figure 1.2 Circuit integration development [6]

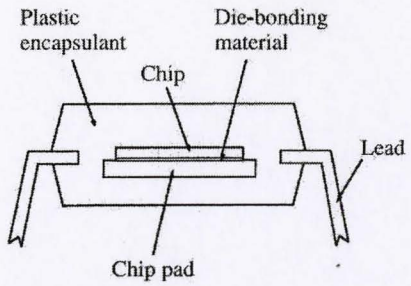

Figure 1.3 A typical integrated circuit package [7]

1.2 Temperature Control Requirement

As our world electrifies, the quality, reliability, and performance of electronics become matters of attention in industries. Better design in electronic cooling systems enhances performance and plays a major role in electronic system reliability. Not only does this concept apply to high-heat-flux electronics but the challenge remains in the field to improve less intense heat fluxes as well. Unanticipated chip temperature of electronic equipment is the key subject of permanent as well as periodic failure in electronic components. Off-limit temperatures lead to excessive strain and cause physical breakdown because of thermo-mechanical stresses. Also, high temperatures are responsible for the weakening of chemical bonds and of wear in electronic components. Figure 1.4 illustrates that uncontrolled temperature in electronic systems is responsible for more than fifty percent of failures in electronics [2].

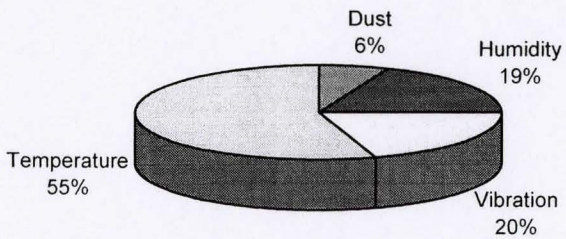

Figure 1.4 Major causes of electronics failure [2]

The typical convective heat transfer coefficient that applies to electronic packaging varies by three orders of magnitudes. This value changes for specific fluids, geometry, and heat transfer techniques. As an example, figure 1.5 shows the convective thermal resistance of a typical 10 cm^2 heat source for a variety of coolants and techniques, in which velocity ranges from 2 to 8 m/s [7].

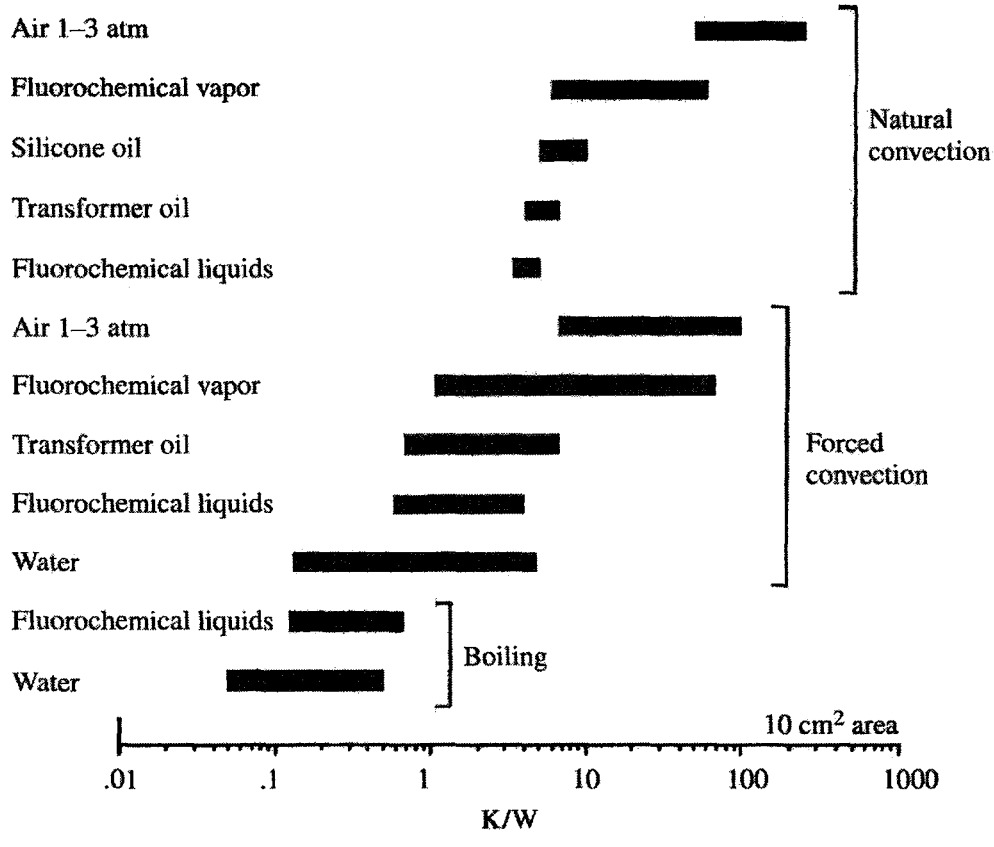

Figure 1.5 Convective thermal resistance ranges applied in electronic packaging [7]

1.3 Motivation

Computer analysis reduces both the time development cycle and the prototyping costs in the early to intermediate design phases [8]. Heat transfer and flow field in

electronic cooling are simulated by predicting turbulent phenomena and wake of electronic components [9]. From the simulation viewpoint, geometric modeling of problems has become simpler by integrating printed circuits into a single module as a heat source. But the sensitivity and complexity of appropriate modeling to obtain accurate predictions of heat and flow fields has intensified the problem [10]. Thus selecting an appropriate method to model flow and heat transfer is vital for simulating electronic packages.

1.4 Computational Modeling

Thermal management in electronics requires an understanding of heat transfer phenomena and of the aerodynamic impacts of flow on electronic cooling. The ability to accurately predict wall shear stress and heat transfer rate in the vicinity of solid surfaces (walls) depends largely on the correct choice of turbulent model. When it comes to electronic cooling and commercially available thermal management packages, researchers disagree about which turbulence model captures best the physics of such problem. This point is an obvious deduction from past works, such as that of Yang et al. [11], who researched two-dimensional channel flow over one and two mounted surface obstacles with a uniform velocity profile at the inlet and fully developed condition at the outlet. This study also used a wall function to bridge the viscous sublayer. Results from this research are obtained with the well-known $k-\varepsilon$ turbulent model in the Reynolds number range of 10^4 to 10^6 based on hydraulic diameter ($D_h = 2H$), and have good agreement with experimental data. Yang et al. concluded that as the integrated circuit volume becomes less in the future, a turbulent flow field should be considered for better performance in cooling an electronic system. In 1998, Behnia et al. [10] performed a set of computational fluid dynamics (CFD) investigations to imitate heat transfer from heated modules in an air stream using commercial code FLUENT. These investigations have been compared with experimental results of other works and discuss solutions of uniform

and fully developed velocity profile at channel entrance, where the mean velocity was varied from 1 to 7 m/s. This study has employed second order accuracy in discretization of convective terms. It reports that $k-\varepsilon$ and RNG $k-\varepsilon$ turbulent models show no significant difference from each other and that the use of a wall function is not suitable with these models. Also, results from their investigation show that the choice of inlet velocity profile has an impact on the predicted average heat transfer coefficient. The authors emphasize that fully developed velocity profile yields better results (especially at high Reynolds numbers). In the same year, Young et al. [12] conducted a two-dimensional numerical parametric study in a channel containing multiple heated blocks. This laminar forced convection study has involved obstacle height, width and spacing, number of obstacles, obstacle thermal conductivity ratio, flow rate, and heating method of obstacles. The study assumes that all channel walls to be adiabatic with the exception of obstacles, and has varied the Reynolds number based on hydraulic diameter ($D_h = 2H$) in the range of 200 to 2000. The parametric study of Young et al. highlights that surface heat flux and uniform volumetric heat generation have negligible effect on the average Nusselt number of an individual obstacle. Moreover, obstacle width increase is reported to have a decreasing effect on the top surface average Nusselt number, contrary to obstacle spacing. In addition, shorter obstacles account for higher top surface average Nusselt numbers, with the exception of the first row. Later, V. Eveloy et al. [13] investigated the flow and heat transfer field of a single and multi-component printed circuit board (PCB) using the FLOTERM CFD commercial package. In the absence of a proper length scale to determine the flow regime, their research has considered solutions of both the laminar and the turbulent model for the 2 m/s forced convection problem. They report that laminar, Zero- (LVEL), and $k-\varepsilon$ models are incapable of capturing accurately the heat and flow field in detail over the entire multi-component PCB. Interestingly, energy balance on a single component was found to be independent of the applied model, whereas in the multi-component model, heat transfer balance due to component interactions was found to be sensitive to the model. Bredberg et al. [14] have conducted similar investigations to examine the effectiveness of two-equation turbulent

models, specifically $k-\varepsilon$, $k-\omega$, and two-layer or zonal models. This study has been compared with experimental data according to two high Reynolds numbers of 40,000 and 100,000, and the conclusion is that both $k-\varepsilon$ and $k-\omega$ turbulent models have reasonable accuracy in predicting heat transfer, whereas in contrast, the zonal $k-\varepsilon$ model lacks accuracy. Also, all selected models have shown that the Nusselt number has high dependency on Reynolds number, and that this dependency is higher in equilibrium flows and lower in separated flows. In another study, Low et al. used a commercial CFD code FLUENT to compare heat transfer coefficient profiles of flat, interrupted, and ribbed heated surfaces in a two-dimensional channel flow. This research at the inlet uses one-seven-power law turbulent velocity profile for a fixed Reynolds number, $\mathrm{Re}_H = 194000$, and employs a non-equilibrium wall function. Results from this research have been compared with different turbulent models such as the Standard, Realizable, and Renormalized-Group (RNG) $k-\varepsilon$ models, and the Reynolds Stress Model (RSM) [15]. In its mesh structure, this study considers a y^+ value of 25 and concludes that when same grid size is used, all $k-\varepsilon$ and RSM models show consistent results, unlike Spalart-Allmaras and Large Eddy turbulent models. On the other hand, Eveloy et al. [8] and [16], who studied under commercial code FLOTHERM, have questioned the current capabilities of CFD packages as a design tool. This study sought a turbulent model that could capture the physics of a PCB-mounted component heat transfer for free stream velocities of 2 to 4 m/s, and they have considered turbulent models such the algebraic mixing length model, LVEL, and $k-\varepsilon$ turbulent models. Eveloy et al. suggest that Reynolds Average Navier Stokes (RANS) based models are unlikely to be replaced by Large Eddy Simulation (LES) or Direct Numerical Simulation (DNS) in design environments in the foreseeable future. Also, other two-equation eddy viscosity turbulence models should be considered for implemention in CFD codes. In addition, the use of wall functions is inappropriate for flows containing separation, reattaching, or recirculating conditions. Similarly, Dhinsa et al. [9] have discussed the capabilities of zero-equation models such as LVEL, LVEL CAP, Wolfshtein first equation model, and of two-equation models such as $k-\varepsilon$, $k-\omega$, SST, and $k\varepsilon/kl$ turbulent models, to

predict heat and fluid flow in electronic packages. This investigation has been carried out under CFD commercial code PHYSICA and has compared its results with experimental data. Then, the high Reynolds standard $k-\varepsilon$ turbulent model was introduced to struggles for an accurate prediction even for simple cases, and other models under investigation are reported to give better results, although no model has been deemed the clear winner. In addition, their case study of flow over a surface mounted cube body is reported to have a separation of boundary layer on the sides (side vortex recirculation tube), and top surface (bound recirculation), an arc-shaped vortex at the downstream face, and a horseshoe vortex in the windward face. Figure 1.6 shows these vortices around such a cube. It has been concluded that the electronic failure is due to these recirculation areas since they trap heat and restrict further heat from escaping the system.

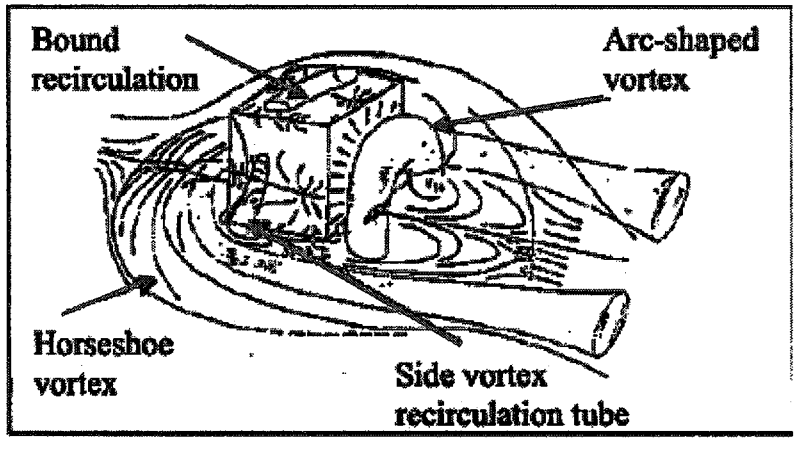

Figure 1.6 Schematic of the flow field around a cube [9]

Another investigation has foreseen that RANS modeling of low-Reynolds turbulent models in electronic applications will remain the realistic engineering approach in modeling electronic cooling [17]. Also, the Reynolds Stress Model (RSM), Large Eddy Simulation (LES), and Direct Numerical Simulation (DNS) are considered unpractical for engineering applications because of their high computational cost (Year 2004). This study

has used the FLUENT solver to examine the predicted accuracy of three low-Reynolds turbulent models: Two-Layer Zonal model, Spalart-Allmaras (SA), and Shear Stress Transport (SST). Standard wall function and non-equilibrium wall function (flow with separation and reattachment) are discussed in this study as being inappropriate and not intended for low Reynolds number flows. The Two-Layer Zonal model temperature predictions are shown to be lower than those for SST and SA. But encouragingly, the SST model is reported to predict component junction temperature within $\pm 3^{\circ}C$ (5%) of measurements. In addition, SA model performance is evaluated as being comparable to SST as an alternative with lower computational cost. On the other hand, Dhinsa et al. [18] in December 2005 reported an investigation under commercial CFD code PHYSICA on the appropriateness of the zero-equation LVEL, the one–equation Wolfshtein, the two-equation $k-\varepsilon$ and $k-\omega$, and the hybrid $k\varepsilon-kl$ and SST turbulent models in electronic applications. These results, when compared with experiment data, reveal that although the SST model from the literature on electronic cooling applications has received good reviews, it has poor flow recovery in the wake region. The SST model has also been reported to show some difficulty with high aspect ratio obstacles. Notably, no turbulent model was found to be the clear winner in investigating the simple case of a single heated cube in the channel flow. Following the previous work, Lou et al. [19] examined the capabilities of the standard $k-\varepsilon$ and RSM turbulent models in a rectangular cross sectional ribbed channel flow. The flow in this study was fully turbulent ($22{,}000 \le \mathrm{Re}_{Dh} \le 94{,}000$), and the channel was provided with eight ribs along the bottom wall, where a uniform heat flux was applied. Also, the geometric configuration of the problem was fixed at $s/e = 2$, $e/D_h = 0.25$, and $w/e = 2$. This investigation concluded that the standard $k-\varepsilon$ turbulent model is able to give better Nusselt profile prediction than the RSM model, but both models are reported to underpredict their values. This superiority is emphasized to be true, especially downstream of the rib.

1.5 Experimental Work

Even computational work in electronic cooling applications requires a considerable amount of resource, and it is time-consuming when done in detail, as is the required tedious work for experimental investigations. An example of such attempt is the work of McEntire et al. [20], who investigated local forced convective heat transfer coefficient of an array of four discrete heat sources, $q"=850\ w/m^2$, with a two-dimensional flush and protruding concept. Their investigation takes into account three different element heights, $0 \le e\ [mm] \le 127$, two different channel clearance heights, $C=(H-e)=0.635$ and $127\ [mm]$, with a fixed stream-wise element spacing, $s=127\ [mm]$. This experiment has been performed only for air in the Reynolds range of 1000 to 10,000, based on hydraulic diameter. Results from this work suggest that the buoyancy factor is negligible. In other words, flow and heat transfer fields are deemed to be forced-convection dominant. The study by McEntire et al. show that the heat transfer characteristics on the first heater have a complex dependency on Reynolds number and, thus, the authors omitted the first heater results in obtaining any correlation for convective heat transfer coefficient. Equation 1.1 is obtained based on their work for average Nusselt number, with an average associated error of 8.4%. The study reports protrusion and less channel clearance area, C, to have a favourable effect of heat transfer rate because of thermal boundary layer interruptions and evolution of flow from transition to turbulence. Flow visualizations show that this phenomenon first occurs at about $\mathrm{Re}_{Dh} \approx 2000$, Figure 1.7.

$$Nu_w = 0.244\,\mathrm{Re}_{Dh}^{0.61}\left(\frac{(H-e)}{w}\right)^{-0.40}\left(\frac{e}{w}\right)^{0.10} \tag{1.1}$$

where

$$T_{ref} = T_{inlet},\ 2000 \le \mathrm{Re}_{Dh} \le 10{,}000,\ 0.5 \le \left(\frac{(H-e)}{w}\right) \le 1.0,\ \text{And}\ 0.5 \le \left(\frac{e}{w}\right) \le 1.0$$

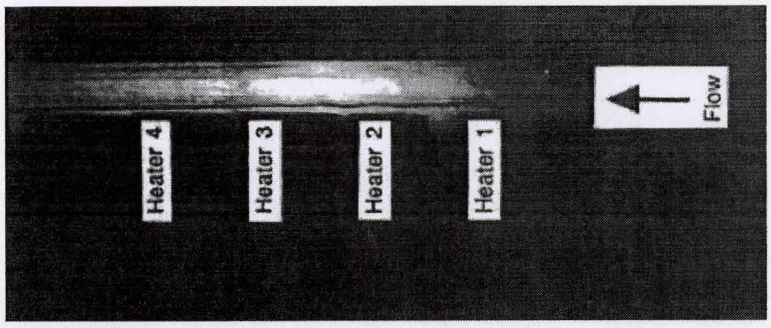

(a) $\mathrm{Re}_{Dh} = 1000$

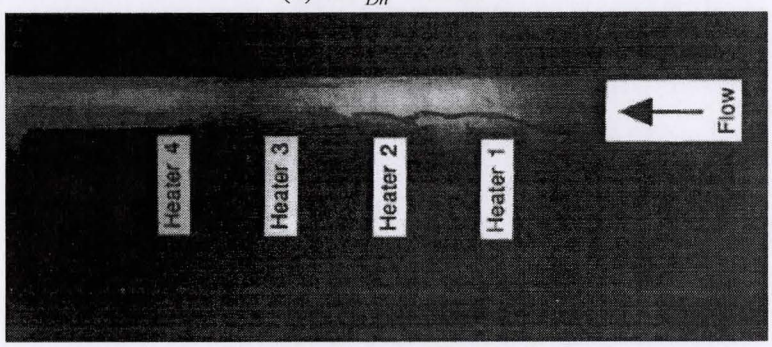

(b) $\mathrm{Re}_{Dh} = 2000$

Figure 1.7 Flow visualization past discrete heat sources in a ribbed channel with $s = w,\ \frac{e}{w} = 0.5,\ and\ \frac{(H-e)}{w} = 1$ [20]

In a later work, Hacohen et al. [21] studied the forced and free convection of various channel heights, component heights, flow rates, and applied heat fluxes. The study represents two theoretical upper and lower limits for free and forced convection in a channel that thermally and hydrodynamically developing is similar to a printed circuit board. The upper theoretical average Nusselt number limit for turbulent forced convection is formulated from a constant temperature plate where thermal and hydrodynamic boundary layers start from the edge of the plate. The lower band of the theoretical average Nusselt number limit for turbulent forced convection is calculated by numerically integrating the local heat transfer coefficient at a constant flow rate with unheated starting

length, x_0. Lower and upper theoretical expressions are given by equation 1.2 and 1.3, respectively. Figure 1.8 shows the corresponding geometry. The measured values in this study confirm that this theory holds to be valid for the conducted experiments.

$$Nu_x = 0.0287 \mathrm{Re}_x^{0.8} \mathrm{Pr}^{0.6} \left[1 - \left(\frac{x_0}{x} \right)^{9/10} \right]^{-1/9} \qquad \text{Lower Limit} \qquad (1.2)$$

$$Nu_m = 0.036 \mathrm{Re}_L^{0.8} \mathrm{Pr}^{1/3} \qquad \text{Upper Limit} \qquad (1.3)$$

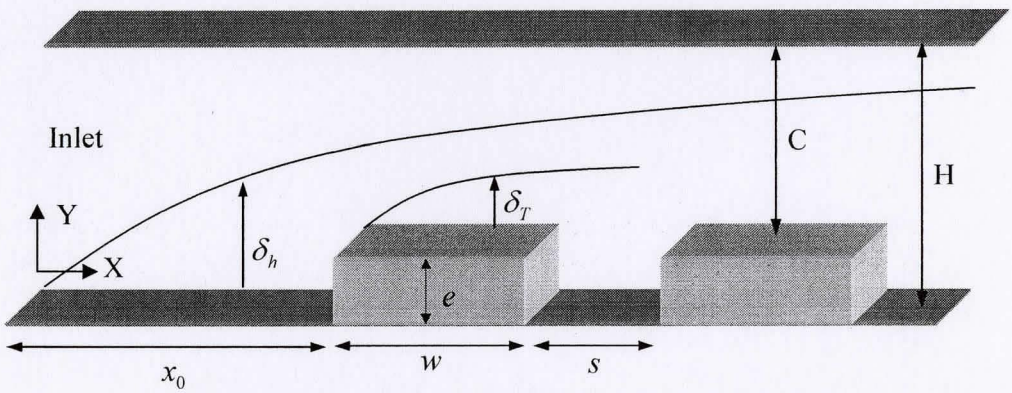

Figure 1.8 Geometry corresponding to equation 1.2

Another experimental work by Jubran et al. [22] explored the effect of the size of modules and missing modules on the performance of imitated electronic components, in which the Reynolds number ranged from 1690 to 2625 based on module stream-wise length. It was found that in an array of obstacles, the rectangular modules tend to improve heat transfer by as much as forty percent over that of square modules. Also, heat transfer is reported to improve up to thirty-seven percent on the subsequent missing module. Leung et al. [23] reported an experimental work which has investigated an electronic printed circuit board by examining periodic rectangular ribs in a channel flow. This

research performed a parametric study on channel height, rib height ($H/e = 2$,4 ,6 ,and 8), and rib width ($w/e = 3$, and 4) in both the vertical and horizontal orientation of the channel. The twelve-array ribs, uniformly spaced $s = 6.35$ [mm], are on one principal channel wall, and the Reynolds number varies from 510 to 2050 based on clearance length above the ribs. In an analysis of convective heat transfer coefficient, Leung et al. have adopted a linear change in channel temperature, T_{adopt}, from inlet to exit, and have suggested the following expressions for the average Nusselt number based on clearance length, shown in equations 1.4 and 1.5, which depict the correlations for horizontal and vertical channel orientations, respectively. The study concludes that a choice of flat rib with a larger top surface is the more appropriate option since it enhances heat dissipation. This also could be inferred from the following equations:

$$Nu_C = 0.40\,\mathrm{Re}_C^{0.42}\left(\frac{H}{e}\right)^{0.68}\left(\frac{w}{e}\right)^{0.80} \tag{1.4}$$

$$Nu_C = 0.12\,\mathrm{Re}_C^{0.29}\left(\frac{H}{e}\right)^{0.78}\left(\frac{w}{e}\right)^{1.35} \tag{1.5}$$

where

$$T_{ref} = T_{adopt},\ 460 \le \mathrm{Re}_C \le 2300,\ 3 \le \frac{w}{e} \le 4,\ \textit{and}\ 2 \le \frac{H}{e} \le 10$$

Wang et al. [24] investigated in a parametric study the effects of flow rate ($1500 \le \mathrm{Re}_{Dh} \le 6300$) and element height ($0 \le e/H \le 0.805$) in electronic equipments. This study considered an array of four elements in a channel with uniform constant heat flux. The investigation of flush and protruding obstacles revealed that free convection plays an important role in the underlying physics when dealing with flush-mounted discrete heat sources, but it can be ignored in protruding cases when the Reynolds number exceeds 1500. It is noteworthy that for the same flow rates and applied heat fluxes,

element protrusion results in a higher heat transfer rate for each heater. Similarly, an increase of Reynolds number is reported to have an increasing effect on the heat transfer rate for each element height aspect ratio, e/H. Wang et al. have attributed the difference of two Nusselt numbers in flush and protruding cases to distortion in the flow due to the presence of protruding blocks and small separated regions above the heater surface. But an exception to the above trend in the average Nusselt number has been reported for protruding heat sources at Reynolds number of 1200 and 1600. In this range, the average Nusselt numbers for all heat sources have higher values at Reynolds number of 1200 than 1600. This range is suggested to be the critical Reynolds range in which transition from laminar to turbulent flow occurs in a rectangular channel with protruding heat sources. In other words, turbulent intensity has increased drastically and, thus, the average Nusselt number is elevated. Moreover, the spatial occurrence of maximum and minimum average Nusselt number is associated with different locations and with shape of separated regions that might change with Reynolds number, and with protruding height from one heater to another. Wang et al. have formulated an empirical relationship between the studied parameter for protruding cases in which flow is considered exceeding laminar Reynolds number, $1500 \leq \mathrm{Re}_{Dh}$. Equation 1.5 represents this correlation for average Nusselt number, and table 1.1 shows the corresponding values.

$$Nu_w = A\,\mathrm{Re}_{Dh}^{\;B} \tag{1.5}$$

where $T_{ref} = T_{bulk}$

Table 1.1 Data values of equation 2.5 [24]

e/H		0.151	0.327	0.503	0.654	0.805
Heater 1	A	0.648	0.336	0.972	1.791	0.952
	B	0.500	0.629	0.526	0.474	0.581
Heater 2	A	0.532	0.630	1.095	1.722	1.121
	B	0.537	0.547	0.503	0.475	0.575
Heater 3	A	0.701	0.646	0.890	1.138	0.851
	B	0.491	0.538	0.522	0.519	0.594
Heater 4	A	0.676	0.494	0.603	0.991	0.987
	B	0.503	0.582	0.581	0.545	0.583

In 1999, Young et al. [25] studied the preceding experiments and conducted a more comprehensive investigation. This investigation has included the effect of air flow rate ($800 \le \mathrm{Re}_{Dh} \le 13000$), channel height, array configuration, and input heat flux ($950 \le q'' \le 20200$). The study concerns an array of two-dimensional forced convection, and has obtained a set of correlations for protruding obstacles. Equation 1.6 defines this expression for average Nusselt number of an array of five obstacles, in which the studied parameters are fixed as follows: $\frac{e}{w} = 0.89$, $\frac{s}{w} = 1.0$, $\frac{H}{w} = 1.57$, *and* $q'' = 3750\ w/m^2$. Table 1.2 summarizes the values in equation 1.6.

$$Nu_H = A\,\mathrm{Re}_{Dh}{}^{B} \tag{1.6}$$

Table 1.2 Data values of equation 2.6 [25]

Parameters / Reynolds Number Range		*A*	*B*
Heater 1	2600-4300	0.1262	0.699
	5000-13000	0.0140	0.940
Heater 2	2600-4300	0.2701	0.605
	5000-13000	0.0672	0.746
Heater 3	2600-4300	0.1028	0.703
	5000-13000	0.0212	0.860
Heater 4	2600-4300	0.1339	0.661
	5000-13000	0.0244	0.833
Heater 5	2600-4300	0.1661	0.632
	5000-13000	0.0338	0.794

The work of both Wang et al. and Young et al. show the predicted critical range of Reynolds number to be different. This range is predicted to fall in the range of $500 \leq \mathrm{Re}_{Dh} \leq 2{,}000$ in the first work, and $3{,}800 \leq \mathrm{Re}_{Dh} \leq 4{,}400$ in the second work. This difference is suggested to be as a result of different geometric parameters of the test section and applied boundary condition [24].

Later, Chen et al. [26] conducted an investigation to determine an optimum spacing between obstacles in cooling electronic package applications. This two-dimensional investigation assumes five identical uniformly heated square obstacles with different side-to-side arrangements. The convective heat transfer coefficient in this investigation is based on a linear variation in the channel temperature from entrance to the exit, T_{adopt}. The experimental research concludes that conventional equally spaced arrangements between obstacles do not follow an optimum heat transfer rate in electronic package applications. Furthermore, it is found that when the side-to-side ratio, $\frac{S_n}{S_{n+1}}$, is below a critical limit and follows a geometric series pattern, heat is removed more efficiently until it reaches its optimum critical side-to-side ratio value. Interestingly, when the side-to-side ratio is increased further, the heat transfer rate is reported to decrease.

Finally, experimental work by Yoo et al. [27] in the Reynolds number range of 1.29×10^4 to 3.87×10^4 (based on channel height) has examined the local heat transfer coefficient in both two-dimensional and three-dimensional module arrays. The two-dimensional module array data showed a little lower value than the three-dimensional results, as a result of bypass flow. This difference is reported to decrease with less longitudinal module spacing. In this study, the local heat transfer coefficient profile distribution is shown to be unaffected by variation in the module stream-wise spacing. And on the third row, where flow is assumed to have a fully developed behaviour, the variation trend of the local Nusselt number is the same for different velocities, with the exception of the top surface where the local Nusselt number decreases gradually as the boundary layer thickens.

1.6 Conclusion

The current literature is mainly focusing on the cooling of electronic packages. The review has explored the progress, shortage, and requirement of the electronic cooling pathway, where further developments could lead the electronic industry to design better systems. Many available industrial-purpose commercial CFD codes have implemented various turbulent CFD models to satisfy different industrial needs. Although some models have shown a breakthrough in electronic cooling, this model is yet to come. Indeed, CFD modeling is still in search of a universal turbulent model applicable to electronic cooling applications. In addition, not all data from the literature come to the same conclusions. These outcomes are usually valid for a certain band of Reynolds number, and do not apply as a general rule. Thus new turbulent models applicable should be carefully examined and tested before applying in industrial applications.

It is noticed that classic electronic cooling problems found in the literature have always omitted some of the underlying parameters. Perhaps the explanation is that incorporating more parameters rapidly raises the combination of all possibilities. In most electronic

cooling applications the free stream velocities range from 2 to 4 m/s, which represent mid- to high-range free stream airflows employed [8]. As the electronic industry tends toward miniaturization even on passage flow and casing, based on the above velocity values no such attempt has been conducted to investigate the basic geometric parameters within the turbulent range.

The objective of the present work is to discover the most appropriate turbulent model that can capture both the heat transfer and flow field characteristics in electronic cooling and use it to investigate the influence of geometric parameters on the nature of flow and heat transfer in a typical classic electronic cooling problem.

Chapter Two

Mathematical Modeling

2.1 Geometry and Computational Domain of Parametric Study

Two parallel plates form the geometry of the present parametric study, and flow has been allowed through this passage. The lower plate has five identical square ribs of height e, length w, and distance s between two successive ribs. The upper plate is smooth, and the two plates are a distance H (channel height) apart. In presenting results, all geometric dimensions have been normalized with respect to channel height to provide a clear contrast and comparison between different cases. Figure 2.1 shows the geometry of the present parametric study.

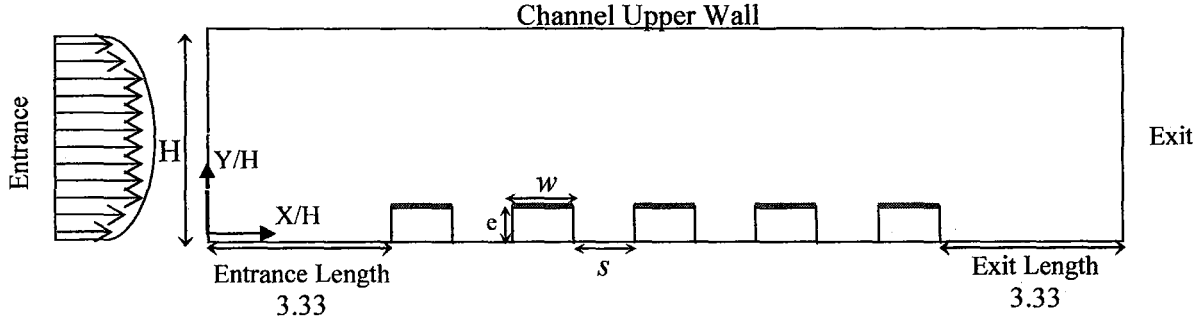

Figure 2.1 Geometry of the Parametric Study

2.2 Governing Equations

In this investigation, air is selected as the cooling medium, which is assumed to be a non-buoyant incompressible[1] ideal fluid. The governing equations are the ideal gas equation of state, the continuity equation, the time-averaged Navier-Stokes, and the energy equations in stationary and steady state conditions given by equations 2.1, 2.2, 2.3,

[1] By incompressible we mean that pressure and density are not linked, but there is no prior assumption that density is constant or that it cannot be function of temperature.

and 2.4, respectively. In governing equations, advection terms are discretised using a second order upwind scheme, which handles numerical diffusion more appropriately. Also, convergence criteria for governing equations are selected as the root mean square of residuals, RMS, which is the imbalance of each conservative control volume equation. This criterion is set to the target value of 1.0E-6, which is suggested for academic interest [28] [29].

$$\rho = \frac{P}{RT}, \; R = \frac{R_0}{M} \tag{2.1}$$

$$\frac{\partial \rho \bar{U}_i}{\partial x_i} = 0 \tag{2.2}$$

$$\frac{\partial}{\partial x_j}\left(\rho \; \bar{U}_i \; \bar{U}_j\right) = \frac{\partial \bar{P}}{\partial x_i} + \frac{\partial}{\partial x_j}\left[\mu\left(\frac{\partial \bar{U}_i}{\partial x_j} + \frac{\partial \bar{U}_j}{\partial x_i}\right) - \rho\overline{u_i u_j}\right] \tag{2.3}$$

$$\frac{\partial}{\partial x_j}\left(\rho \; \bar{U}_j \; T_i\right) = \frac{\partial}{\partial x_j}\left(\left(\frac{\mu}{\mathrm{Pr}} + \frac{\mu_t}{\mathrm{Pr}_t}\right)\frac{\partial T_i}{\partial x_j}\right) \tag{2.4}$$

In equation 2.4, Prandtl number, Pr, is a fluid property and the turbulent Prandtl number, Pr_t, is set to a constant value of 0.9 [30].

2.3 Boundary Conditions of Parametric Study

The present work studies the classic problem encountered in electronic cooling applications, in which populated heated blocks represent electronic components mounted

on a printed circuit board (PCB). A two-dimensional domain was studied using the commercial CFD code ANSYS-CFX 10.0 [28] to investigate the flow and heat transfer with the following boundary conditions.

2.3.1 Inlet Boundary

The flow is assumed fully turbulent with a fully developed velocity profile at the entrance to the channel. This velocity profile is introduced by well known one-seventh-power-law velocity profile, equation 2.5 [15]:

$$\frac{U}{U_c} = \left(2y/H\right)^{1/7} \tag{2.5}$$

Where

$$\frac{U_m}{U_c} = 0.817 \tag{2.6}$$

In addition, turbulent quantities, such as kinetic energy, k, and dissipation rate, ε, are assumed to be convection-dominant. In other words, the diffusion is assumed to be negligible. These quantities are computed by applying one percent turbulent intensity, $I = 1\%$, at the inlet, and are defined as follows [28]:

$$k_{inlet} = \frac{3}{2} I^2 U^2 \tag{2.7}$$

$$\varepsilon_{inlet} = \rho\, C_\mu\, \frac{k^2}{\mu_t} \tag{2.8}$$

$$\mu_t = 1000\ I\ \mu \tag{2.9}$$

in which C_μ is a constant. Also, the turbulent stress tensor is assumed to have an isotropic attribute at this location, and its components are calculated according to equation 2.10 and 2.11 [28]:

$$u_x u_x = u_y u_y = u_z u_z = \frac{2}{3}k \tag{2.10}$$

$$u_x u_y = u_x u_z = u_y u_z = 0 \tag{2.11}$$

A uniform temperature profile is assumed at inlet with

$$T_{inlet} = T_{ref} = 25^o C \tag{2.12}$$

Figure 2.2 compares turbulent quantitative values at the entrance. Very close to the wall, viscosity effects dampen fluctuations, and in the outer region, kinetic energy is produced because of large velocity gradients, which, in turn, augment turbulence. Figure 2.3 shows this augmentation over the ribs for a typical case study.

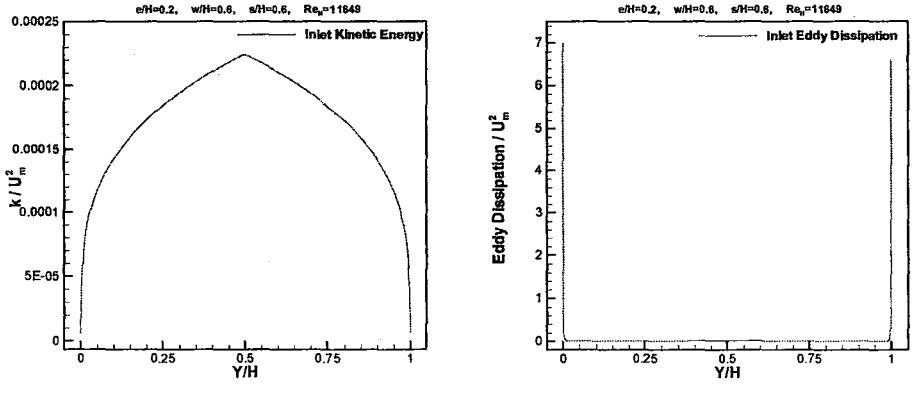

Figure 2.2 Turbulent kinetic energy and eddy dissipation at entrance boundary

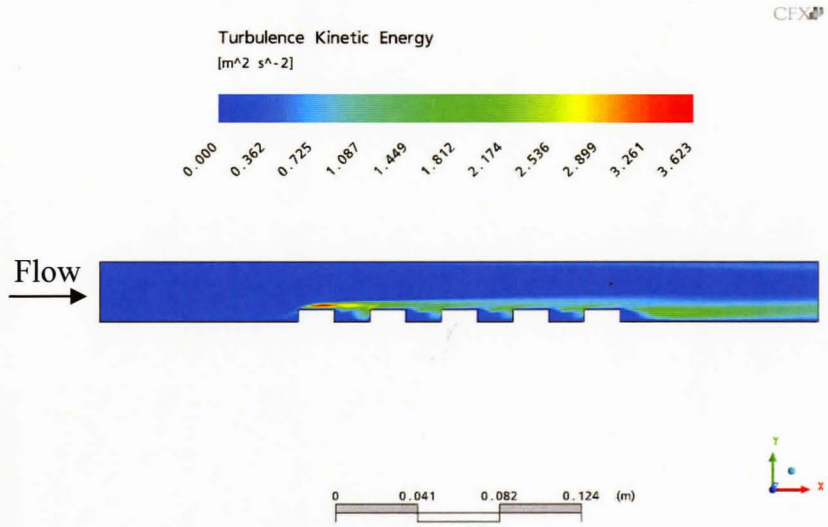

Figure 2.3 Turbulent kinetic energy over the five ribs of the parametric study $e/H = 0.2, w/H = 0.6, s/H = 0.6, \mathrm{Re}_H = 11649$

2.3.2 Exit Boundary

At the exit, the flow field is provided with a uniform static pressure at this location. Its value is assumed to be atmospheric, equation 2.13. Figure 2.4 compares turbulent quantitative values at the exit (SST model).

$$P = P_{ref} = 1 \ atm \tag{2.13}$$

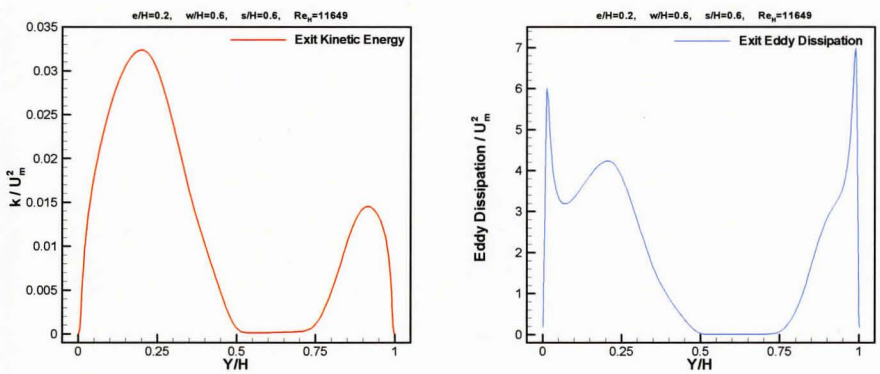

Figure 2.4 Turbulent kinetic energy and eddy dissipation at exit boundary

2.3.3 Wall Boundary

All walls in the channel are assumed to be adiabatic, with the exception of the top rib surface, where a constant uniform heat flux of 5000 W/m^2 is applied. In addition, at all walls the velocity of the fluid is set to zero, no slip condition. In turbulent flows, an important key subject for accurate predictions of wall shear stress and the wall heat transfer is the treatment of flow close to the wall. This treatment is usually provided either by considering the wall function or by employing a low-Reynolds number model close to this region.

In the wall function approach, it is assumed that flow close to the wall acts like a fully developed turbulent boundary layer. In this condition, the production term and dissipation term are dominant in the log-law region, $(30 < y^+ < 100)$. The convection term and diffusion term are ignored [29]. In the wall function approach, the first node adjacent to the wall should fall within the logarithmic region, where inertial and molecular viscous terms are negligible [32], and flow between this point and the wall is bridged by means of an empirical correlation. In other words, wall function ignores the influence of the inner region (laminar sublayer and buffer layer) on the development of a boundary layer.

The main disadvantage of such an approach is that results are sensitive to the near wall meshing. This is especially true in low Reynolds number flows since the logarithmic layer thickness decreases so placing the first grid node within the logarithmic layer becomes more difficult. But on the other hand, wall functions help to save time and resources. Figure 2.5 shows the log-law layer extent for low and high Reynolds number flows [30].

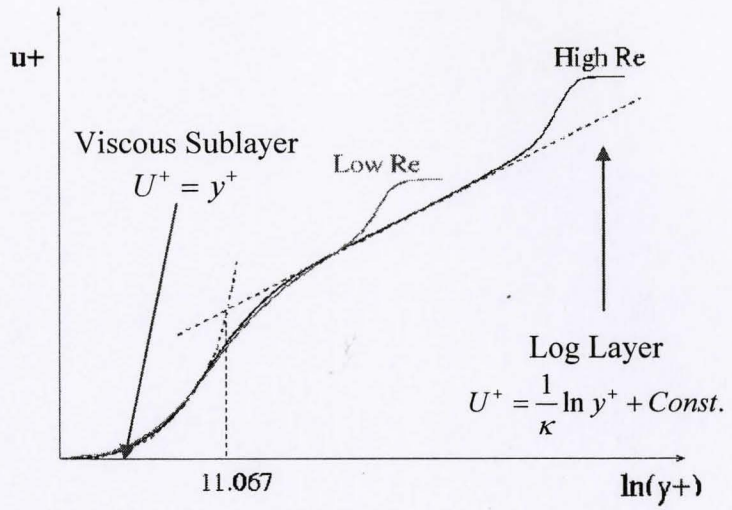

Figure 2.5 Log layer in a fully turbulent velocity profile
for low Reynolds and high Reynolds number [30]

In the alternative approach, grids are chosen sufficiently fine at the wall region, and the turbulent models close to this region are adjusted and modified to solve the flow field all the way down to the wall. These modified models are termed low-Reynolds number turbulent models, in contrast to high-Reynolds number turbulent models that use a wall function [29]. Figure 2.6 illustrates these two approaches.

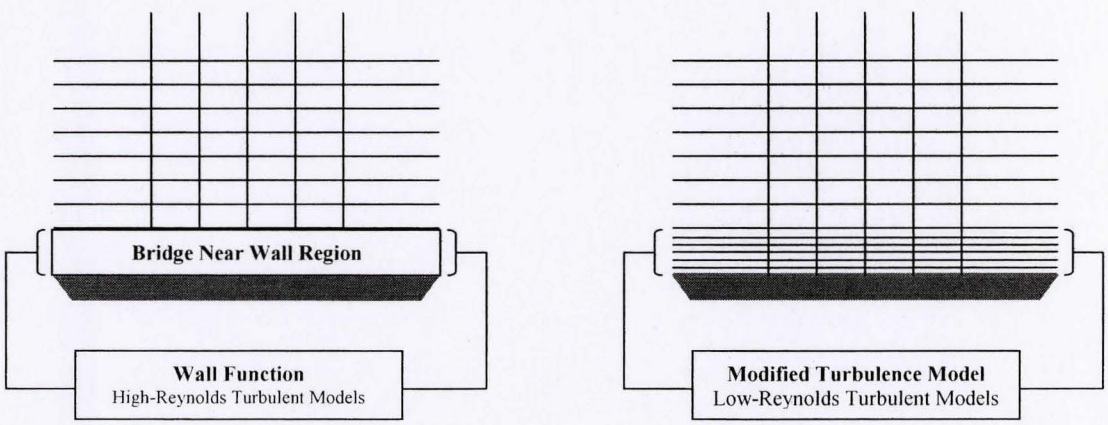

Figure 2.6 Different near-wall approaches [31]

The automatic wall function uses the same definition for energy equation treatment as the scalable wall function, and it is defined as follows for momentum equation treatment [30]:

$$u_\tau = [(u_{\tau\ Viscous})^4 + (u_{\tau\ Logarithmic})^4]^{0.25} \tag{2.19}$$

where

$$u_{\tau\ Viscous} = \frac{U}{y^+},\ u_{\tau\ Logarithmic} = \frac{U}{\frac{1}{\kappa}\log(y^+) + c} \tag{2.20}$$

Figure 2.7 shows the shift of the automatic wall function between the viscous sublayer and the logarithmic layer for velocity profile when employing different grid resolutions [30].

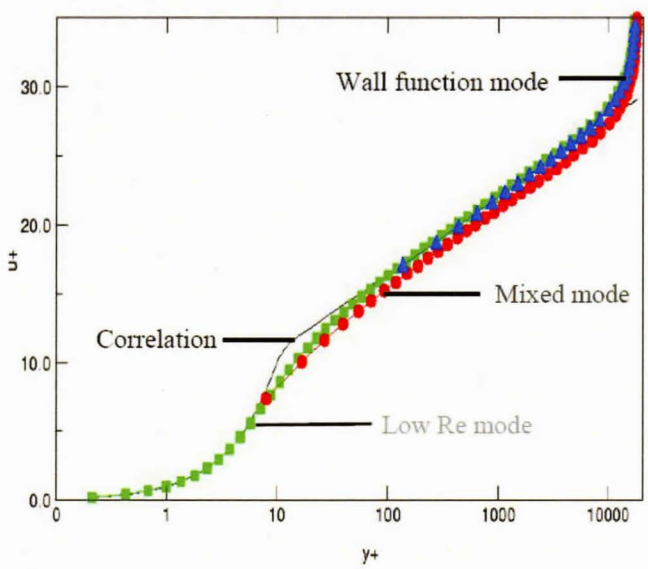

Figure 2.7 Automatic wall function treatment for velocity profile [30]

2.4 Parameters to Be Studied

The parametric study in this research involves four parameters. Three of these are the non-dimensional geometric parameters, $0.025 \le e/H \le 0.2$, $0.1 \le w/H \le 0.6$, and $0.1 \le s/H \le 0.6$. The fourth parameter, mean inlet air velocity, focuses on the hydrodynamic aspects of flow field, and it varies from 2 to 6 m/s. This is equivalent to Reynolds range of $3883 \le \mathrm{Re}_H \le 11649$, based on channel height. Each variable will be studied one at a time keeping all other variables constant. This research has taken into account all possible combinations among parameters (Re_H, e/H, w/H, and s/H) while keeping channel height, H, constant and has performed 192 study cases. Table 2.1 shows 24 of these study cases. The complete body of cases is presented in appendix A.

Table 2.1 Study Cases of Parametric Study

Study Case	e/H	w/H	s/H	$U_m\ [m/s]$	Re_H	Dissipating Power (Watts)
1	0.025	0.100	0.100	2	3883	15
2	0.025	0.100	0.100	4	7766	15
3	0.025	0.100	0.100	6	11649	15
4	0.025	0.100	0.200	2	3883	15
5	0.025	0.100	0.200	4	7766	15
6	0.025	0.100	0.200	6	11649	15
7	0.025	0.100	0.300	2	3883	15
8	0.025	0.100	0.300	4	7766	15
9	0.025	0.100	0.300	6	11649	15
10	0.025	0.100	0.600	2	3883	15
11	0.025	0.100	0.600	4	7766	15
12	0.025	0.100	0.600	6	11649	15
13	0.025	0.200	0.100	2	3883	30
14	0.025	0.200	0.100	4	7766	30
15	0.025	0.200	0.100	6	11649	30
16	0.025	0.200	0.200	2	3883	30
17	0.025	0.200	0.200	4	7766	30
18	0.025	0.200	0.200	6	11649	30
19	0.025	0.200	0.300	2	3883	30
20	0.025	0.200	0.300	4	7766	30
21	0.025	0.200	0.300	6	11649	30
22	0.025	0.200	0.600	2	3883	30
23	0.025	0.200	0.600	4	7766	30
24	0.025	0.200	0.600	6	11649	30

2.5 Grid Generation

The numerical domain (grid) is created using version 10.0 ICEM-CFD software, and is provided fully structured. Gird in computational domain are selected to be coarse in the core region of the flow and fine near the walls. In the wall region, it is ensured that y^+ is of order of unity ($y^+ \leq 1$), an

d at least 15 mesh points lie inside the boundary layer to ensure that the turbulent model works properly. Also, through the entire computational domain, the grid element aspect ratio (X/Y) lies between 0.1 and 10 so as to avoid numerical round-off errors [28]. Figures 2.8 and 2.9 show typical grids used in the parametric study and the corresponding y^+ value, respectively.

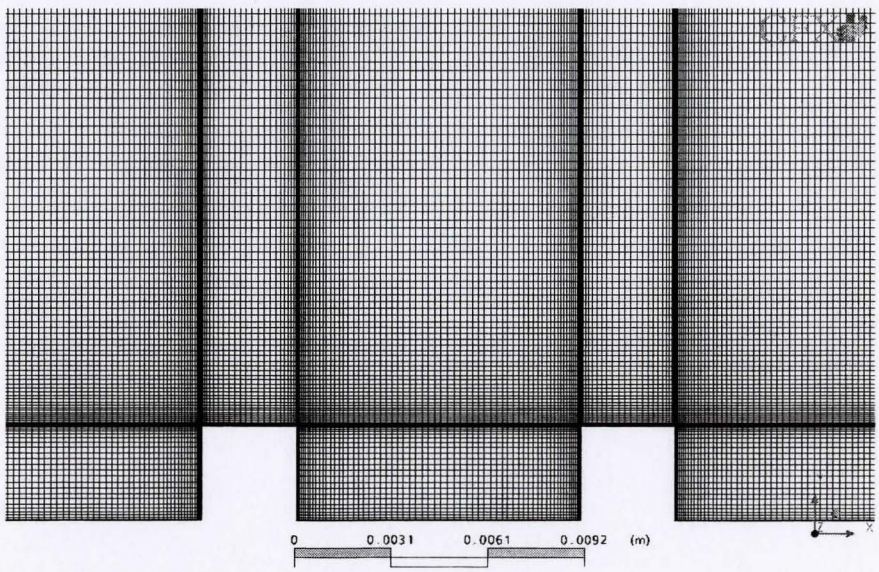

Figure 2.8 Typical grids used in the parametric study

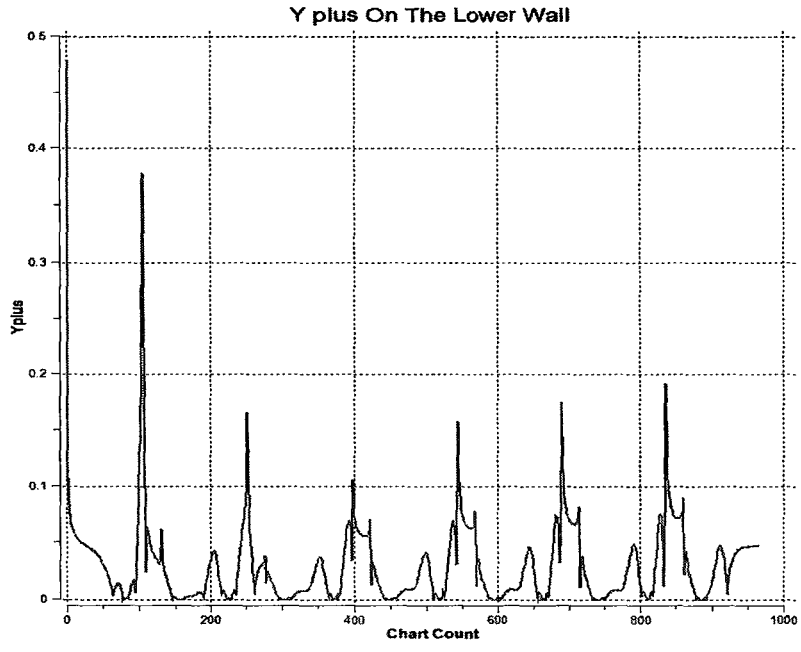

Figure 2.9 Typical y^+ values along the ribbed wall

ANSYS-CFX 10.0 is a three-dimensional solver. To provide a two-dimensional concept, the mesh is created in three-dimensions, but with only one element thickness in the Z direction, and then the symmetry condition is applied to the front and back faces of the computational domain. This condition is given by equation 2.21 [28]:

$$U_n = 0 \ , \ and \ \frac{\partial \phi}{\partial n} = 0 \tag{2.21}$$

Equation 2.21 simply states that the normal velocity component and scalar variable gradients normal to the symmetry plane are zero. In the physical sense, this condition mirrors the flow at the front and back faces of the computational domain.

Mesh independency tests in the parametric study are done by comparing the average Nusselt number on each rib with the average Nusselt number on the next successive finer mesh. When the difference between two successive average Nusselt numbers was found to be less than one percent, then the results were accepted as mesh-independent. From this practice, the total number of nodes in the parametric study falls

between 295,780 and 555,820 for different study cases, and the total number of Hexahedron elements falls between 161,142 and 276,360.

2.6 Turbulent Models

There are two main reasons behind the decomposing of scalar variables in the Navier-Stokes equation into mean and fluctuating segments and time averaging this equation. The first is that mean values are usually of interest in engineering applications and the second is that if we were to solve all turbulent scales (time and space wise), we would need an extremely fine mesh and a very fine resolution in time. Turbulence models developed to assist engineers with these problems can be categorized as follows [29]:

1. **Algebraic Models:** These models use an algebraic equation to approximate eddy viscosity. They use the Boussinesq assumption to estimate Reynolds stresses.
2. **One-Equation Models:** These models solve a transport equation for a turbulent quantity like kinetic energy and use an algebraic expression to estimate a second turbulent quantity, for example Turbulent length scale. Then turbulent viscosity is obtained from Boussinesq assumption.
3. **Two-Equation Models:** These models solve the two-transport equation for two scalar turbulent quantities, for example kinetic energy and eddy dissipation. The Reynolds stresses are then calculated by obtaining eddy viscosity from the two turbulent scalars and the Boussinesq assumption.
4. **Reynolds stress Models:** These models derive a transport equation for Reynolds stress tensor components, $\overline{u_i u_j}$. An extra transport equation is then added, for example eddy dissipation ε, to obtain length scale of turbulence.

As an example, equation 2.22 shows the exact transport equation for turbulent kinetic energy. This equation contains many unknowns such as production term, turbulent diffusion terms, and dissipation term. These unknown terms, except for the pressure term, are then modeled to obtain modeled transport equation of turbulent kinetic energy, as in equation 2.23. Equation 2.24 shows the modeled equation for a boundary layer flow ($\overline{V} << \overline{U}$ *and* $\frac{\partial}{\partial x} << \frac{\partial}{\partial y}$) [29].

$$\underbrace{\frac{\partial \rho \overline{U}_j k}{\partial x_j}}_{\text{Convection}} = \underbrace{-\frac{\partial}{\partial x_j}\left[\overline{u_j p} + \frac{1}{2}\overline{\rho u_j u_i u_i} - \mu \frac{\partial k}{\partial x_j}\right]}_{\substack{\text{Turbulent Diffusion of pressure-velocity fluctuations,} \\ \text{velocity fluctuations, and viscous diffusion}}} \underbrace{-\rho \overline{u_i u_j} \frac{\partial \overline{U}_i}{\partial x_j}}_{\text{Production}} \underbrace{-\mu \overline{\frac{\partial u_i}{\partial x_j}\frac{\partial u_i}{\partial x_j}}}_{\substack{\text{Dissipation of} \\ \text{kinetic energy} \\ \text{into internal} \\ \text{energy}}} \tag{2.22}$$

$$\underbrace{\frac{\partial \rho \overline{U}_j k}{\partial x_j}}_{\text{Convection}} = \underbrace{\frac{\partial}{\partial x_j}\left[\left(\mu + \frac{\mu_t}{\sigma_k}\right)\frac{\partial k}{\partial x_j}\right]}_{\text{Diffusion}} + \underbrace{\mu_t\left(\frac{\partial \overline{U}_i}{\partial x_j} + \frac{\partial \overline{U}_j}{\partial x_i}\right)\frac{\partial \overline{U}_i}{\partial x_j} - \frac{2}{3}\rho k \frac{\partial \overline{U}_i}{\partial x_i}}_{\text{Production}} \underbrace{-\rho \frac{k^{3/2}}{l}}_{\text{Dissipation}} \tag{2.23}$$

In which σ_k is the turbulent Prandtl number for turbulent kinetic energy.

$$\frac{\partial \rho \overline{U} k}{\partial x} + \frac{\partial \rho \overline{V} k}{\partial y} = \frac{\partial}{\partial y}\left[\left(\mu + \frac{\mu_t}{\sigma_k}\right)\frac{\partial k}{\partial y}\right] + \mu_t\left(\frac{\partial \overline{U}}{\partial y}\right)^2 - \rho \frac{k^{3/2}}{l} \tag{2.24}$$

In the current study, four turbulent models are selected, from which one will become the candidate turbulent model. This model should be qualified as being more capable of handling the physics of the flow and convective heat transfer in a two-dimensional ribbed channel. These models are chosen based on literature information, as

shown earlier, and they are used frequently in thermal management packages. These models are the standard $k-\varepsilon$ model, *RNG* $k-\varepsilon$ model, Shear Stress Transport (SST) model, and Reynolds Stress (ω based) model. The following brief describes the main characteristics of each model; Reference [28] provides a detailed description of each model.

2.6.1 Standard $k-\varepsilon$ Model

The standard $k-\varepsilon$ model is a semi-empirical model, based on transport equations for the turbulence kinetic energy, k, and dissipation rate, ε. This model assumes that flow is fully turbulent [28]; that is, the boundary layer behaves like a turbulent boundary layer. Under this condition, the inertial terms and molecular or viscous stresses (comparing to eddy viscosity) are negligible in the asymptotic limit of the inner viscous layer and the outer defect layer, which we know as the logarithmic layer [32]. Moreover, in a high Reynolds number flow, the rate at which large eddies extract energy from the mean flow is exactly the same as the rate of energy transfer to small dissipating eddies. Equation 2.25 and 2.26 define the velocity, ϑ, and length scale, l, of the large scale turbulence, respectively [33]:

$$\vartheta = k^{1/2} \tag{2.25}$$

$$l = \frac{k^{3/2}}{\varepsilon} \tag{2.26}$$

The $k-\varepsilon$ model is successful for a large variety of different flow situations, but it lacks sensitivity to adverse pressure gradients. This condition causes the model to over-predict shear stresses and, hence, separations in the flow can be delayed or completely prevented

[34]. The turbulence kinetic energy, k, and its rate of dissipation, ε, are formulated as follows [28]:

$$\frac{\partial \rho \overline{U_j} k}{\partial x_j} = \frac{\partial}{\partial x_j}\left[\left(\mu + \frac{\mu_t}{\sigma_k}\right)\frac{\partial k}{\partial x_j}\right] + P_k - \rho\varepsilon \tag{2.27}$$

$$\frac{\partial \rho \overline{U_j} \varepsilon}{\partial x_j} = \frac{\partial}{\partial x_j}\left[\left(\mu + \frac{\mu_t}{\sigma_\varepsilon}\right)\frac{\partial \varepsilon}{\partial x_j}\right] + \frac{\varepsilon}{k}(C_{\varepsilon 1} P_k - C_{\varepsilon 2}\rho\varepsilon) \tag{2.28}$$

$$\mu_t = C_\mu \rho \frac{k^2}{\varepsilon} \tag{2.29}$$

in which $C_\mu = 0.09$, $\sigma_k = 1.0$, $\sigma_\varepsilon = 1.3$, $C_{\varepsilon 1} = 1.44$, and $C_{\varepsilon 2} = 1.92$ are $k-\varepsilon$ turbulent model constant, and P_k is the shear production term of turbulence defined as [28]:

$$P_k = \underbrace{\mu_t\left(\frac{\partial \overline{U_i}}{\partial x_j} + \frac{\partial \overline{U_j}}{\partial x_i}\right)\frac{\partial \overline{U_i}}{\partial x_j}}_{\text{Turbulent Shear stresses Production}} \underbrace{-\frac{2}{3}\rho k \frac{\partial \overline{U_i}}{\partial x_i}}_{\text{Turbulent Normal stresses Production}} \tag{2.30}$$

It should be noted that in the transport equation of dissipation rate, ε, the regions of flow where low turbulence exists, both k and ε approach zero, and this appears to be a problem because the destruction term in equation 2.28 includes $\frac{\varepsilon^2}{k}$ [29]. A remedy to this problem is that both k and ε quantities go to zero at the wall with a correct rate. This can be achieved by introducing a dampening function in the eddy viscosity term, f_μ. The

$k-\varepsilon$ model that uses a dampening function are referred to as low Reynolds $k-\varepsilon$ models. The dampening function term is of the order of $O(y^{-1})$ close to the wall, and approaches unity away ($y^+ \geq 30$) from the wall.

Moreover, in both transport equations 2.27 and 2.28, k and ε quantities are isotropic (independent of direction). This fact is obvious from equation 2.30, where turbulent normal stress terms[2] ($-\rho\overline{u^2}$, $-\rho\overline{v^2}$, $-\rho\overline{w^2}$) are each given an equal $\frac{1}{3}$ weight to account for kinetic energy. The boundary conditions for the standard $k-\varepsilon$ turbulent model are as follows [33]:

Entrance: Distribution of k and ε are given in section 2.2.1

Exit: $\frac{\partial k}{\partial n}=0$ and $\frac{\partial \varepsilon}{\partial n}=0$ (2.31)

Solid Walls: Scalable Wall function, $k=\frac{u_\tau^{\,2}}{\sqrt{C_\mu}}$, $\varepsilon=\frac{u_\tau^{\,3}}{\kappa\, y_w}$, and

$$\mu_t=\rho C_\mu \frac{k^2}{\varepsilon}=\rho\kappa u_\tau y_w$$

2.6.2 RNG $k-\varepsilon$ Model

The RNG-based $k-\varepsilon$ turbulence model is derived from the instantaneous Navier-Stokes equations using a mathematical technique called renormalization group (RNG) method. This method results in a model with different constants from those in the standard $k-\varepsilon$ model. But the transport equation for turbulent generation and dissipation

[2] Although this term is zero, due to the continuity equation (fluid is assumed incompressible) it has been included for clarification.

remains the same. A more comprehensive description of RNG theory and its application to turbulence can be found in [28].

$$\frac{\partial \rho \overline{U}_j k}{\partial x_j} = \frac{\partial}{\partial x_j}\left[\left(\mu + \frac{\mu_t}{\sigma_{k\ RNG}}\right)\frac{\partial k}{\partial x_j}\right] + P_k - \rho\varepsilon \tag{2.32}$$

$$\frac{\partial \rho \overline{U}_j \varepsilon}{\partial x_j} = \frac{\partial}{\partial x_j}\left[\left(\mu + \frac{\mu_t}{\sigma_{\varepsilon\ RNG}}\right)\frac{\partial \varepsilon}{\partial x_j}\right] + \frac{\varepsilon}{k}(C_{\varepsilon 1\ RNG} P_k - C_{\varepsilon 2\ RNG}\rho\varepsilon) \tag{2.33}$$

$$P_k = \mu_t\left(\frac{\partial \overline{U}_i}{\partial x_j} + \frac{\partial \overline{U}_j}{\partial x_i}\right)\frac{\partial \overline{U}_i}{\partial x_j} - \frac{2}{3}\rho\, k\frac{\partial \overline{U}_i}{\partial x_i} \tag{2.34}$$

$$\mu_t = \rho\, C_{\mu\ RNG}\ \frac{k^2}{\varepsilon} \tag{2.35}$$

where

$$C_{\mu\ RNG} = 0.085,\ \sigma_{k\ RNG} = 0.7179,\ \sigma_{\varepsilon\ RNG} = 0.7179,\ C_{\varepsilon 1\ RNG} = 1.42 - f_\eta\ ,\ and\ C_{\varepsilon 2\ RNG} = 1.68$$

and where f_η is defined as:

$$f_\eta = \frac{\eta\left(1 - \frac{\eta}{4.38}\right)}{(1 + \beta_{RNG}\,\eta^3)}\ ,\ \eta = \sqrt{\frac{P_k}{\rho\, C_{\mu\ RNG}\ \varepsilon}} \tag{2.36}$$

2.6.3 $k-\omega$ Model

The Wilcox $k-\omega$ model solves two transport equations. The turbulent kinetic energy, k, and the specific dissipation rate, ω, (turbulent frequency) are formulated as follows [30]:

$$\frac{\partial \rho \overline{U_j} k}{\partial x_j} = \frac{\partial}{\partial x_j}\left[\left(\mu + \frac{\mu_t}{\sigma_k}\right)\frac{\partial k}{\partial x_j}\right] + P_k - \beta' \rho\, k\omega \tag{2.37}$$

$$\frac{\partial \rho \overline{U_j} \omega}{\partial x_j} = \frac{\partial}{\partial x_j}\left[\left(\mu + \frac{\mu_t}{\sigma_\omega}\right)\frac{\partial \omega}{\partial x_j}\right] + \alpha \frac{\omega}{k} P_k - \beta \rho\, \omega^2 \tag{2.38}$$

$$P_k = \mu_t \left(\frac{\partial \overline{U_i}}{\partial x_j} + \frac{\partial \overline{U_j}}{\partial x_i}\right)\frac{\partial \overline{U_i}}{\partial x_j} - \frac{2}{3}\rho\, k \frac{\partial \overline{U_i}}{\partial x_i} \tag{2.39}$$

$$\mu_t = \rho \frac{k}{\omega} \tag{2.40}$$

in which $\beta' = 0.09$, $\alpha = 5/9$, $\beta = 0.075$, $\sigma_k = 2$, and $\sigma_\omega = 2$ are dimensionless constants. Comparing with ε equation of 2.28, the turbulent production term in turbulent frequency ω of equation 2.38 does not include k, and the turbulent diffusion term in this equation simply goes to zero as k approaches zero. Overall, the $k-\omega$ turbulent model performs significantly better under an adverse pressure gradient than the $k-\varepsilon$ model, the low Reynolds version with damping function. And since the $k-\omega$ turbulent model does not employ a damping function in the near wall region, it has a significant advantage in numerical stability [34]. Another important advantage of the $k-\omega$ turbulent model is

that it needs a resolution of $y^+ < 2$ near the walls, while a $k-\varepsilon$ turbulent model (low Reynolds version) typically requires a near wall resolution of $y^+ < 0.2$ [28]. On the other hand, this model has shown to have a strong dependency of results on the free stream values of ω_f [35]. This means that, depending on the values specified for ω at the inlet, results could differ substantially [28]. The boundary conditions for the standard $k-\omega$ turbulent model are given as follows [32] and [34]:

Entrance: Distribution of k are given in section 2.2.1 and $\omega_f = \frac{4}{\sqrt{\beta'}} \frac{u_\tau^2}{U_e \delta^*}$

Exit: $\frac{\partial k}{\partial n} = 0$ and $\frac{\partial \omega}{\partial n} = 0$ (2.41)

Solid Walls: Wall function is given in section 2.2.3, $k = \frac{u_\tau^2}{\sqrt{\beta'}}$, and $\omega = \frac{u_\tau}{\sqrt{\beta'} \kappa \, y_w}$

At solid walls, the above boundary condition tends to infinity for ω close to the wall, as $k \to 0$. Close to the wall, to derive a boundary condition for ω, the largest terms in a specific dissipation rate equation are viscous diffusion and destruction. Equation 2.38 close to the wall simplifies to [29]:

$$0 = \frac{\partial}{\partial x_j}\left[\mu \frac{\partial \omega}{\partial x_j}\right] - \beta \rho \, \omega^2 \tag{2.42}$$

which gives; $\omega = \frac{6\nu}{\beta \, y^2}$ (2.43)

Close to the wall, ω is usually not solved, and for $y^+ < 2.5$ it is calculated from equation 2.43. The $k-\omega$ turbulent model in this case is referred to as the low Reynolds number $k-\omega$ model [29].

2.6.4 Shear Stress Transport (SST) Model

The Shear Stress Transport (SST) model combines the $k-\omega$ turbulent model to work at the wall and the $k-\varepsilon$ turbulent model to work in the bulk flow. To ensure a smooth transition between the two models, SST employs a blending function (F_1) based on the distance to the nearest surface and on flow variables [28]. F_1 has a value of 1 close to the surface, and zero in the outer part and free shear flows. A value of 1 activates the $k-\omega$ model, and a value of zero activates the $k-\varepsilon$ model. This approach utilizes the well near wall performance of the $k-\omega$ model without the potential of introduced error due to the free stream sensitivity of the model [30]. Figure 2.10 shows how this blending function works in the computational domain.

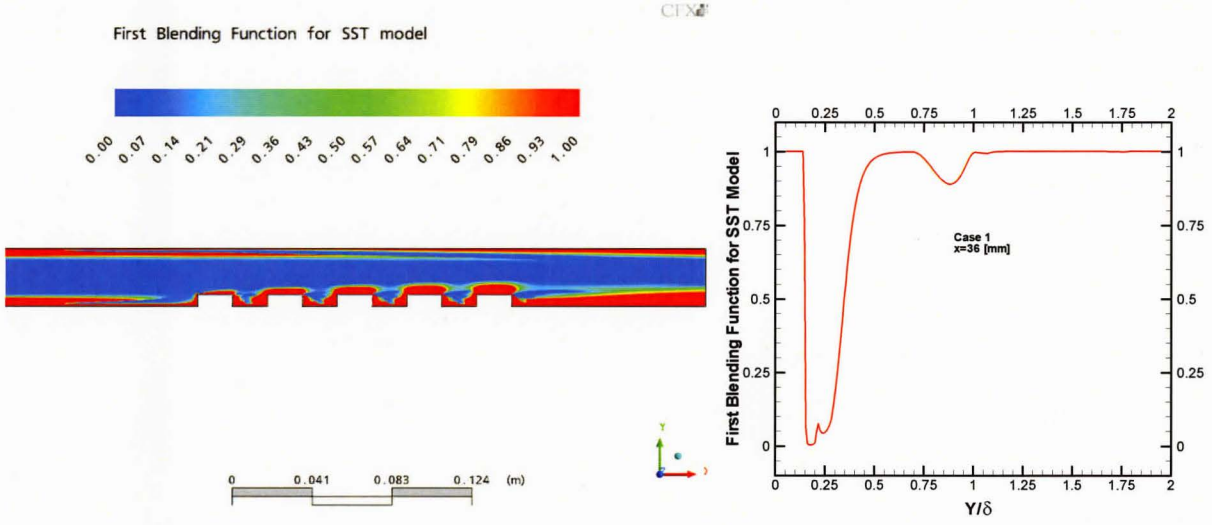

(a) (b)

Figure 2.10 Blending function between $k-\omega$ and $k-\varepsilon$ models

(a) A typical case in parametric study (b) Direct Numerical Simulation with periodic stream wise boundary condition (section 3.2)

In addition to the first blending function, the SST model uses a second blending function (F_2) that makes it different from an eddy viscosity model. This difference comes from the way in which the SST model handles eddy viscosity in the near wall region and outer boundary layer region. In the near wall region, eddy viscosity is modeled on Bradshaw's assumption that the shear stress in a boundary layer is proportional to the turbulent kinetic energy. In the outer free shear layer, the eddy viscosity is computed as its original formulation based on the Boussinesq assumption [34]. Figure 2.11 shows how this blending function applies in the computational domain.

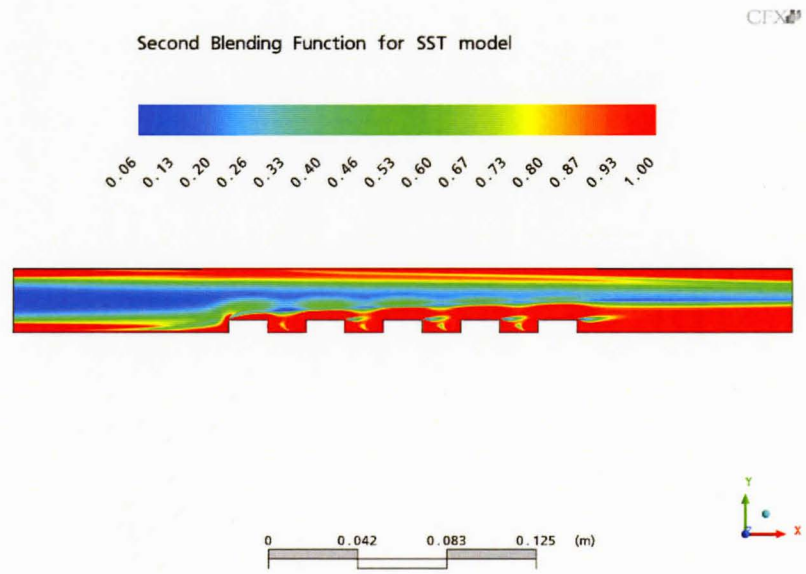

Figure 2.11 Blending function for different eddy viscosity formulations

Perhaps the SST model is named because of the definition of the modified turbulent viscosity to account for the transport of the principal turbulent shear stress[3], which gives the SST model an advantage in terms of performance over both the standard $k-\omega$ model and the standard $k-\varepsilon$ model. The two eddy viscosity definitions are as follows [30]:

[3] Although this is still isotropic and, hence, works better for higher Reynolds number flows

$$\tau_{ij} = -\rho\overline{u_i u_j} = 0.31\rho\, k \quad \text{and} \quad \mu_t = \rho\frac{0.31k}{\max(a_1\omega\ ;\ \sqrt{2}SF_2)} \tag{2.44}$$

$$\tau_{ij} = -\rho\overline{u_i u_j} = \mu_t\left(\frac{\partial\overline{U_i}}{\partial x_j} + \frac{\partial\overline{U_j}}{\partial x_i} - \frac{2}{3}\frac{\partial\overline{U_k}}{\partial x_k}\right) - \frac{2}{3}\rho k\delta_{ij} \quad \text{and} \quad \mu_t = \rho\frac{k}{\omega} \tag{2.45}$$

Equation 2.44 introduces a feature of the SST model that is an upper band limit in the shear stress boundary layer, in order to avoid excessive shear stress levels[4]. In this equation, S is the absolute value of the strain rate and F_2 is defined according to equation 2.46 [30]:

$$F_2 = \tanh(\arg_2^2), \qquad \arg_2 = \max\left(\frac{2\sqrt{k}}{\beta'\omega\, y}\ ;\ \frac{500\nu}{y^2\omega}\right) \tag{2.46}$$

The formulation of the Shear Stress Turbulent model is as follows [30]:

$$\frac{\partial\rho\overline{U_j}k}{\partial x_j} = \frac{\partial}{\partial x_j}\left[\left(\mu + \frac{\mu_t}{\sigma_{k3}}\right)\frac{\partial k}{\partial x_j}\right] + \tilde{P}_k - \beta'\rho\, k\omega \tag{2.47}$$

$$\frac{\partial\rho\overline{U_j}\omega}{\partial x_j} = \frac{\partial}{\partial x_j}\left[\left(\mu + \frac{\mu_t}{\sigma_{\omega 3}}\right)\frac{\partial\omega}{\partial x_j}\right] + \alpha_3\frac{\omega}{k}P_k - \beta_3\rho\,\omega^2 + (1-F)2\rho\frac{1}{\sigma_{\omega 2}\omega}\frac{\partial k}{\partial x_j}\frac{\partial\omega}{\partial x_j} \tag{2.48}$$

$$\tilde{P}_k = \min\left[P_k\ ;\ c_{\lim}\varepsilon\right] \quad \text{and} \quad P_k = \tau_{ij}\frac{\partial\overline{U_i}}{\partial x_j} \tag{2.49}$$

[4] This usually happens with Boussinesq eddy viscosity models [30]

in which $c_{lim} = 10$ is a limiter that does not affect the shear layer performance but prevents build-up of turbulence in stagnation regions. The coefficients with subscript 3 are a linear combination of the $k-\omega$ model with subscript 1, and the transformed $k-\varepsilon$ model with subscript 2. This function is defined as follows [28]:

$$\varphi_3 = F_1\varphi_1 + (1-F_1)\varphi_2 \tag{2.50}$$

where φ_1, φ_2, and φ_3 represent the coefficients used in $k-\omega$, $k-\varepsilon$, and SST models, respectively. Other dimensionless constants are $\beta' = 0.09$, $\alpha_1 = 5/9$, $\beta_1 = 0.075$, $\sigma_{k1} = 2$, $\sigma_{\omega 1} = 2$, $\alpha_2 = 0.44$, $\beta_2 = 0.0828$, $\sigma_{k2} = 1$, and $\sigma_{\omega 2} = 1/0.856$. The blending function F_1 is defined as [28]:

$$F_1 = \tanh(\arg_1^4) \tag{2.51}$$

in which

$$\arg_1 = \min\left(\max(\arg_2), \left(\frac{4\rho\, k}{CD_{k\omega}\sigma_{\omega 2}\, y^2}\right)\right) \text{ and } CD_{k\omega} = \max\left(2\rho\frac{1}{\sigma_{\omega 2}\omega}\frac{\partial k}{\partial x_j}\frac{\partial \omega}{\partial x_j};\ 1.0\times 10^{-10}\right)$$

The SST turbulent model uses the following boundary conditions [34]:

Entrance: Distributions of k are given in section 2.2.1 and $\omega_f = \frac{4}{\sqrt{\beta'}}\frac{u_\tau^{\,2}}{U_e\delta^*}$

Exit: $\frac{\partial k}{\partial n} = 0$ and $\frac{\partial \omega}{\partial n} = 0$ (2.52)

Solid Walls: Automatic Wall function, $k = 0$, and $\omega = 10\frac{6\nu}{\beta_1(\Delta y)^2}$

2.6.5 Reynolds Stress Model (RSM/SMC)

The most elaborate and complex classical turbulence model (in this study) is the Reynolds stress equation model (RSM), also called second moment closure (SMC) [33]. This model benefits from directional effects of Reynolds stresses by solving the transport equation for each individual term of Reynolds stress tensor (six terms)[5] and another equation for the dissipation rate. Because of their high computational cost, therefore, Reynolds stress models are not as popular as the one- and two-equation models. There are many versions of the Reynolds Stress model, and the one used in the current study is the Wilcox Stress-Omega model. This model, with automatic wall function, allows a more accurate treatment near the wall based on the grid resolution used. The following equations describe the ω-based Reynolds stress model [28]:

$$\frac{\partial}{\partial x_k}\left(\rho\overline{u_i u_j}\frac{\partial \bar{U}}{\partial x_k}\right) = -\rho\, P_{ij} + \frac{2}{3}\beta'\rho\,\omega\, k\delta_{ij} - \rho\,\Pi_{ij} + \frac{\partial}{\partial x_k}\left[\left(\mu + \frac{\mu_t}{\sigma^*}\right)\frac{\partial \overline{u_i u_j}}{\partial x_k}\right] \tag{2.53}$$

$$\frac{\partial \rho \bar{U}_k \omega}{\partial x_k} = \frac{\partial}{\partial x_k}\left[\left(\mu + \frac{\mu_t}{\sigma}\right)\frac{\partial \omega}{\partial x_k}\right] + \alpha\frac{\omega}{k}P_k - \beta\rho\,\omega^2 \tag{2.54}$$

$$\mu_t = \rho\frac{k}{\omega} \tag{2.55}$$

where

[5] This is because Reynolds stress tensor is symmetric

$$\underbrace{P_{ij} = \overline{u_i u_k}\frac{\partial \overline{U_j}}{\partial x_k} + \overline{u_j u_k}\frac{\partial \overline{U_i}}{\partial x_k}}_{\text{Production Tensor of Reynolds Stresses}}, \quad P = \frac{1}{2}P_{kk} \tag{2.56}$$

$$\underbrace{\Pi_{ij} = \beta' C_1 \omega\left(\overline{u_i u_j} + \frac{2}{3}k\delta_{ij}\right) - \hat{\alpha}\left(P_{ij} - \frac{2}{3}P\delta_{ij}\right) - \hat{\beta}\left(D_{ij} - \frac{2}{3}P\delta_{ij}\right) - \hat{\gamma}\, k\left(S_{ij} - \frac{1}{3}S_{kk}\delta_{ij}\right)}_{\text{Modeled Pressure-Strain Correlation}} \tag{2.57}$$

$$D_{ij} = \overline{u_i u_k}\frac{\partial \overline{U_k}}{\partial x_j} + \overline{u_j u_k}\frac{\partial \overline{U_k}}{\partial x_i} \tag{2.58}$$

In the above equations $\sigma^* = 2$, $\sigma = 2$, $\beta = 0.075$, $\alpha = 5/9$, $\beta' = 0.09$, $\hat{\alpha} = (8 + C_2)/11$, $\hat{\beta} = (8C_2 - 2)/11$, $\hat{\gamma} = (60C_2 - 4)/55$, $C_1 = 1.8$, *and* $C_2 = 0.52$ are constants.

Chapter Three

Choosing a Turbulence Model

3.1 Introduction

This study has used direct numerical simulation (DNS) to compare between the previous turbulent models and two sets of experimental data to examine the accuracy of candidate turbulent model. The direct numerical simulation [36] was used to investigate the capabilities of each turbulent model in capturing the structure of heat and flow field in the ribbed channel with heated blocks. Of the two experiments, both were used to examine the precision of the turbulent models. One [37] was used to assess the sensitivity of each turbulent model to predict an appropriate heat transfer profile. The second experiment [38] helped in determining how the SST turbulent model performs and predicts under a high element-to-channel height aspect ratio (effect of stream curvature, 3D) as a sensitive case.

3.2 Applicability of Turbulent Models for the Present Study

In this section, the standard $k-\varepsilon$, $k-\omega$, SST, and RSM are analytically compared in terms of accuracy. In addition, important points of flow within a ribbed channel structure are briefly examined, including first rib windward face stagnation point, and recirculation region. To compare turbulent models, the production terms of Reynolds stresses are selected and compared. Equations 3.1, 3.2, and 3.3 restate this term for each model:

$k-\varepsilon$ And $k-\omega$ Model

$$P_k = \mu_t \left(\frac{\partial \overline{U_i}}{\partial x_j} + \frac{\partial \overline{U_j}}{\partial x_i} \right) \frac{\partial \overline{U_i}}{\partial x_j} - \frac{2}{3} \rho \, k \frac{\partial \overline{U_i}}{\partial x_i} \qquad (3.1)$$

SST Model:
$$P_k = \tau_{ij}\frac{\partial \overline{U_i}}{\partial x_j},\ \tau_{ij} = -\rho\overline{u_i u_j} = 0.31\rho\ k,\ k = \frac{1}{2}\overline{u_i u_i} \qquad (3.2)$$

RSM Model:
$$P_{ij} = -\rho\left(\overline{u_i u_k}\frac{\partial \overline{U_j}}{\partial x_k} + \overline{u_j u_k}\frac{\partial \overline{U_i}}{\partial x_k}\right) \qquad (3.3)$$

3.2.1 Stagnation Point

The stagnation point on the first rib windward face is shown in figure 3.1 (approximate location) [39]. At this location, $\overline{u^2} \approx \overline{v^2}$, and the production due to normal stresses is zero [29]. The production term due to $-\rho\overline{u}^2$ and $-\rho\overline{v}^2$ stresses for each turbulent model according to equations 3.1, 3.2, and 3.3 are:

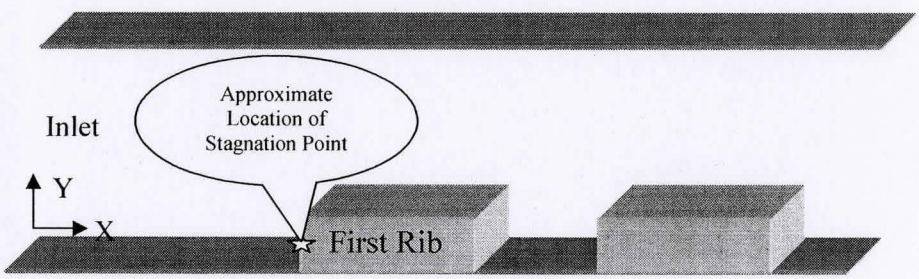

Figure 3.1 Approximate location of stagnation
Point on the windward face of first rib

$k-\varepsilon$ And $k-\omega$ Model $$P_k = 2\mu_t \left[\left(\frac{\partial \overline{U}}{\partial x} \right)^2 + \left(\frac{\partial \overline{V}}{\partial y} \right)^2 \right] \quad (3.4)$$

SST Model: $$P_k = 0.62\rho\, k \left(\frac{\partial \overline{U}}{\partial x} + \frac{\partial \overline{V}}{\partial y} \right) \quad (3.5)$$

RSM Model: $$P_{ij} = -2\rho\, \overline{uv} \left(\frac{\partial \overline{U}}{\partial y} + \frac{\partial \overline{V}}{\partial x} \right) \quad (3.6)$$

Due to continuity ($\frac{\partial \overline{U}}{\partial x} = -\frac{\partial \overline{V}}{\partial y}$), and $\overline{u^2} \approx \overline{v^2}$, the above simplifies to:

$k-\varepsilon$ And $k-\omega$ Model $$P_k = 2\mu_t \left[\left(\frac{\partial \overline{U}}{\partial y} \right)^2 + \left(\frac{\partial \overline{V}}{\partial x} \right)^2 \right] \quad (3.7)$$

SST Model: $$P_k = 0 \quad (3.8)$$

RSM Model [29]: $$P_{ij} \approx 0 \quad (3.9)$$

These values show that the $k-\varepsilon$ And $k-\omega$ models over-predict the production term at this point, but that SST and RSM are capable of handling the production term appropriately.

3.2.2 Recirculation Region

In the recirculation region, figure 3.2, concave and convex streamlines are present where the entire Reynolds stress tensor, shear and normal, is important [29]. The production term before distortion, as long as it is parallel to the wall, is a result of the $\frac{\partial \overline{U}}{\partial y}$ term, and in a distorted area both $\frac{\partial \overline{U}}{\partial y}$ and $\frac{\partial \overline{V}}{\partial x}$ contribute to the production term. According to equations 3.1, 3.2, and 3.3, the production terms for $-\rho\overline{u}^2$, $-\rho\overline{v}^2$, and $-\rho\,\overline{uv}$ stresses give:

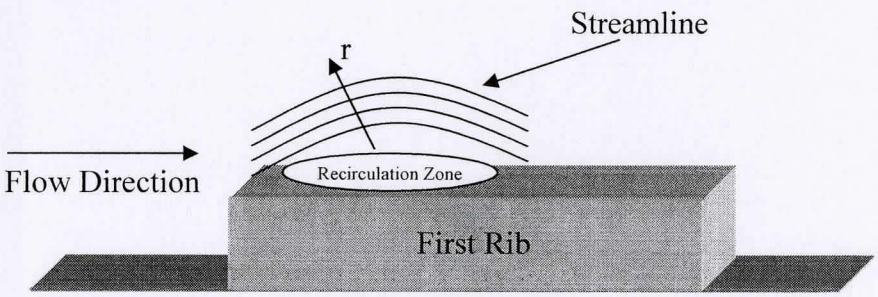

Figure 3.2 Concave and convex streamlines

$k-\varepsilon$ and $k-\omega$ model:

$-\rho\overline{u^2}$:
$$P_k = 2\mu_t\left(\frac{\partial \overline{U}}{\partial x}\right)^2 \tag{3.10}$$

$-\rho\overline{v^2}$:
$$P_k = 2\mu_t\left(\frac{\partial \overline{V}}{\partial y}\right)^2 \tag{3.11}$$

$-\rho\overline{uv}$:
$$P_k = \mu_t\left[\left(\frac{\partial \overline{U}}{\partial y}+\frac{\partial \overline{V}}{\partial x}\right)\frac{\partial \overline{U}}{\partial y}+\left(\frac{\partial \overline{U}}{\partial y}+\frac{\partial \overline{V}}{\partial x}\right)\frac{\partial \overline{V}}{\partial x}\right] \tag{3.12}$$

SST Model:

$$-\rho\overline{u^2}: \qquad P_k = 0.31\rho\, k\left(\frac{\partial \overline{U}}{\partial x}+\frac{\partial \overline{V}}{\partial y}\right) \tag{3.13}$$

$$-\rho\overline{v^2}: \qquad P_k = 0.31\rho\, k\left(\frac{\partial \overline{V}}{\partial y}+\frac{\partial \overline{U}}{\partial x}\right) \tag{3.14}$$

$$-\rho\overline{uv}: \qquad P_k = 0.31\rho\, k\frac{\partial \overline{U}}{\partial y} \tag{3.15}$$

RSM Model:

$$-\rho\overline{u^2}: \qquad P_{ij} = -2\rho\ \overline{uv}\frac{\partial \overline{U}}{\partial y} \tag{3.16}$$

$$-\rho\overline{v^2}: \qquad P_{ij} = -2\rho\ \overline{vu}\frac{\partial \overline{V}}{\partial x} \tag{3.17}$$

$$-\rho\overline{uv}: \qquad P_{ij} = -\rho\left(\overline{u^2}\frac{\partial \overline{V}}{\partial x}+\overline{v^2}\frac{\partial \overline{U}}{\partial y}\right) \tag{3.18}$$

Let us assume $\frac{\partial \overline{U}_\theta}{\partial r} > 0$, *and* $U_r = 0$ in the convex portion of the streamline. This assumption dictates that fluctuations in the radial direction according to equation 3.19 (instantaneous inviscid momentum) will be dampened (stabilizing effect) [29].

$$\frac{\rho U^2{}_\theta}{r} = \frac{\partial P}{\partial r} \tag{3.19}$$

In the RSM model, a decrease in magnitude of the $-\rho\overline{u}^2$ or $-\rho\overline{v}^2$ term will give a negative feedback to $-\rho\overline{uv}$ and decrease its value. This process continues, and hence, this model can handle stabilizing and destabilizing effects. In the SST model, a decrease in the magnitude of $-\rho\overline{u^2}$ or $-\rho\overline{v^2}$ also gives a negative feedback to $-\rho\overline{uv}$ ($k=\frac{1}{2}\left(\overline{u^2}+\overline{v^2}\right)$) and decreases its value. Although the SST model is shown to be capable of managing stabilizing and destabilizing effects, unlike RSM, it is not sensitive to $\frac{\partial\overline{V}}{\partial x}$ gradients in the flow (height aspect ratio) similar to the situation discussed in [18]. Among turbulence models, $k-\varepsilon$ and $k-\omega$ models show no sensitivity for stabilizing and destabilizing effects, a drawback that makes them inappropriate models for solving flows with concave or convex (not parallel) streamlines.

3.3 Comparison with Direct Numerical Simulation (DNS)

3.3.1 Problem Definition

The two dimensional flow and heat transfer between two infinite parallel plates has been solved numerically using ANSYS CFX 10.0. The geometry of the domain used is shown in figure 3.3, where the origin of the coordinate system is located at middle of the lower plate. The upper plate is smooth, while on the lower plate six ribs of height e and length w are spaced a distance s from each other. The two plates are separated by a distance H (channel height) and are kept at constant temperature. The upper cold plate is maintained at uniform temperature of 0^oC (T_c= 0^oC), while the lower hot plate is maintained at a higher temperature of 50^oC (T_h= 50^oC). Different rib heights, e, have been used in the current study as shown in table 3.1. The rib length, spacing between ribs,

entrance length ($L_{Enterance}$), and exit length (L_{Exit}) were fixed at 3, 9, 4.5 and 4.5 mm, respectively.

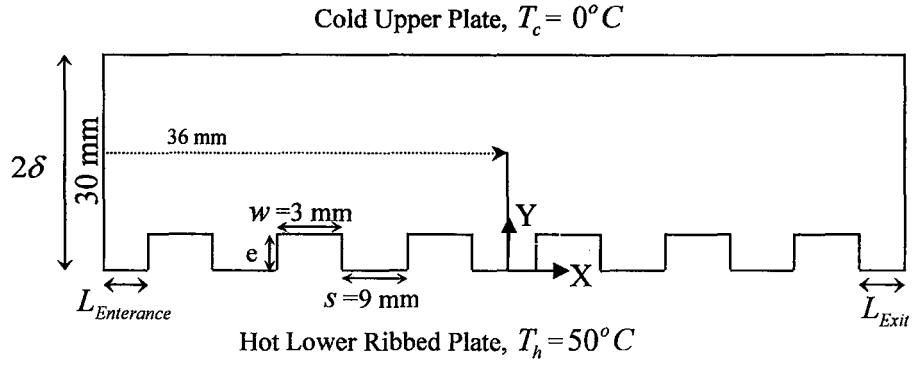

Figure 3.3 The geometry of the problem

Table 3.1 Different Cases of the

Study Case Number	Case 1	Case 2	Case 3	Case 4
Element Height e [mm]	3	1.5	0.75	0

Flow at inlet and exit of the computational domain is assumed fully developed turbulent flow. This condition is maintained by applying periodic boundary conditions at both the inlet and the exit. The flow is induced through the channel by applying mean pressure gradient of 1.886110 [Pa/m] from the inlet to the exit of the domain. This pressure gradient was applied as a source term in the stream-wise direction momentum equation.

For all meshes used in this study, the y^+ values were taken as order of unity. Mesh independent solutions were obtained for all turbulent models using structured mesh, with high densities in the vicinity of walls in order to capture the higher gradients of both

hydrodynamic and thermal boundary layers in this region. The total number of hexahedron elements in the computational domain was about 115,000.

3.3.2 Results and Discussions

Mean velocity streamlines, obtained using the four turbulence models, are shown in Figures 3.4, 3.5, and 3.6 for rib-height to channel-height ratios (e/H) of 0.1, 0.05, and 0.025 m, respectively, and for a Reynolds number based on friction velocity and channel half width (Re_τ) of approximately 150. The rib width and spacing between ribs are kept constant at $w/H = 0.1$ and $s/H = 0.3$, respectively. Corresponding DNS results, shown along with each case, reveal that for the highest rib, case 1, two vortices are occupying the enclosure between the ribs. The centre of the larger vortex is shifted towards the downward face of the rib, while the smaller is confined to the corner between the leeward face of the rib and the bottom wall. This feature is well captured by both the SST and *ω-RSM* turbulence model, while for the *k-ε* and *RNG k-ε* models the larger vortex is shifted toward the opposite (upward) face of the rib, as shown in Figure 3.4. For the second case, $e/H = 0.05$, shown in figure 3.5, the smaller vortex no longer exists and the larger one is stretched within the enclosure between ribs with its centre moving toward the upward face of the rib. The SST model is still capable of capturing this feature along with the *ω-RSM* model. The same take place in case 3, $e/H = 0.025$, as shown in Figure 3.6, where unlike the SST and *ω-RSM* models, the *k-ε* and *RNG k-ε* models fails to cope up with the change in the structure of the vortices formed in the enclosure between ribs.

The contours of the mean temperature obtained from the present work DNS study for the same three cases mentioned above are shown in figure 3.7, 3.8, and 3.9 compared with the DNS solution from [36]. The temperature contours are closely packed at the front corners of the ribs, indicating higher heat transfer rates at these locations. This observation is not only shown by the DNS results [36] but also confirmed in the experimental work by Liou et al. [40]. This phenomenon is captured by both the SST and the *ω-RSM* model, while the *k-ε* and *RNG k-ε* models could not capture this phenomenon.

However, the temperature contours of $e/H = 0.05$, case 2, (figure 3.8) computed using the SST and *ω-RSM* models, show a more stratified manner than those captured by DNS, where a wavy pattern upstream of the rib is apparent.

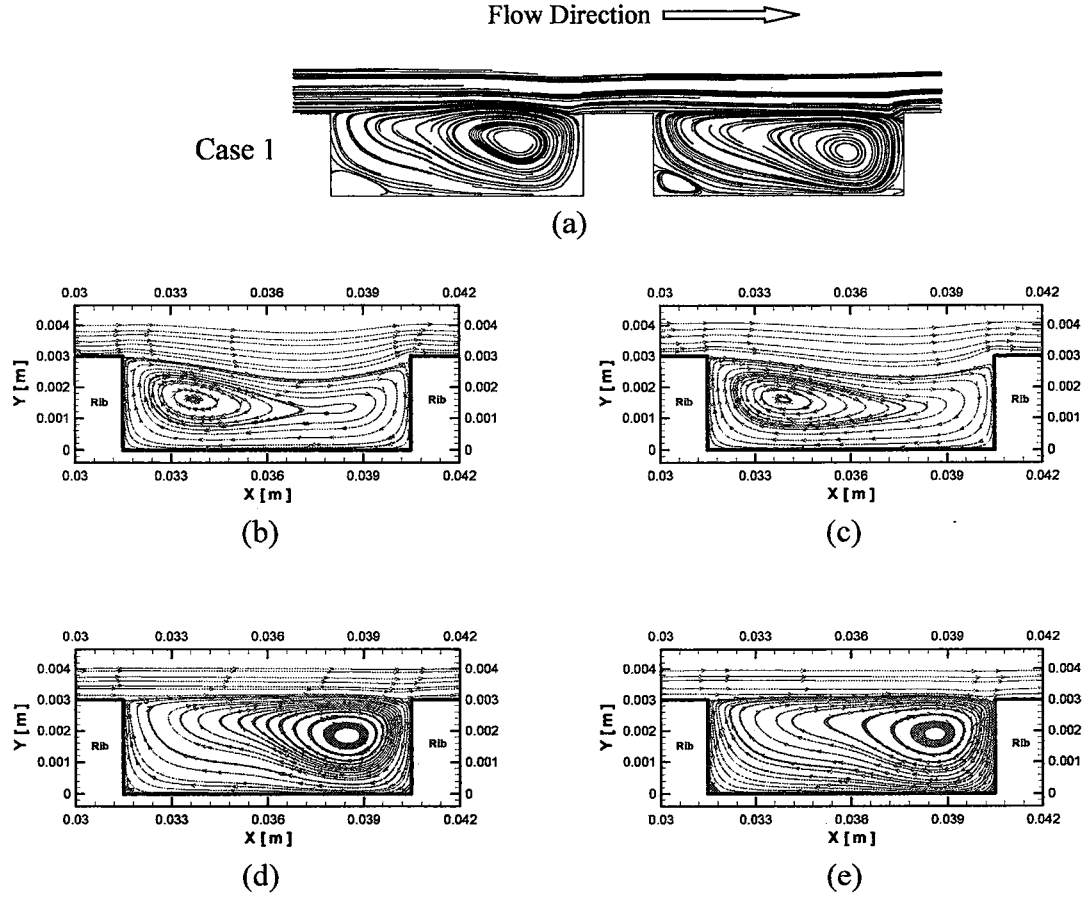

Figure 3.4: Streamlines of mean velocity (e/H = 0.1, w/H = 0.1 and s/H = 0.3) (a) DNS [36] (b) $k-\varepsilon$ (c) RNG $k-\varepsilon$ (d) *SST* (e) *ω-RSM* turbulent models.

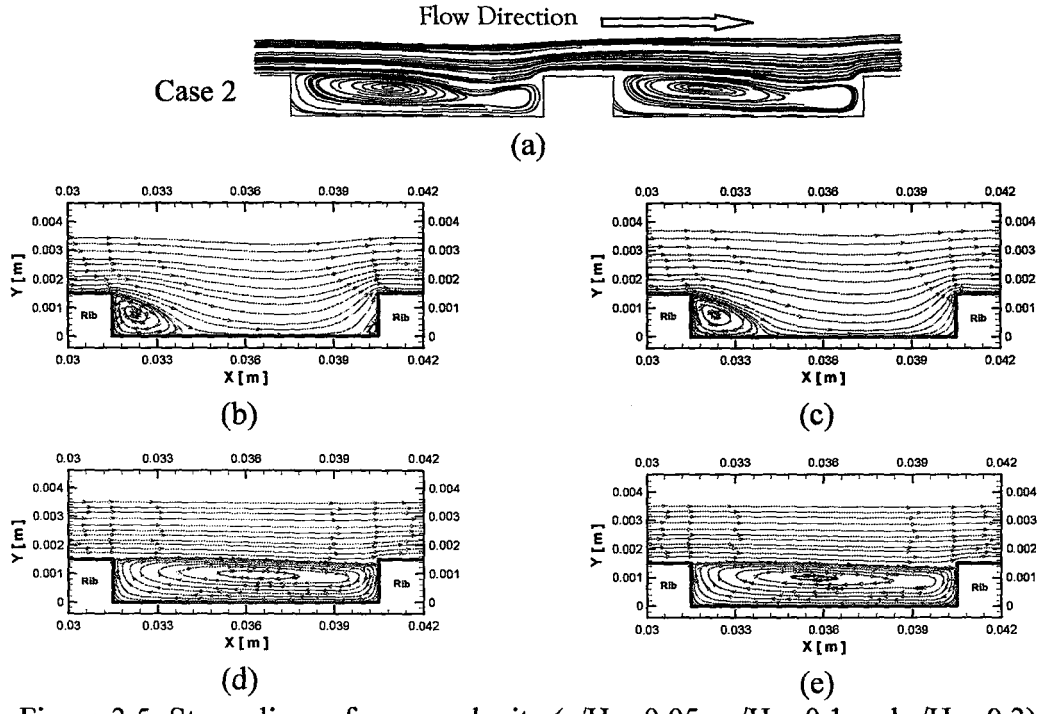

Figure 3.5: Streamlines of mean velocity (e/H = 0.05, w/H = 0.1 and s/H = 0.3) (a) DNS [36] (b) $k-\varepsilon$ (c) RNG $k-\varepsilon$ (d) *SST* (e) ω-*RSM* turbulent models.

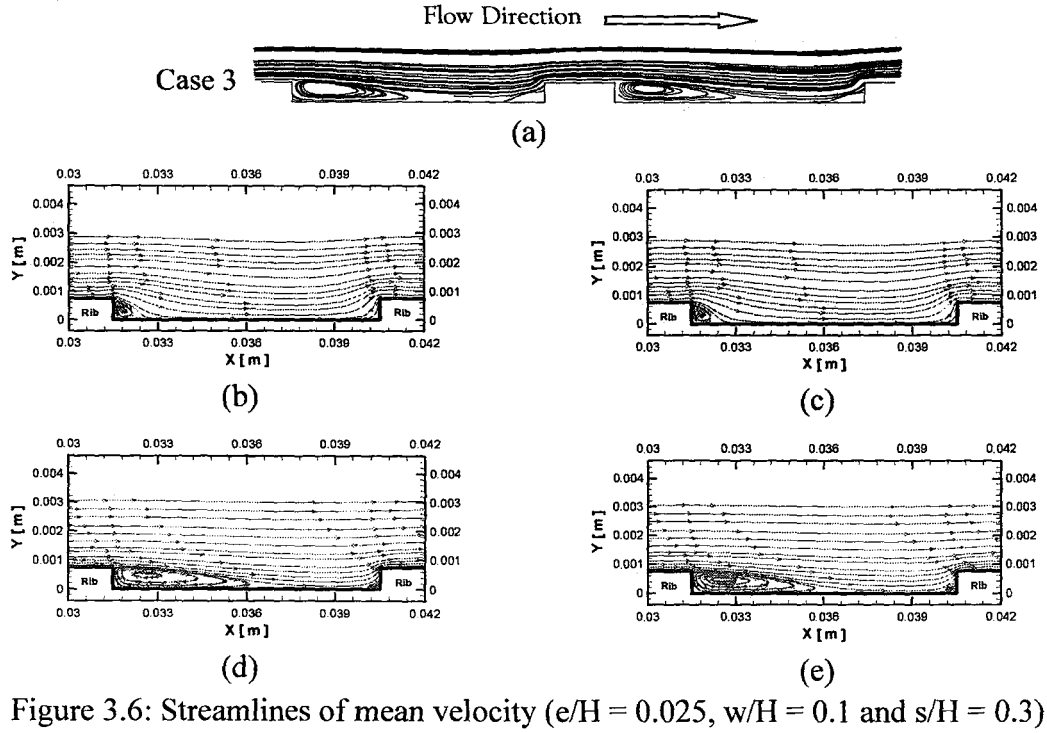

Figure 3.6: Streamlines of mean velocity (e/H = 0.025, w/H = 0.1 and s/H = 0.3) (a) DNS [36] (b) $k-\varepsilon$ (c) RNG $k-\varepsilon$ (d) *SST* (e) ω-*RSM* turbulent models.

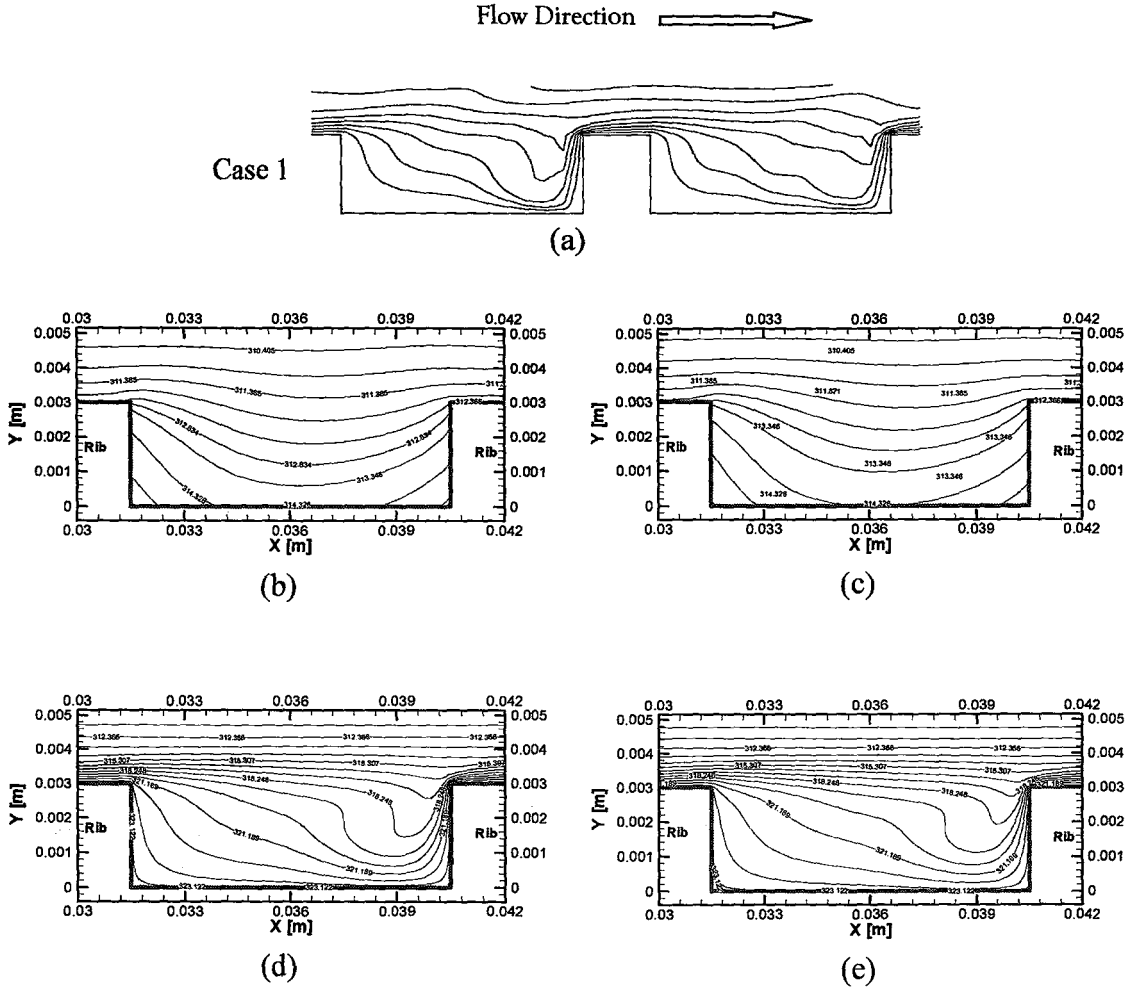

Figure 3.7: Contours of mean temperature (e/H = 0.1, w/H = 0.1 and s/H = 0.3) (a) DNS [36] (b) $k-\varepsilon$ (c) RNG $k-\varepsilon$ (d) *SST* (e) *ω-RSM* turbulent models.

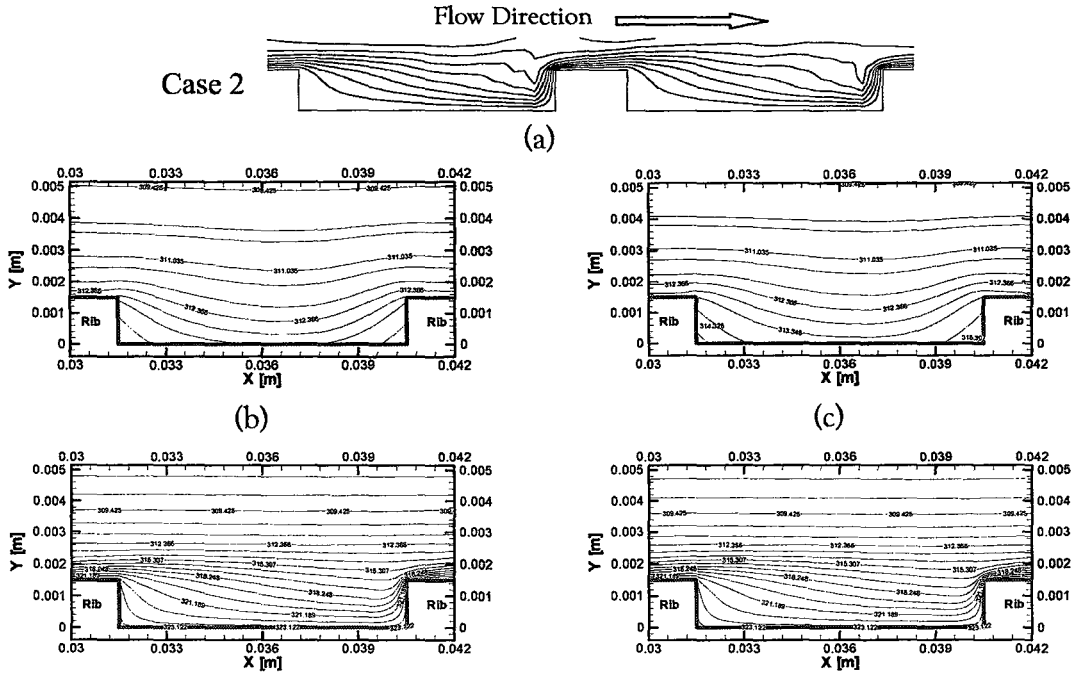

Figure 3.8: Contours of mean temperature (e/H = 0.05, w/H = 0.1 and s/H = 0.3) (a) DNS [36] (b) $k-\varepsilon$ (c) RNG $k-\varepsilon$ (d) *SST* (e) *ω-RSM* turbulent models.

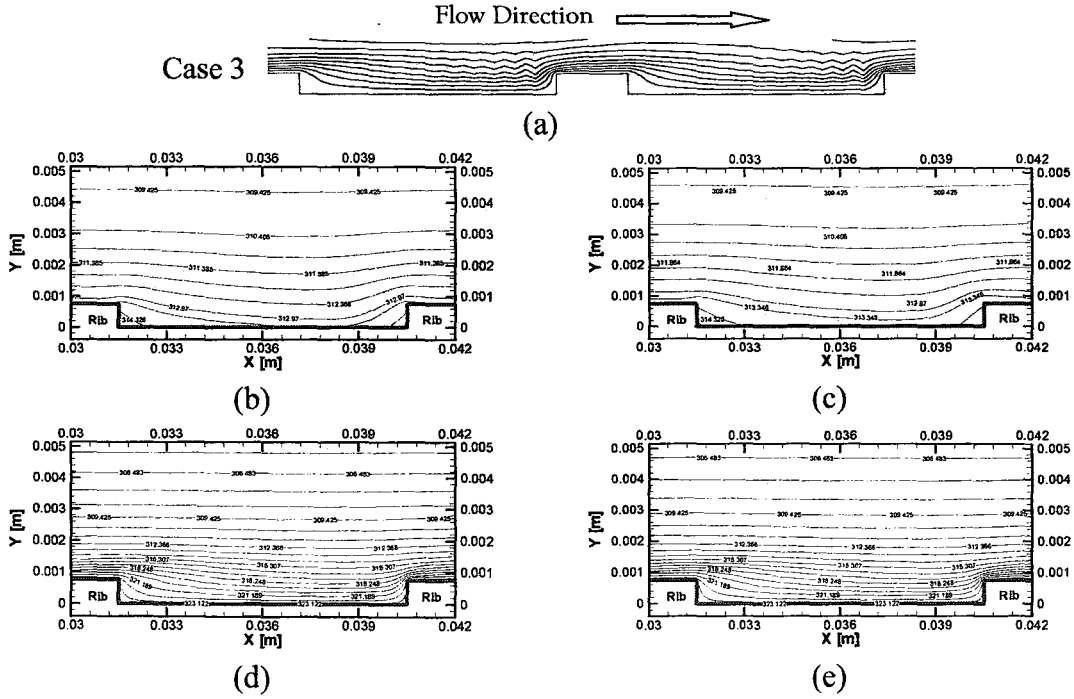

Figure 3.9: Contours of mean temperature (e/H=0.025, w/H = 0.1 and s/H = 0.3) (a) DNS [36] (b) $k-\varepsilon$ (c) RNG $k-\varepsilon$ (d) *SST* (e) *ω-RSM* turbulent models.

The velocity profiles at the middle of the channel for the three cases studied along with the no-ribbed case (e/H=0) is shown in Figure 3.10. This figure reveal once more that both the *ω-RSM* and *SST* model perform better than the $k-\varepsilon$ and *RNG* $k-\varepsilon$ models because they are able to capture the recirculation zones in the enclosures between ribs. However, these models have not yet revealed the physics of the flow in detail, as can be seen by comparing the velocity profiles of case 1,2, and 3 obtained by DNS with those obtained by the candidate models, Figures 3.10-c, 3.10-d, and 3.10-e. The DNS results show asymmetry of the velocity profile, while the candidate models show a more symmetric profile than that of the DNS. On the other hand, the velocity profiles from DNS exhibit a shift in cases 1 and 2 for maximum velocity occurrence towards the upper wall as the rib to channel height ratio, e/H, increases, Figure 3.10-a . Figure 3.10-b shows the resemblance between the profiles obtained using the SST model with that obtained from DNS, figure 3.10-a. Moreover, the $k-\varepsilon$ and *RNG* $k-\varepsilon$ models are clearly unable to see an adverse pressure gradient on the ribbed wall.

The profiles of turbulent quantities such as turbulent energy, Reynolds shear stress, and turbulent intensity are plotted at the middle of the channel in figures 3.13, 3.14, and 3.15 respectively. Figures 3.13 and 3.14 show that turbulence is promoted near the walls by increasing the element height. As shown the standard $k-\varepsilon$ and *RNG* $k-\varepsilon$ models over-predict turbulent Reynolds shear stress value at the ribbed wall region compared with DNS results. This over-prediction is due to the fact that these models over predict the production term at stagnation points region (section 2.7.1). This behaviour clearly makes these models – with the use of wall function – unsuitable for solving such problems. On the other hand the SST and *ω-RSM* models show turbulent kinetic energy and turbulent shear stress profiles more or less flattened close to the walls. This behaviour is related to eddy viscosity that is nearly zero close to walls (laminar flow regions) as shown in figure 3.11. In figure 3.15, the turbulent intensity profile exhibit an over-predicted value at the ribbed wall region in the standard $k-\varepsilon$ and *RNG* $k-\varepsilon$ models, while the *ω-RSM* and *SST* model predict a more realistic trend for this quantity. On the other hand, although the *ω-RSM* and *SST* turbulent models have a more acceptable behaviour for turbulent

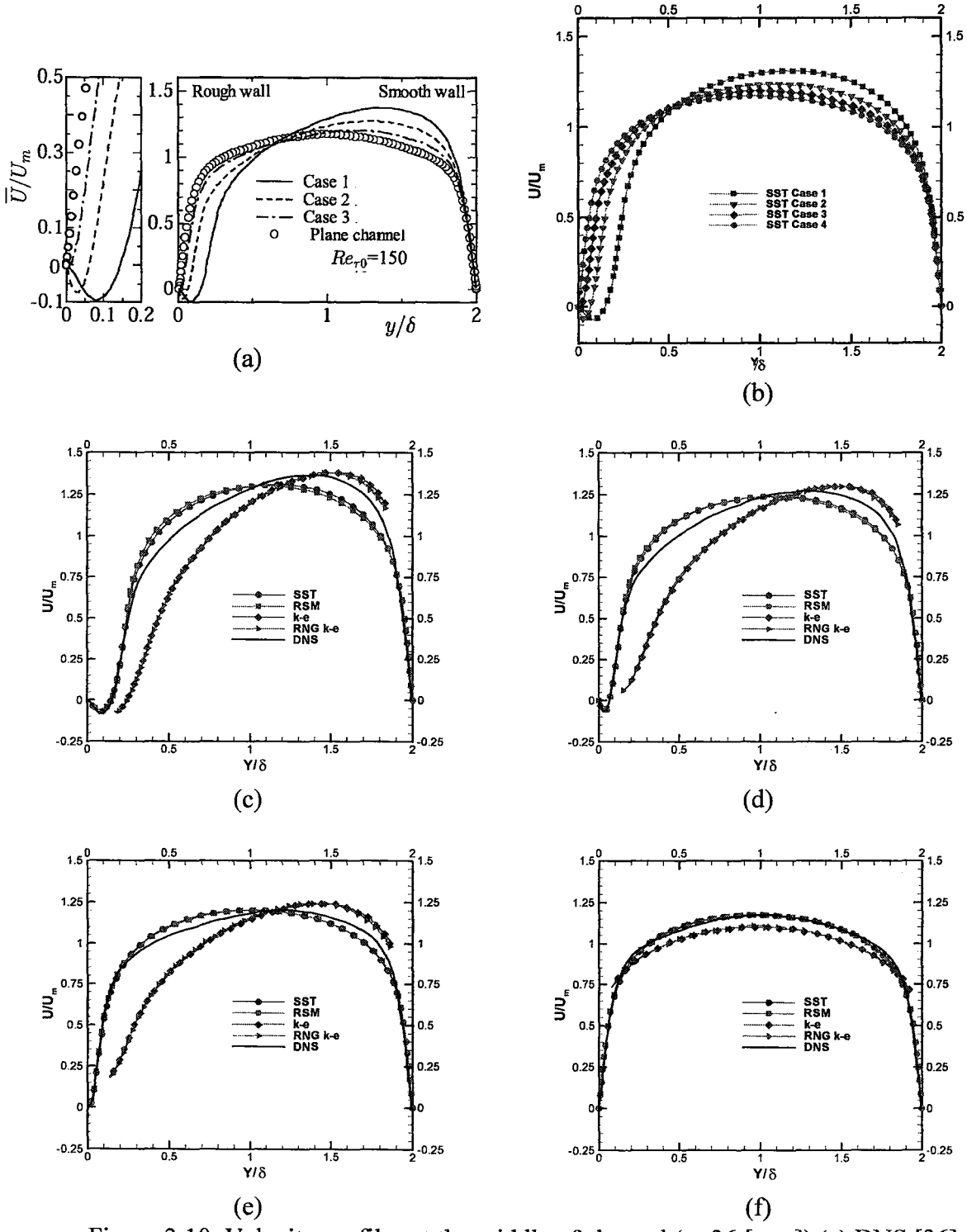

Figure 3.10: Velocity profiles at the middle of channel (x=36 [mm]) (a) DNS [36], (b) SST model (c) case 1 (*e/H=0.1*), (d) case 2, (*e/H=0.05*), (e) case 3, (*e/H=0.025*), (f) case 4, (*e/H=0*)

quantities (figures 3.13, and 3.14) such as turbulent energy and Reynolds shear stress, they under-predict the values obtained from the DNS. This behaviour could be attributed to under predicting the production term (section 3.2) in these models due to under predicted velocity gradient as shown in figure 3.12. Also, flow structure close to the walls is three dimensional while this study is assuming a two-dimensional flow which might be a possible explanation for lower value predictions.

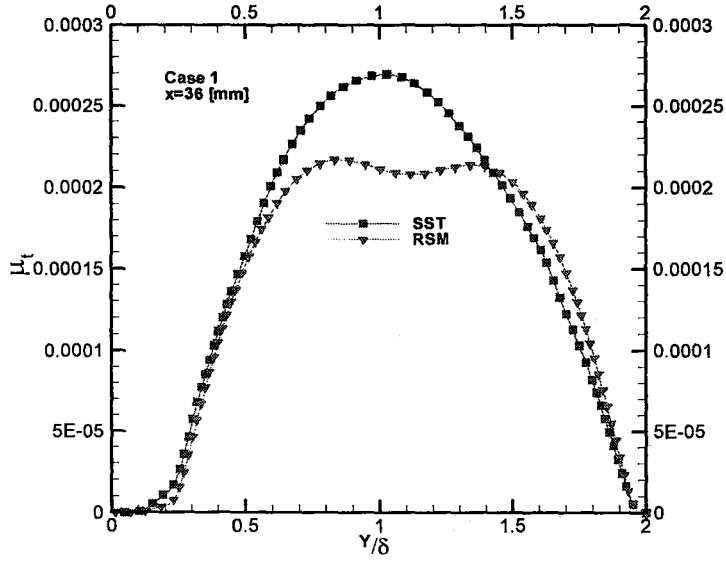

Figure 3.11 Eddy viscosity profile at x=36 [mm], case 1 (*e/H=0.1*)

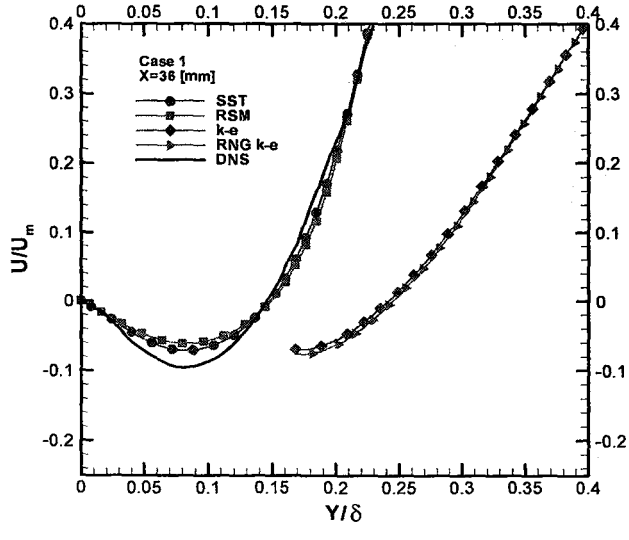

Figure 3.12 Velocity profiles near the lower hot ribbed wall at x=36 [mm], case 1 (*e/H=0.1*)

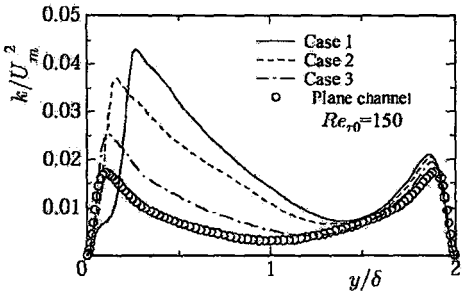

(a)

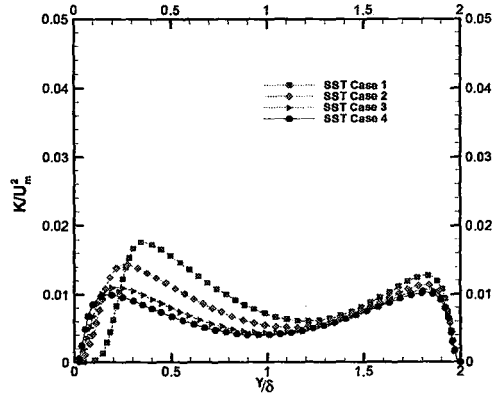

(b)

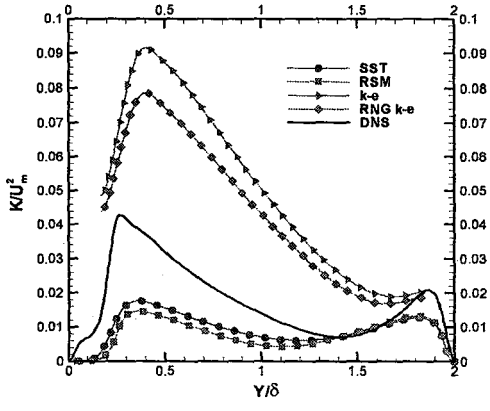

(c)

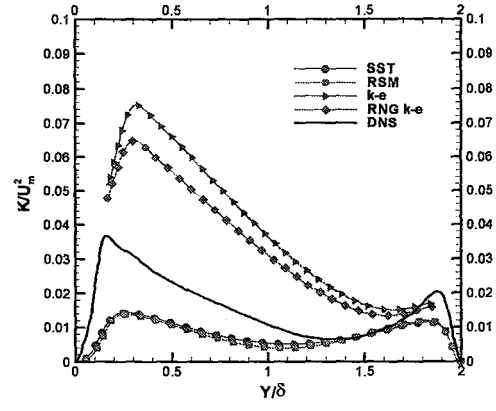

(d)

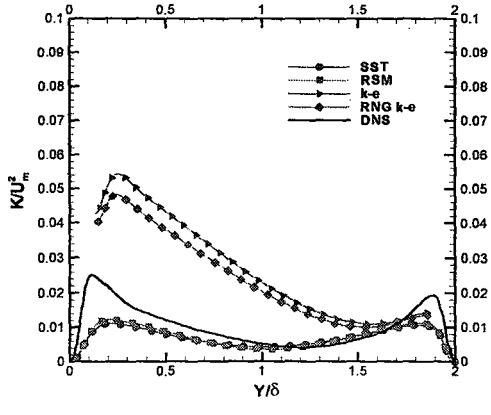

(e)

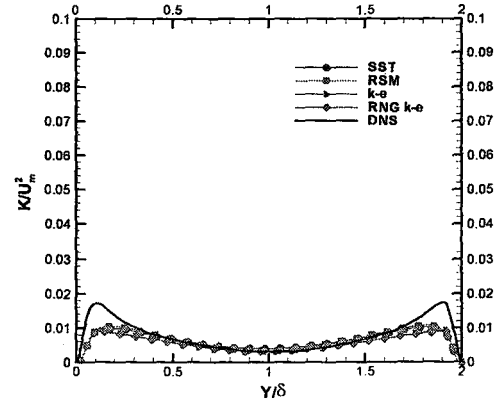

(f)

Figure 3.13: Turbulent energy profile at the middle of channel (x=36 [mm]) (a) DNS [36], (b) SST model (c) case 1 (*e/H=0.1*), (d) case 2, (*e/H=0.05*), (e) case 3, (*e/H=0.025*), (f) case 4, (*e/H=0*)

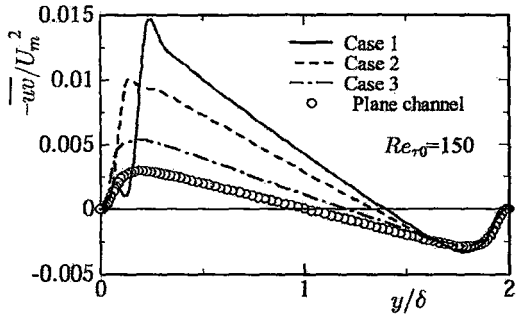

(a)

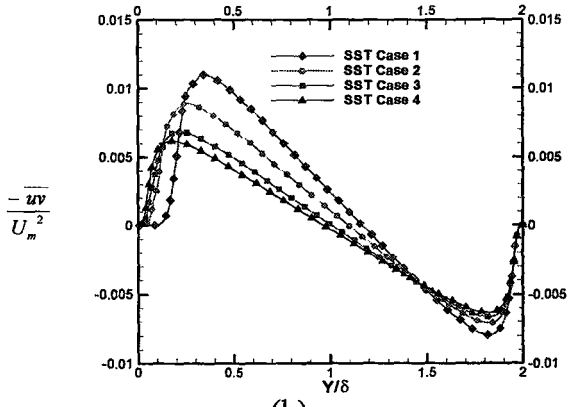

(b)

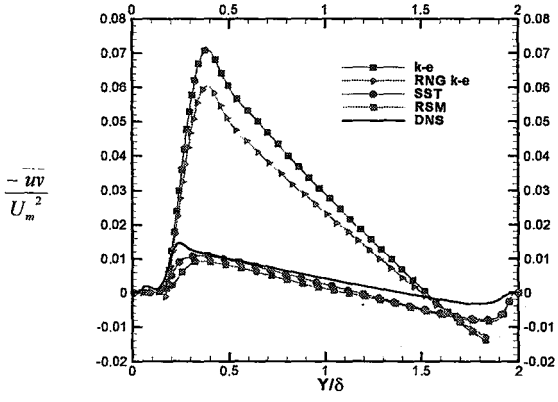

(c)

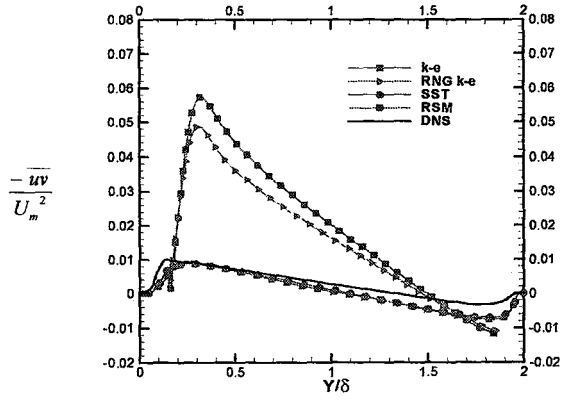

(d)

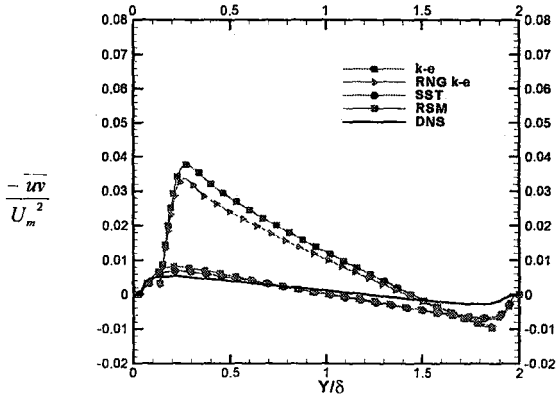

(e)

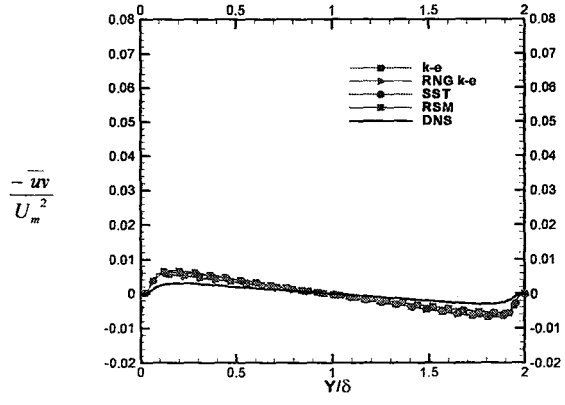

(f)

Figure 3.14: Reynolds shear stress profile at the middle of (x=36 [mm]) (a) DNS [36], (b) SST model (c) case 1 (*e/H=0.1*), (d) case 2, (*e/H=0.05*), (e) case 3, (*e/H=0.025*), (f) case 4, (*e/H=0*)

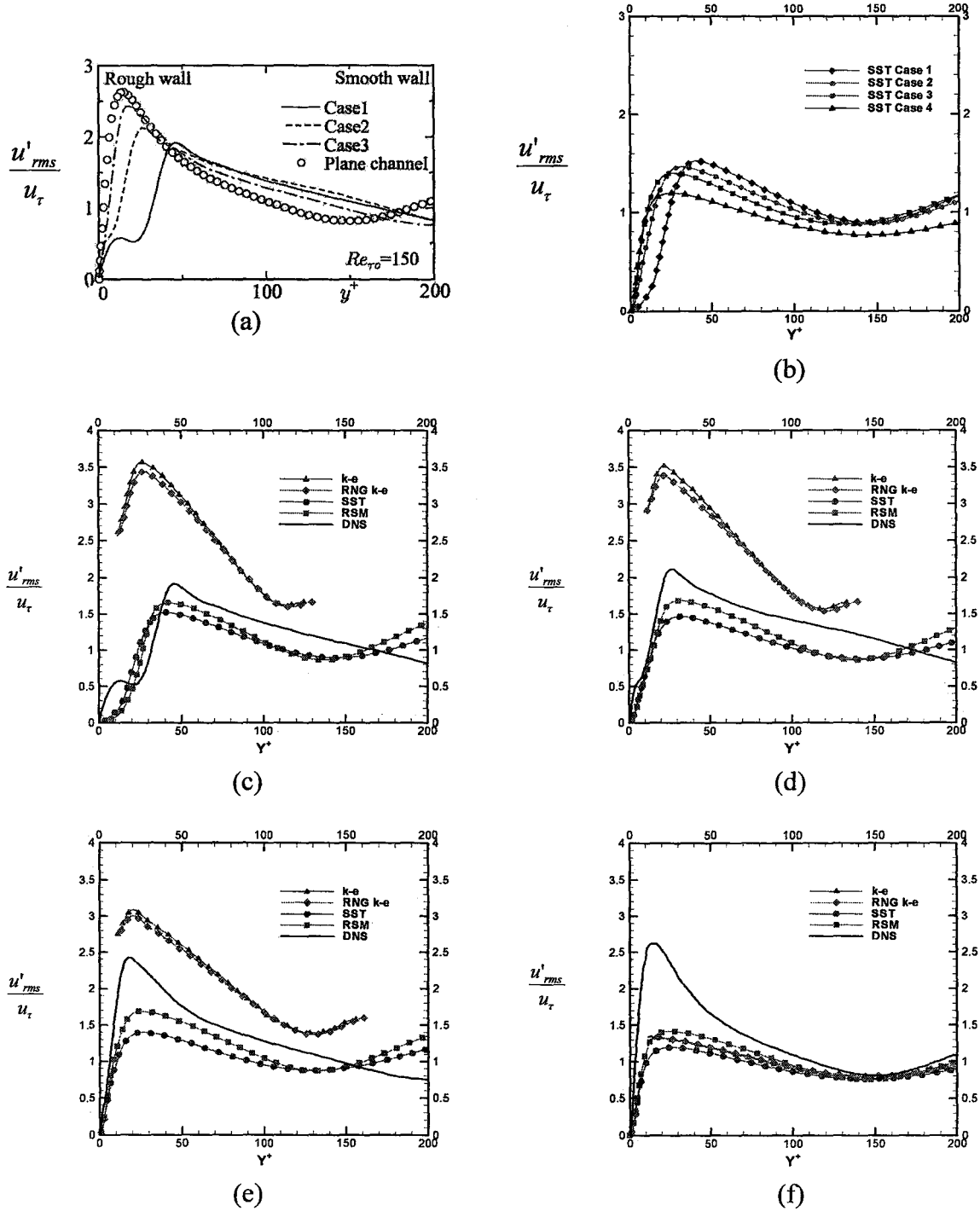

Figure 3.15: Turbulent intensity profile at the middle of channel (x=36 [mm]) (a) DNS [36], (b) SST model (c) case 1 (*e/H=0.1*), (d) case 2, (*e/H=0.05*), (e) case 3, (*e/H=0.025*), (f) case 4, (*e/H=0*)

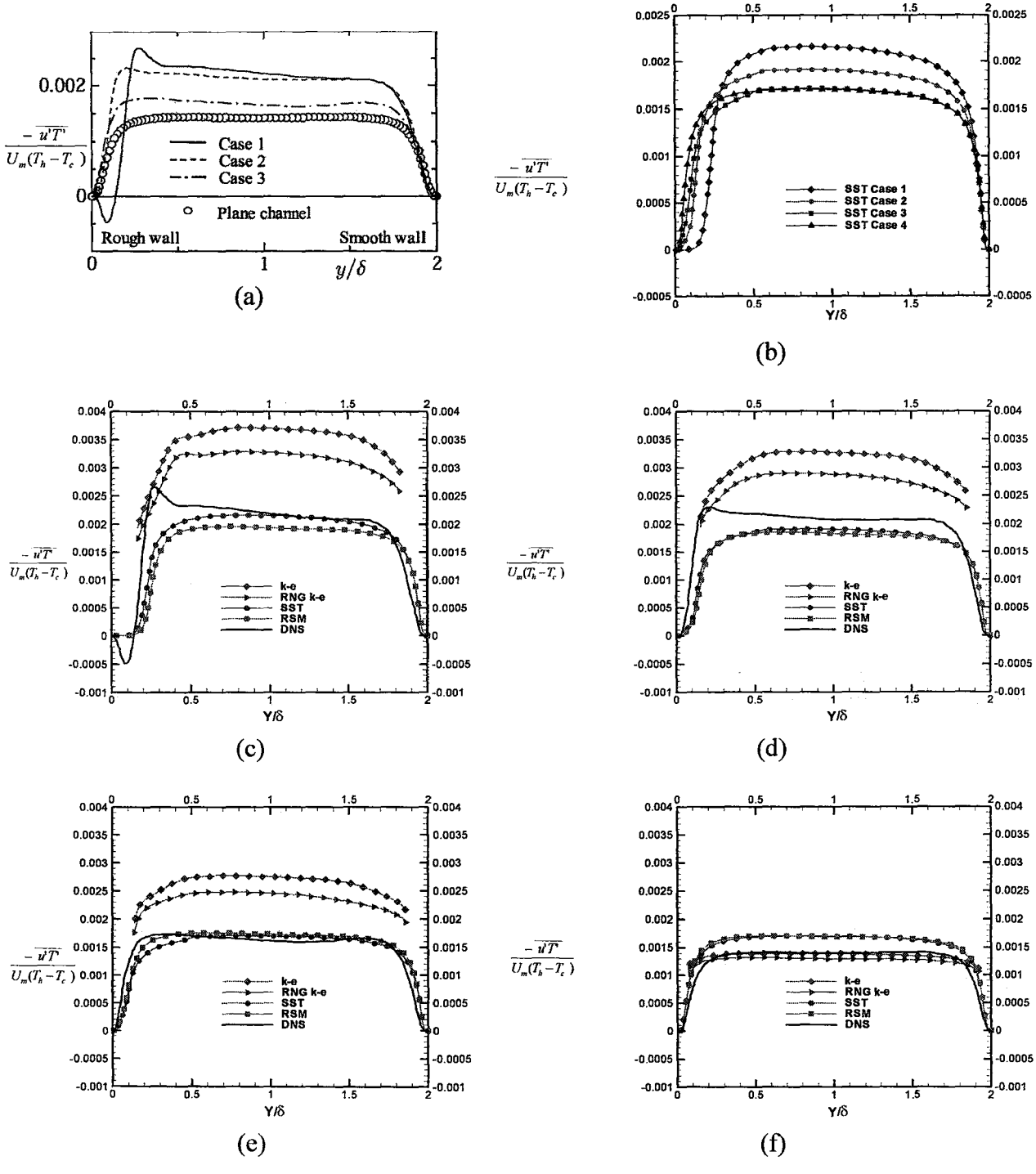

Figure 3.16: Turbulent heat flux profile at the middle of channel (x=36 [mm]) (a) DNS [36], (b) SST model (c) case 1 (*e/H=0.1*), (d) case 2, (*e/H=0.05*), (e) case 3, (*e/H=0.025*), (f) case 4, (*e/H=0*)

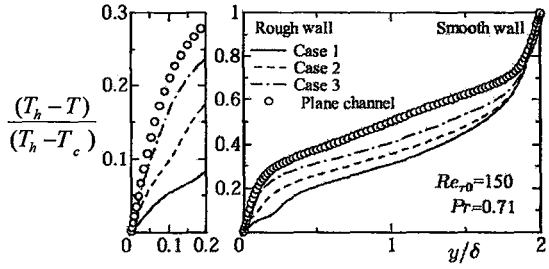

(a)

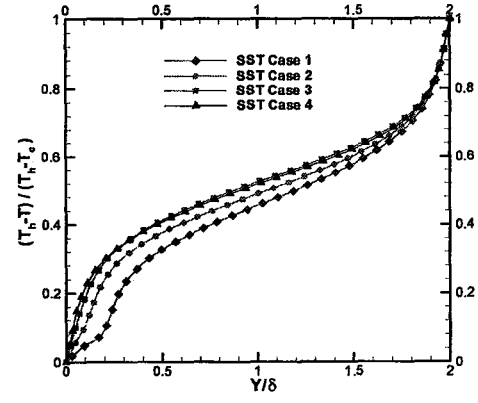

(b)

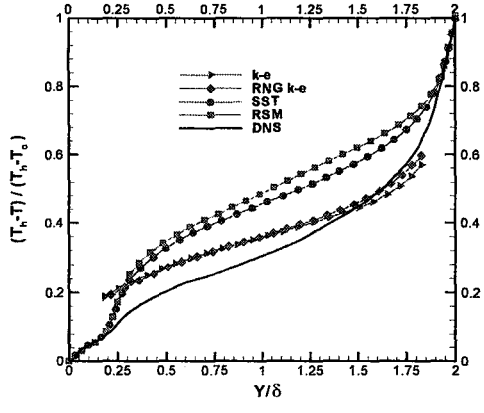

(c)

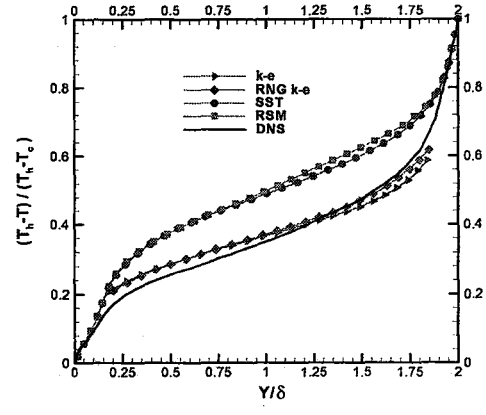

(d)

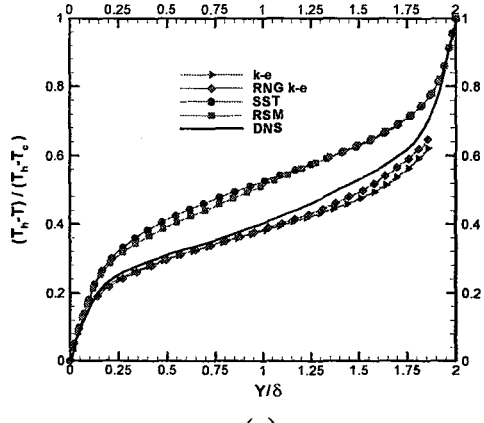

(e)

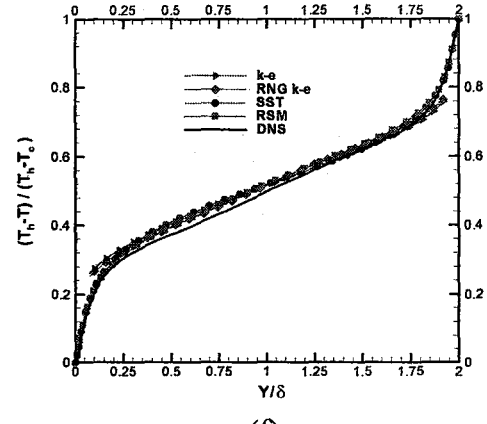

(f)

Figure 3.17: Mean temperature profile at the middle of channel (x=36 [mm]) (a) DNS [36], (b) SST model (c) case 1 (*e/H=0.1*), (d) case 2, (*e/H=0.05*), (e) case 3, (*e/H=0.025*), (f) case 4, (*e/H=0*)

The turbulent heat flux profiles for the four case studies obtained using different turbulent models are shown in figure 3.16. Compared with DNS results the $k-\varepsilon$ and the RNG $k-\varepsilon$ models are still over predicting the DNS values, however, the SST and the *ω-RSM* models are predicting the DNS profile very well especially for lower rib height. Figure 3.17 shows the dimensionless temperature profiles from different turbulent models compared with that from DNS. This is the only case where the SST and the *ω-RSM* models over predict the DNS results while the $k-\varepsilon$ and RNG $k-\varepsilon$ models match the DNS results much better.

3.4 Comparison with Experimental Data

The flow and heat transfer between two infinite parallel smooth plates (two-dimensional channel) is solved numerically and the results obtained using different turbulence models are compared with previous experimental [37] results.

Figure 3.18 shows the geometry of the problem solved. The origin of the coordinate system is at the lower corner of the channel entrance. The channel height is $H = 300\ [mm]$ and its length is L=841 mm. The channel walls are adiabatic, except for the portion in the middle of the lower wall of length 441 mm that is exposed to a constant heat flux of 750 W/m^2K [15]. Two unheated portion at entrance and exit of the channel are each of length $L_{Enterance} = L_{Exit}$ =200 mm. Air enters the channel as a fully developed turbulent flow with a mean velocity of $U_m = 10\ m/s$ and follows the one-seventh-power law, Equation 2.1, with ambient temperature of $T_{inlet} = T_{ref} = 26.15^oC$ [15].

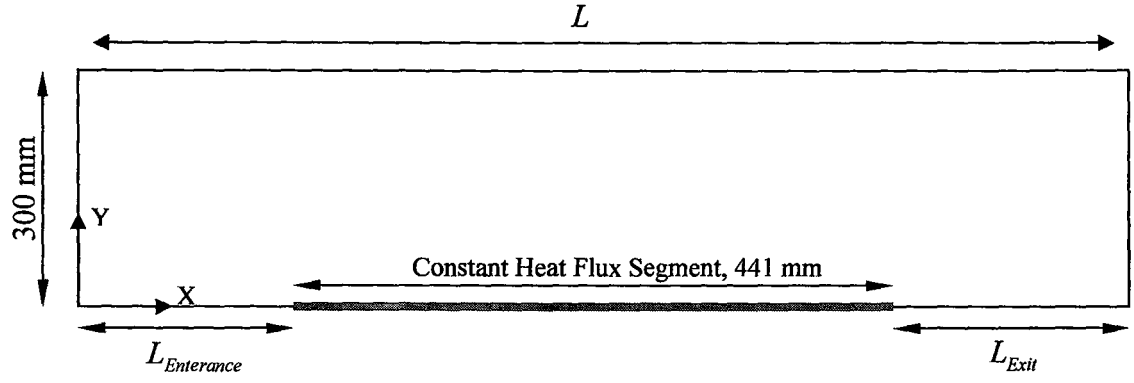

Figure 3.18 Schematic geometry of the first problem

Another geometry used in the comparison with the experimental data of [37], differs from the first in that the constant heat flux portion of lower channel wall is exchanged for a rib configuration. In the second geometry, heat flux is applied only on the top surface of the ribs, as shown in figure 3.19.

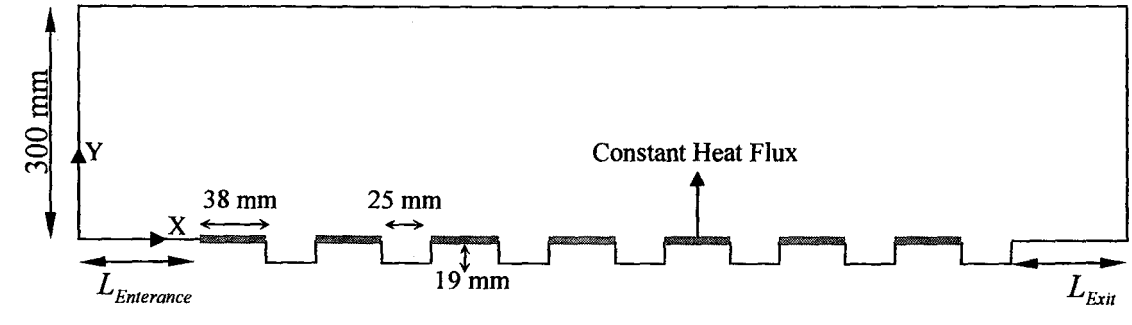

Figure 3.19 Second geometry of the second problem

For all meshes used, the y^+ values were in the order of unity. Mesh-independent solutions were sought for all models using structured meshe, with high mesh densities in the vicinity of walls in order to resolve the high gradients of both hydrodynamic and thermal boundary layers. In this practice, the total number of hexahedron elements was about 150,000 for the first problem and about 220,000 for the second problem.

3.4.1 Results and Discussions

Figure 3.20 and 3.21 show wall heat transfer coefficient profiles on the constant heat flux segments of the lower channel wall for the first and second geometries, respectively. Numerical data in both figures display a fall in the wall heat transfer coefficient (instead of having a zero value) at the margin of constant heat flux and lower wall adiabatic condition, because of the existence of singularity points in the numerical solution.

Heat transfer coefficient profiles in both figures show that both the SST and the *ω-RSM* turbulence model are closer to the previous data than *k-ε* and *RNG k-ε* models. The turbulence heat transfer solution depends not only on the turbulent models (*k-ε, RNG k-ε, SST*, and *ω-RSM*) but also on turbulent Prandtl number, Pr_t, which is taken as a constant value of 0.9 through this work.

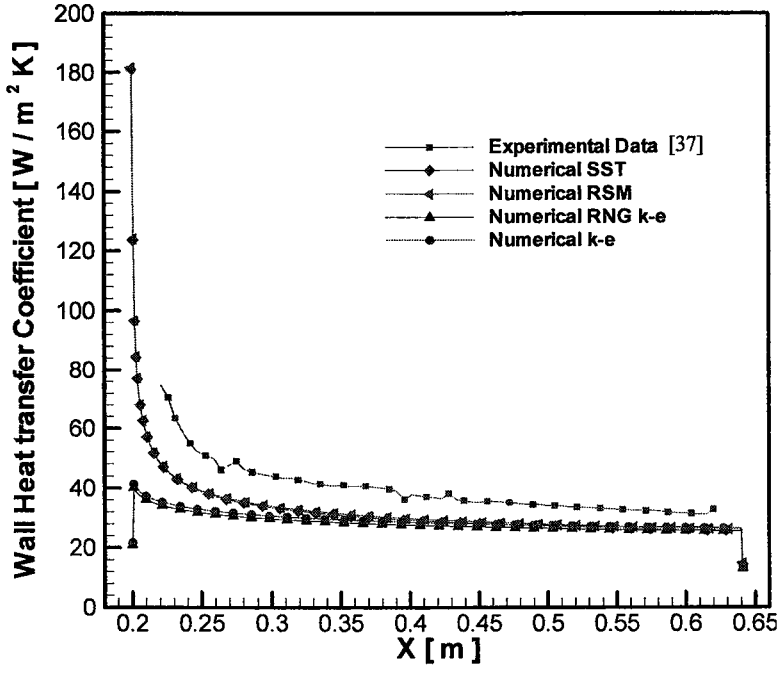

Figure 3.20 Wall heat transfer coefficient of the first problem (a) Full view

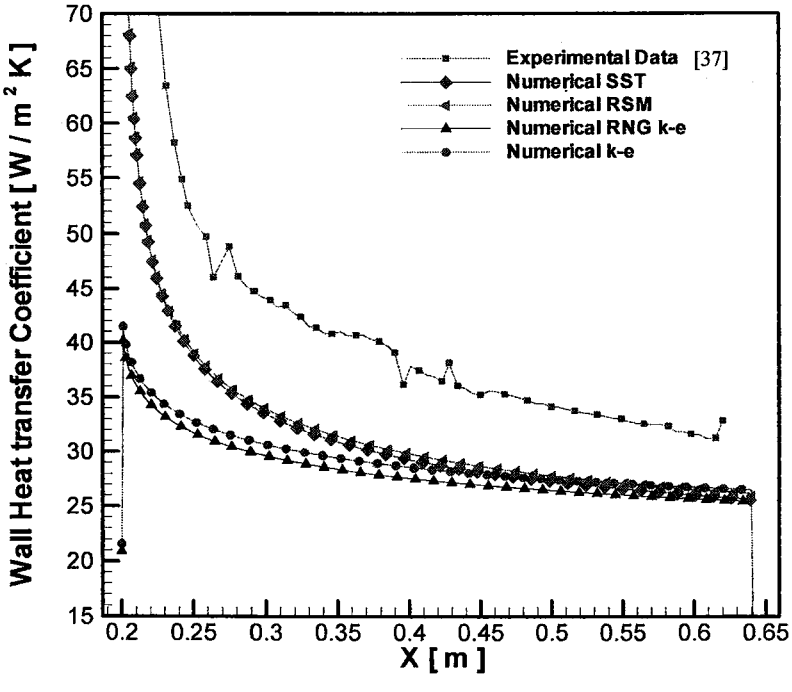

Figure 3.20 Wall heat transfer coefficient of the first problem (b) Close view

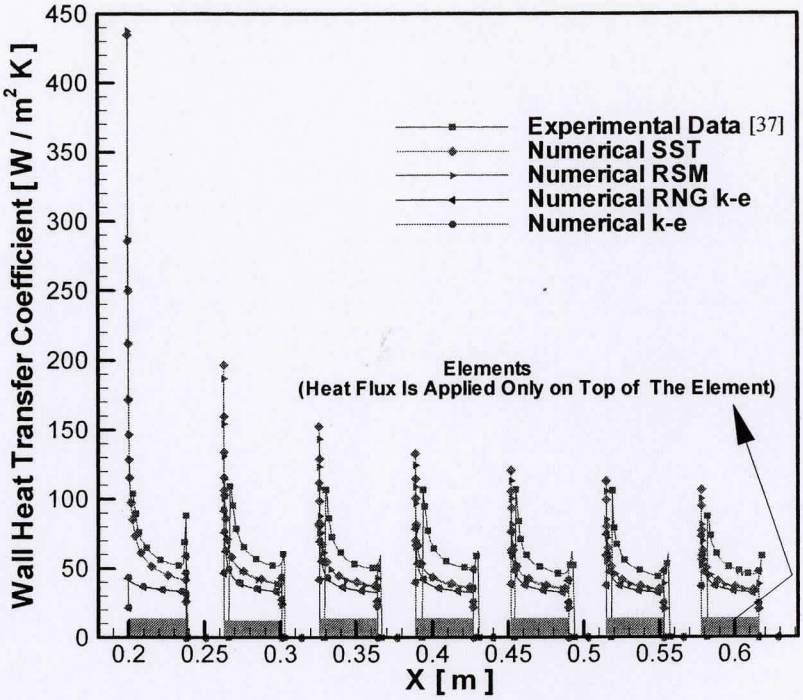

Figure 3.21 Wall heat transfer coefficient of the second problem (a) Full view

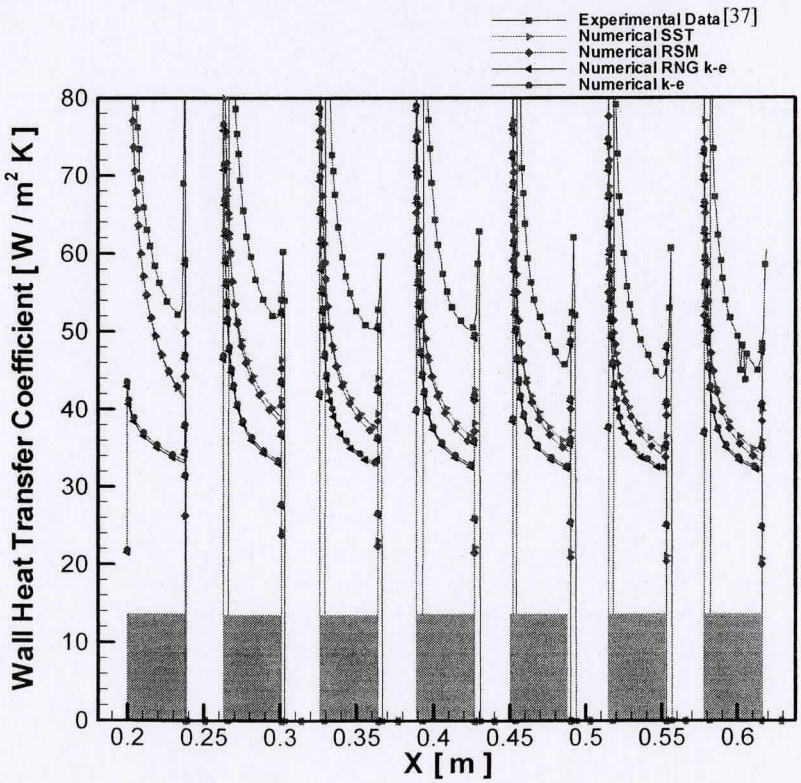

Figure 3.21 Wall heat transfer coefficient of the second problem (b) Close view

3.5 Comparison with Previous Experimental Data

3.5.1 Problem Description

Figure 3.22 depicts the geometry of this problem. The origin of the coordinate system is located at the lower corner of the channel entrance. The two plates are a distance $H = 44.9$ $[mm]$ apart (channel height), and are adiabatic except for the ribs of the lower channel wall that are exposed to a constant heat flux of 1199.622 W/m^2K applied to the sides and top surface of ribs [38]. The entrance length ($L_{Enterance}$) and exit length (L_{Exit}) are 200 mm and 400 mm respectively. Air enters the channel with fully developed turbulent velocity profile that follows the one-seventh-power law, Equation 2.1, and at ambient temperature ($T_{inlet} = T_{ref} = 25^oC$). Reynolds number based on the hydraulic diameter (78.277 mm) is varied from 2600 to 13000. The number of ribs used in this case was five ribs [38].

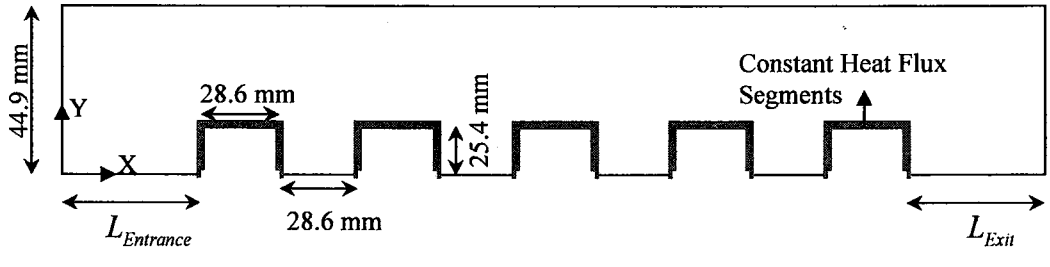

Figure 3.22 Schematic geometry of the experimental problem

For all meshes used, the values of y^+ were in the order of unity. Mesh-independent solutions were sought for the SST model with Reynolds number of 13000 using

structured meshes with higher mesh densities in the vicinity of walls. In this practice, the total number of hexahedron elements was about 125,000.

3.5.2 Results and Discussions

Table 3.2 shows the tabulated data obtained from experiments [38] and the numerical results of the current study using the SST turbulent model to show the percentage error associated with the model. As shown, within the transition range [38] ($2600 \leq \mathrm{Re}_H \leq 4300$) the experimental data and numerical results have a large discrepancy over all of the rows. In the turbulent flow regime ($\mathrm{Re}_H > 4300$), however, the discrepancies are concentrated on the first, second, and last row, where streamlines are distorted. Also, the average Nusselt number is shown to be closer to experiments at the middle of the channel, where flow is more stratified.

The reason for the difference may be that the SST model lacks accuracy for high aspect ratio elements [18]. As shown in section 2.7.2, the model's mathematical structure is insensitive to $\frac{\partial \overline{V}}{\partial x}$ velocity gradient. In addition, the flow encountering the first two ribs and leaving the last rib has strong three-dimensional characteristics. As shown in figure 3.23, the vortices interfere which other and multipair together. This process extracts energy from the higher to the lower energy vortices and mixes the flow downstream of the step, which causes rapid growth of the shear layer. The region downstream of the splitter plate has a high velocity gradient, and flow upstream of reattachment point is shown to have a fully three-dimensional turbulent structure [41].

Table 3.2 Top surface average Nusselt number over the of five ribs

Re_H Number	Nusselt Number Based on	First Obstacle Values and Discrepancy		Second Obstacle Values and Discrepancy		Third Obstacle Values and Discrepancy		Fourth Obstacle Values and Discrepancy		Fifth Obstacle Values and Discrepancy	
2600	Experimental	30.77	58%	31.45	19%	25.87	25%	24.21	31%	23.91	37%
	Numerical	12.97		25.53		19.46		16.64		15.02	
4300	Experimental	43.74	50%	42.64	7%	36.84	20%	33.77	25%	32.86	30%
	Numerical	21.75		39.47		29.57		25.43		23.10	
6000	Experimental	49.84	39%	44.25	16%	37.63	3%	34.24	3%	33.79	10%
	Numerical	30.32		51.50		38.60		33.37		30.45	
7000	Experimental	57.61	39%	49.64	17%	42.97	1%	38.94	3%	38.19	10%
	Numerical	35.26		58.02		43.60		37.79		34.54	
8000	Experimental	65.32	39%	54.84	17%	48.19	0%	43.52	3%	42.46	9%
	Numerical	40.16		64.30		48.42		42.08		38.53	
9000	Experimental	72.97	39%	59.87	17%	53.33	0%	48.00	4%	46.62	9%
	Numerical	44.91		70.35		53.09		46.23		42.39	
10000	Experimental	80.56	39%	64.77	18%	58.39	1%	52.41	4%	50.69	9%
	Numerical	49.51		76.25		57.64		50.29		46.16	
11000	Experimental	88.11	39%	69.54	18%	63.38	2%	56.74	4%	54.67	9%
	Numerical	53.92		82.02		62.09		54.25		49.85	
12000	Experimental	95.62	39%	74.21	18%	68.30	3%	61.00	5%	58.59	9%
	Numerical	58.18		87.69		66.45		58.14		53.49	
13000	Experimental	103.09	40%	78.77	18%	73.17	3%	65.21	5%	62.43	9%
	Numerical	62.24		93.20		70.65		61.91		57.04	

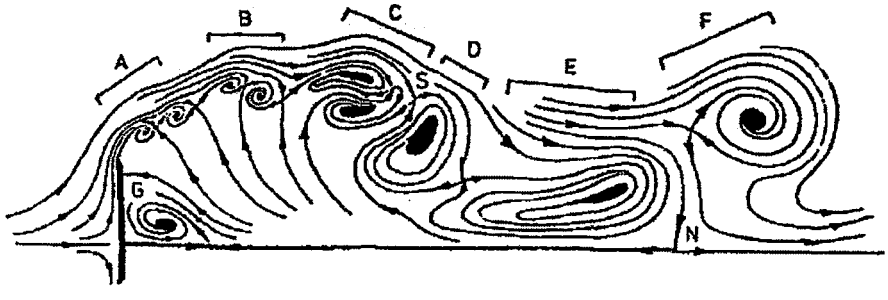

Figure 3.23 Instantaneous streamlines for flow over a flat plate with plate separator [41]

Figure 3.24 shows the flow over backward facing step. In this kind of flow, the separated shear layer rapidly dives down and forms a sharp curve. In this process, part of the shear layer detours upstream into the recirculation zone because of the downstream adverse pressure gradient. In the recirculation region, the back-flow velocity usually exceeds 20% of the free stream flow [41], which shows there are high interactions in this region.

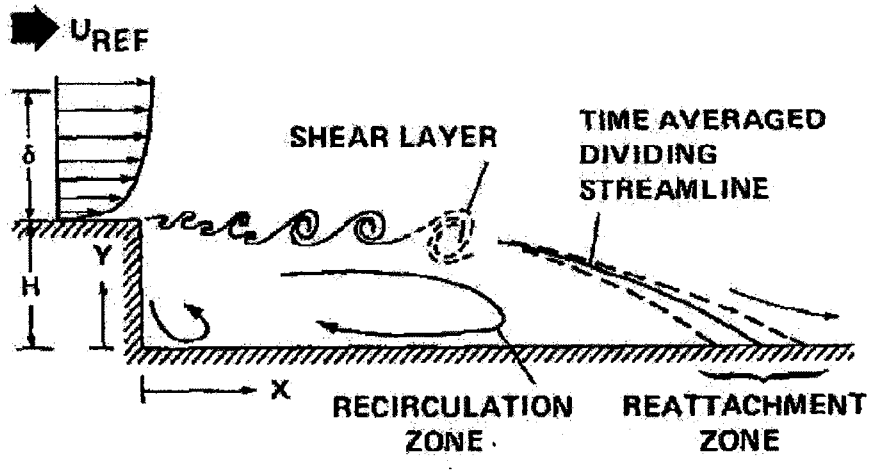

Figure 3.24 Characteristics of backward step flow [41]

3.6 Conclusions and Recommendations

The lack of sensitivity of both $k-\varepsilon$ and RNG $k-\varepsilon$ models to the adverse pressure gradients, separation, and, hence, the ability to capture phenomena such as those accruing in two-dimensional ribbed channel flow fields is mainly because these two models use wall functions to bridge the viscous sub-layer rather than solving for it. This characteristic means that they are not good choices for flow with separation, circulation, and reattachment. Better choices are the Omega Reynolds Stress Model (ω-RSM) and the

Shear Stress Transport model (SST) as they both equally exhibit a reasonable prediction of flow and thermal fields for the cases investigated in the current study.

Since ω-RSM is computationally more demanding, given that it solves more equations than the SST model with no significant improvement, it is recommended to use the Shear Stress Transport (SST) model to capture the features related to the flow and heat transfer of a convective flow field in a two-dimensional ribbed channel.

Although publications such that [42] claim that the SST model has a significant advantage in non-equilibrium boundary layer flows – including heat transfer predictions – this model needs to be tested further in more complex flow regimes, such as those which arise with more populated boards and with different heat fluxes as occurs with real thermal packages, in order to confirm its ability to handle such complex flows.

Chapter Four

Results and Discussion

4.1 Introduction

In this chapter turbulent flow and heat transfer in the ribbed channel are parametrically studied. The dimensions, such as element height, e element width, w and step width, s used in the parametric study, are normalized with respect to the channel height, H. In addition, throughout the chapter, temperature is presented in dimensionless form corresponding to equation 4.1.

$$T^* = \frac{(T - T_{ref})}{T_{ref}} \tag{4.1}$$

where T_{ref} is reference/inlet temperature, $T_{ref} = 25^o C$. The governing equations and all boundary conditions are described in detail and set as discussed in chapter two-mathematical modeling.

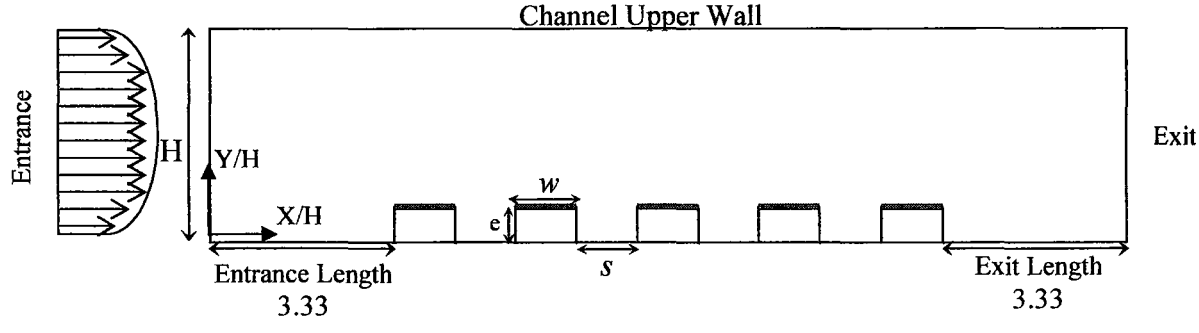

Figure 4.1 Geometry of the parametric study

4.2 Effect of Reynolds Number

To study the effect of Reynolds number on the flow and heat transfer field, the parameters such as the rib and channel dimensions were kept constant. The only variable was the mean inlet velocity. As Reynolds number increases, the nature of stratified streamlines above the first element changes.

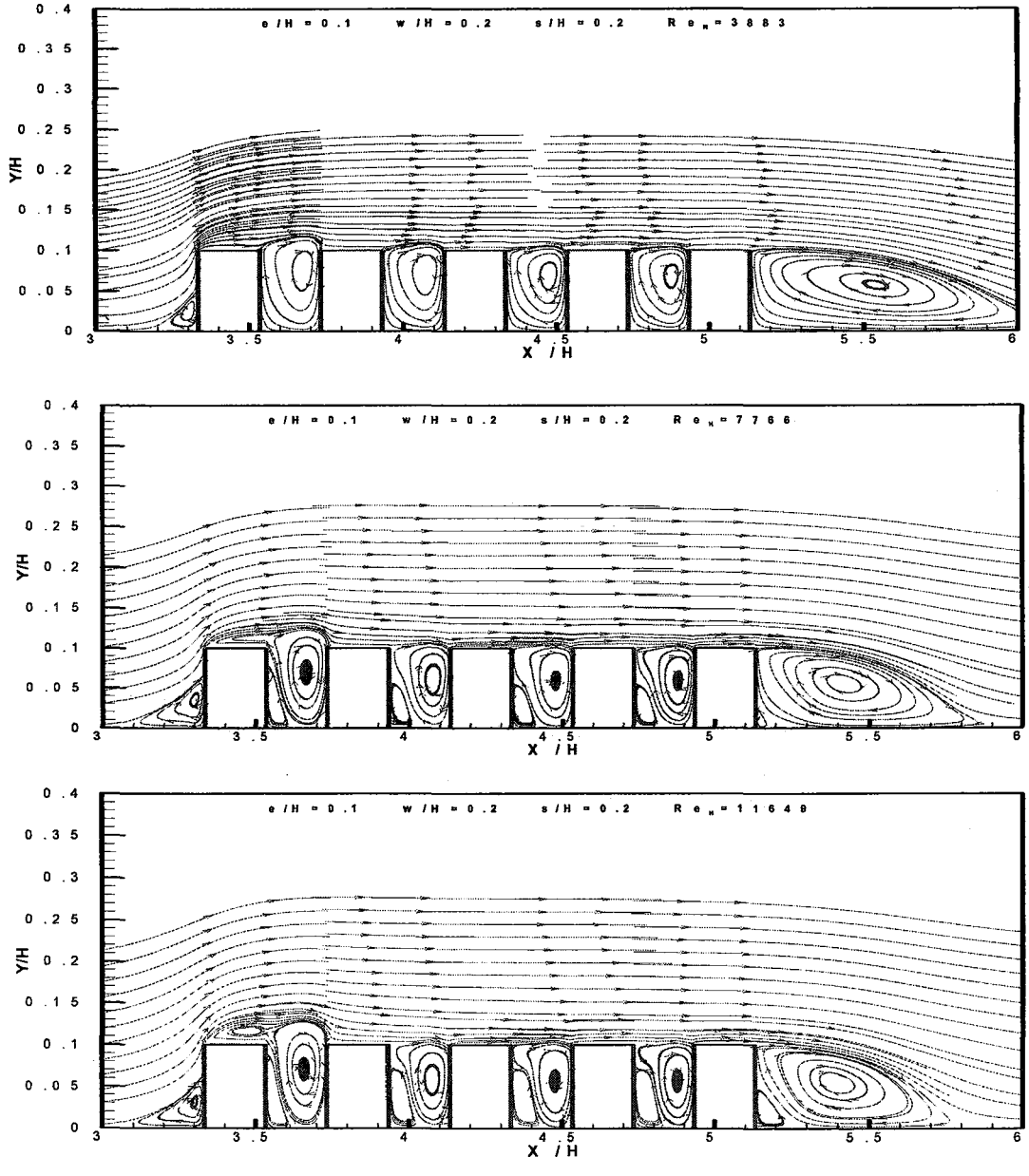

Figure 4.2 Streamline contours through the ribbed channel at different Reynolds number

At $Re_H = 7766$, the streamlines at the top of the first element form a circulation region which extends into the first step. This circulation traps the heat and prevents it from being removed by the free stream flow, and consequently the average Nusselt number decreases [9]. Increasing Reynolds number further, $Re_H = 11649$, the circulation zone continues developing, keeping the heat above the first element to interact freely with the free stream. Since both the circulation region and free stream flow rotate and move faster heat is more easily transferred and Nusselt number increases compared with the case of $Re_H = 7766$.

Forming the circulation region with increase of flow rate is due to higher velocity gradients in both the vertical and the horizontal direction. The circulation region on the top surface of the first element is as a result of vorticity vector, $\vec{\omega}$. The vorticity vector of a fluid element is related to velocity gradients by the following equation: [43]

$$\vec{\omega} = \nabla \times U \tag{4.2}$$

The component of this vorticity vector are:

$$\omega_x = \frac{\partial w}{\partial y} - \frac{\partial v}{\partial z}, \qquad \omega_y = \frac{\partial v}{\partial z} - \frac{\partial w}{\partial x}, \qquad \omega_z = \frac{\partial v}{\partial x} - \frac{\partial u}{\partial y} \tag{4.3}$$

in which ω_z is the major component responsible for forming the circulation zone above the first element. The velocity gradients of this component are found to be maximum at on the sharp edge of the first element. Figures 4.3 and 4.4 show the velocity vectors on the row of elements. In figure 4.3, velocity vectors are colored by change of the vertical component of the velocity, while figure 4.4 shows the same profiles with respect to stream-wise change of the velocity component. Circulation, by definition, is a flux of vorticity through an arbitrary loop-bounded surface, equation 4.4 [43]. This flux is found to be maximum at on the face edge of the first element.

$$\Gamma = \oint_A \vec{\omega} \cdot dA \tag{4.4}$$

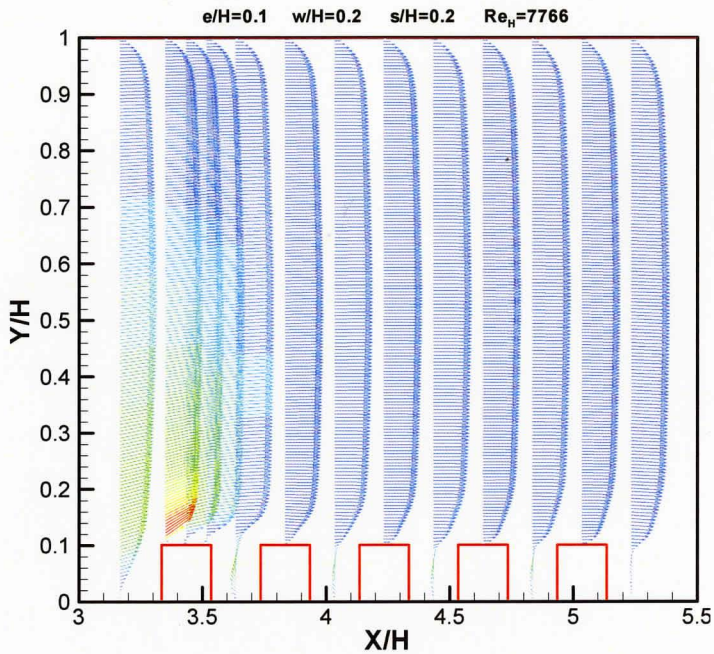

Figure 4.3 Velocity profile coloured by change in vertical component of velocity

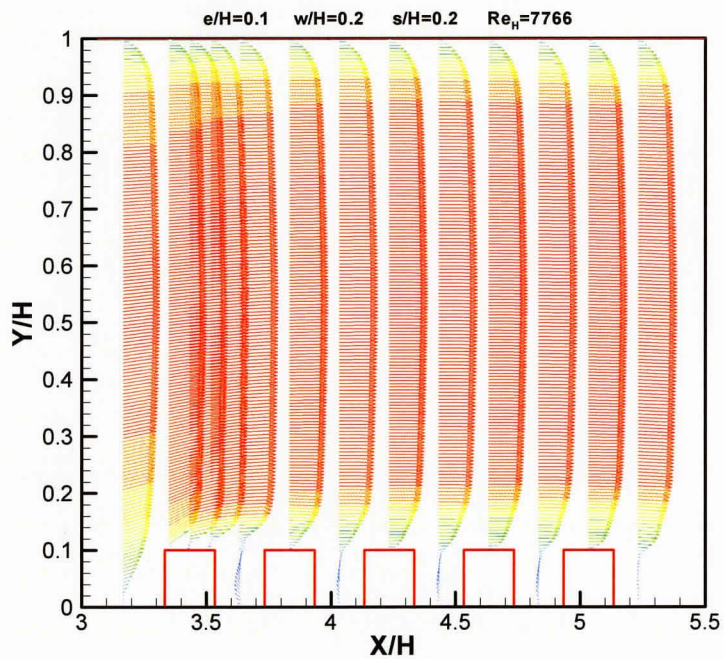

Figure 4.4 Velocity profile colored by change in the stream wise component of velocity

Contours of static pressure shown in figure 4.5 shows that the pressure in the domain and especially on the first element changes in both the axial and normal directions.

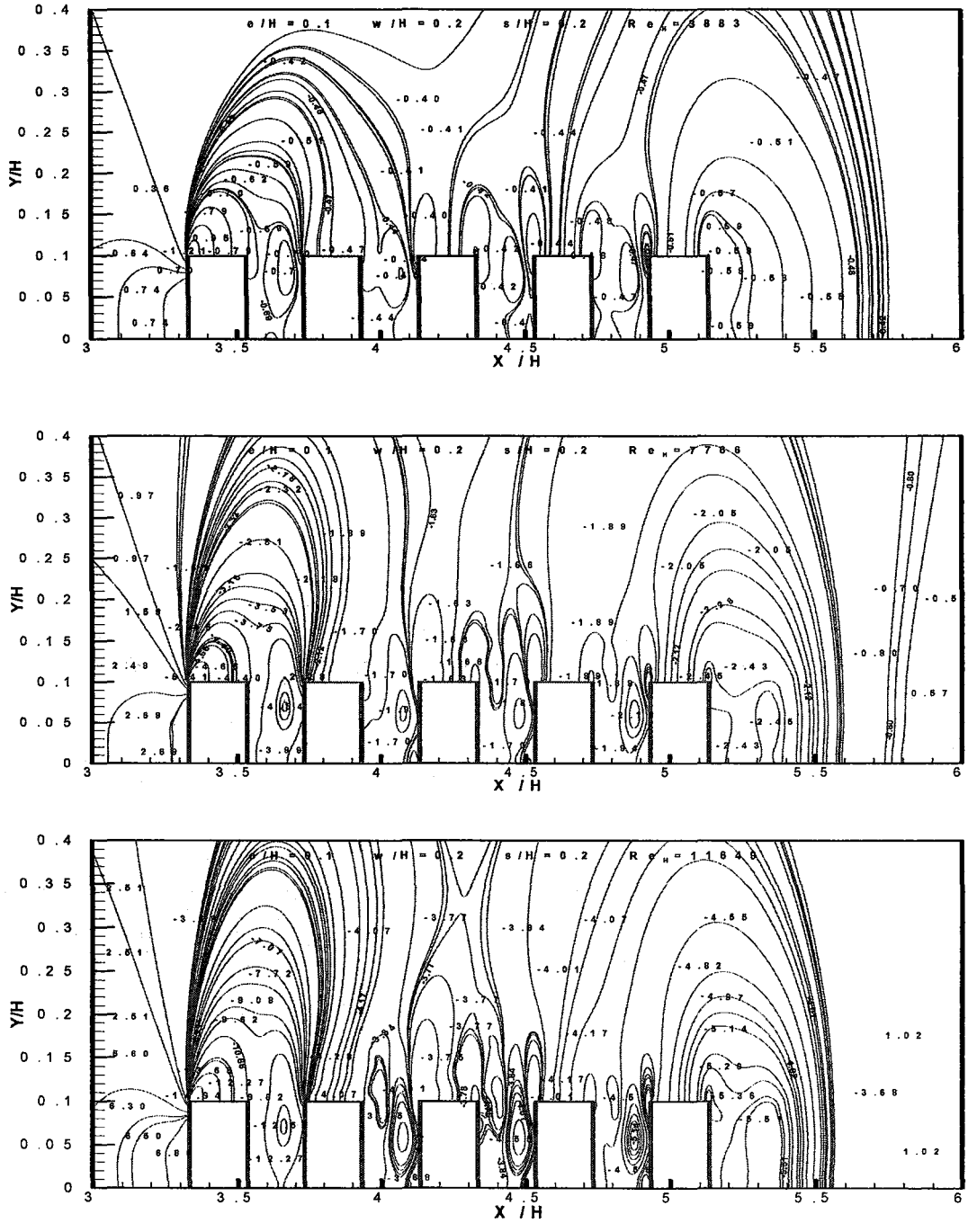

Figure 4.5 Relative static pressure contours at different Reynolds number [Pa]

Both changes are the result of detouring the flow by first row of elements. As the velocity increases, the pressure gradient in both directions increases. That is on the front and backward corners of the first element as well as in the vertical direction above. A positive stream-wise pressure gradient, when strong enough, breaks the shear layer above the first element [9]. The positive vertical pressure gradient prevents the broken shear layer from detaching and merging into the main stream by pushing the flow down towards the top surface of the element. Incorporating these effects simultaneously yields the circulation region above the first element.

It would be interesting to know that the balance of pressure gradients and shear force can move the center of the circulation zone. As we will see in section 4.3, with increasing the element height, the stream-wise positive pressure gradient increases, and, in order to find more equalized pressure levels, the broken shear layer travels further above the first element in the vertical direction to avoid a down-stream positive, adverse, pressure gradient. This effect results in a larger circulation zone, which extends itself even to the second row elements. As a result, the center of circulation zone moves on top of the first step. Further down, pressure gradients weaken and the flow stratifies.

Plots of dimensionless temperature contours are shown in figure 4.6. One should notice that the closer the lines to each other the higher the temperature gradients are and the higher the heat transfer coefficient. Figure 4.6, $\mathrm{Re}_H = 7766$, clearly demonstrates that the temperature contours above the first element diverse causing a drop in the temperature gradient and the heat transfer coefficient and consequently Nusselt number at this Reynolds number.

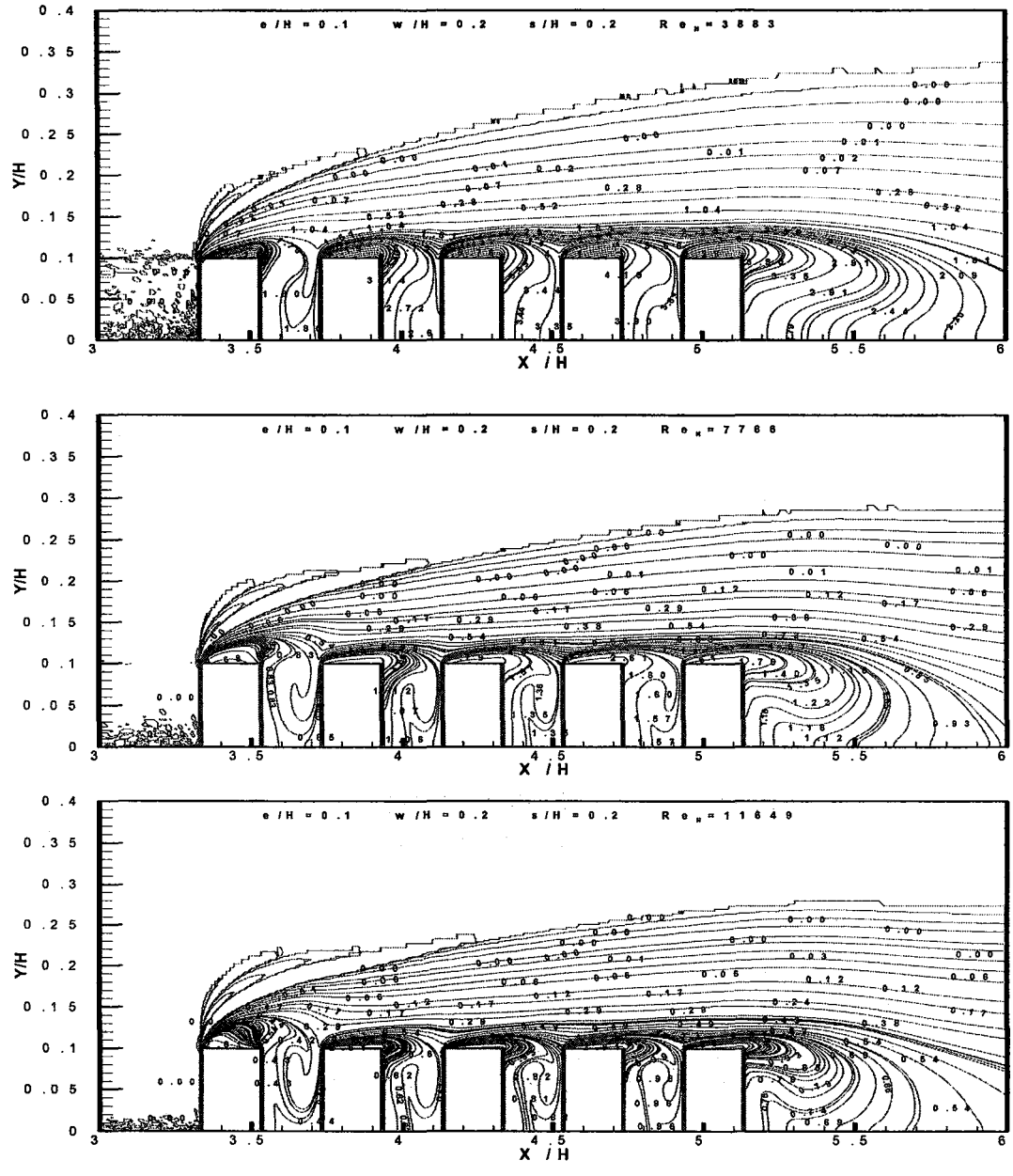

Figure 4.6 Dimensionless temperature contours at different inlet velocities

In general, increasing, Re_H, has a favorable effect on the rate of heat transfer. This increase has two main effects. First, it promotes better mixing in the channel by augmenting turbulence in the flow field; and second, the ability of flow to remove more heat in a shorter time due to the a higher temperature gradient and consequently the

higher heat transfer coefficient. These two effects combined resulting in a better heat transfer rate. Figure 4.7 shows the effect of Reynolds number on the mean Nusselt number of each element of the ribbed wall. It is shown that the average Nusselt number of each row increases with Reynolds number except for the first elements, where the average Nusselt number declines first, and then rises. Figure 4.2 helps us understanding this behavior, as it shows streamline contours through the channel at different Reynolds number.

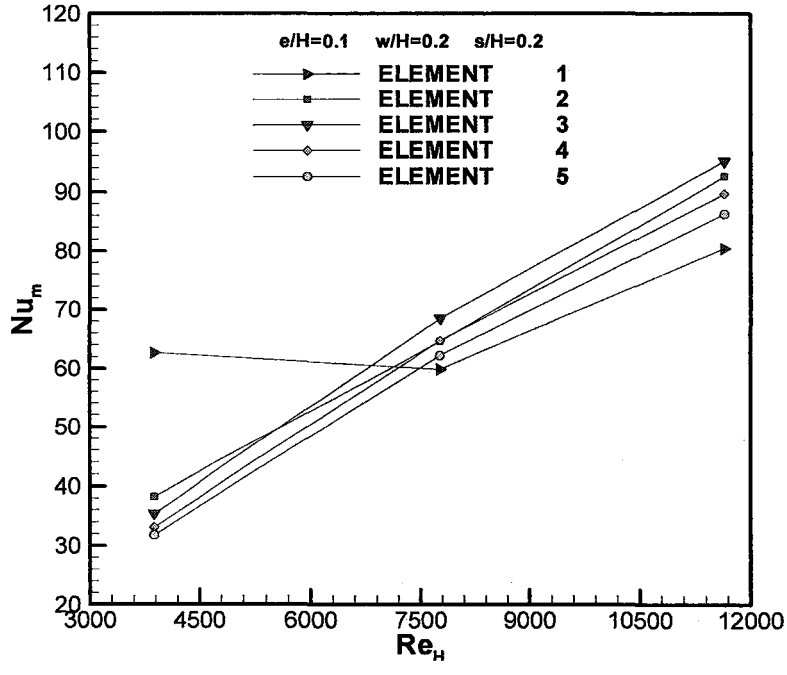

Figure 4.7 Average Nusselt number of a typical geometry over a range of different Reynolds number

4.3 Effect of Element Height

To study the effect of element height on the flow and heat transfer field, the parameters are maintained constant except the element height. Figure 4.8 shows the contours of streamlines for different e/H. It is shown as the element height increase the circulation zone behind the first element increases.

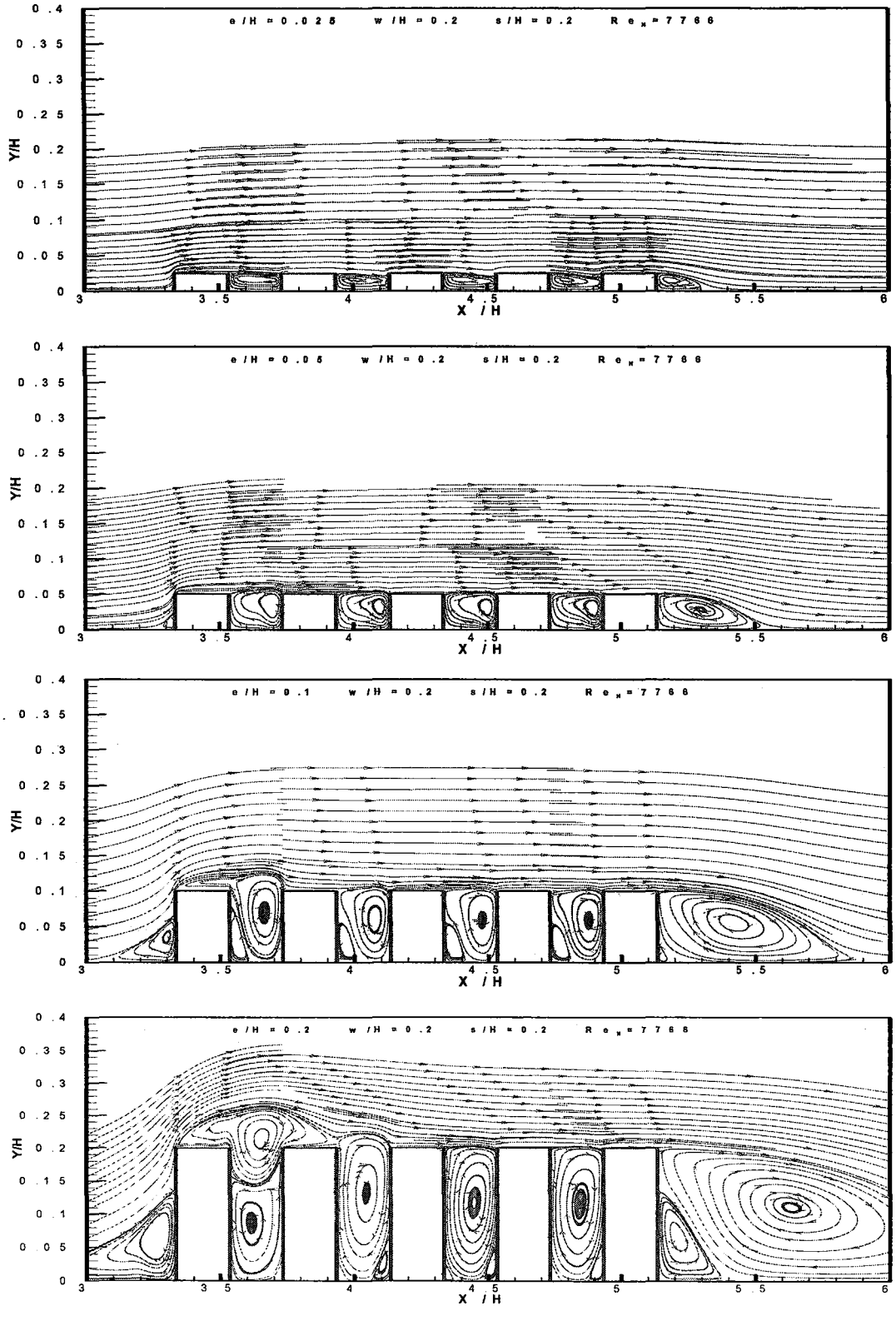

Figure 4.8 Streamlines of different element heights

At $e/H = 0.1$ the circulation zone behind the first element extends backwards in the reverse direction of the main stream. Obstructing the flow over the top surface of the first element and forming an obstacle where the main cold flow move around instead of getting closer to the hot surface to extract more heat.

This effect decreases the rate of heat transfer of the top surface of the first element and consequently Nusselt number. As the element height increases further this effect transfer to the next element and so on. The figure also shows that a small secondary vortex appeared at the lower left corner of the first step at $e/H = 0.1$. As the element height increases to 0.2 the channel height this vortex grows and becomes able to lift the primary vortex on top of it.

For a better understanding of the problem, we define *attack angle* as the chord line joining the upper trailing corner and the lower leading corner of the first element with the horizon, $\tan^{-1} {}^{e}/_{w}$. This angle is proportional to the way streamlines are formed on the leading upper-corner edge of the first element. By increasing the *attack angle,* the minimum pressure point moves forward on the top surface of the element and the minimum pressure becomes lower, generating stronger adverse pressure gradients in the direction of flow. Eventually, at some point, the *attack angle* results in pressure gradients strong enough to separate the boundary layer from the top element surface, and a circulation zone forms.

The pressure contours shown in figure 4.9 for different element heights suggest that as the element height increases, pressure gradients in the stream-wise direction as well as in the normal direction increase. In other words an adverse pressure gradient is able to grow. A closer look at these plots displays a very high negative pressure core that appears in the step between the two elements, the element step, as element height increases further beyond 0.1 *H*. This core is the center of the circulation zone between the two elements.

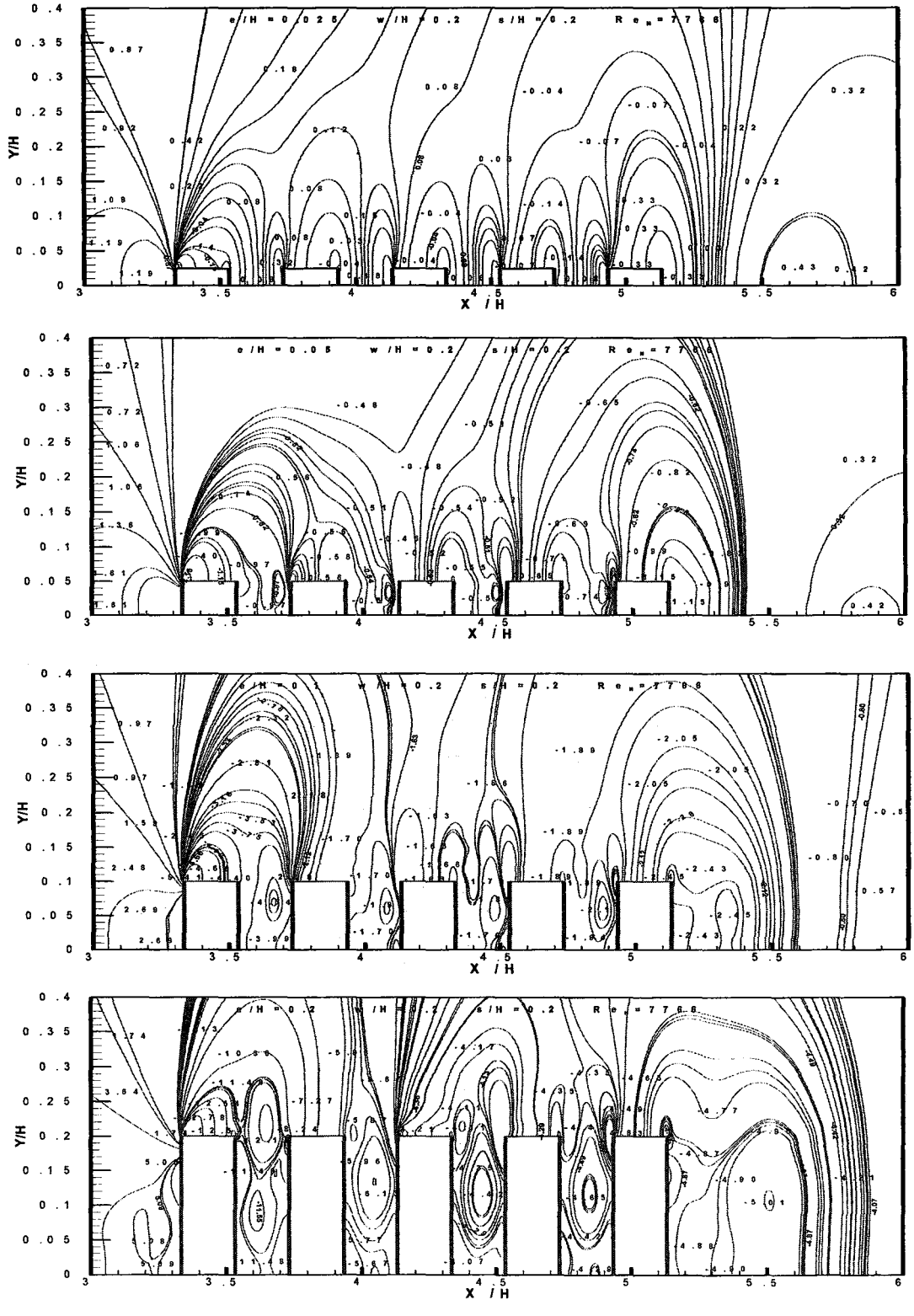

Figure 4.9 Relative pressure contours at different element heights [Pa]

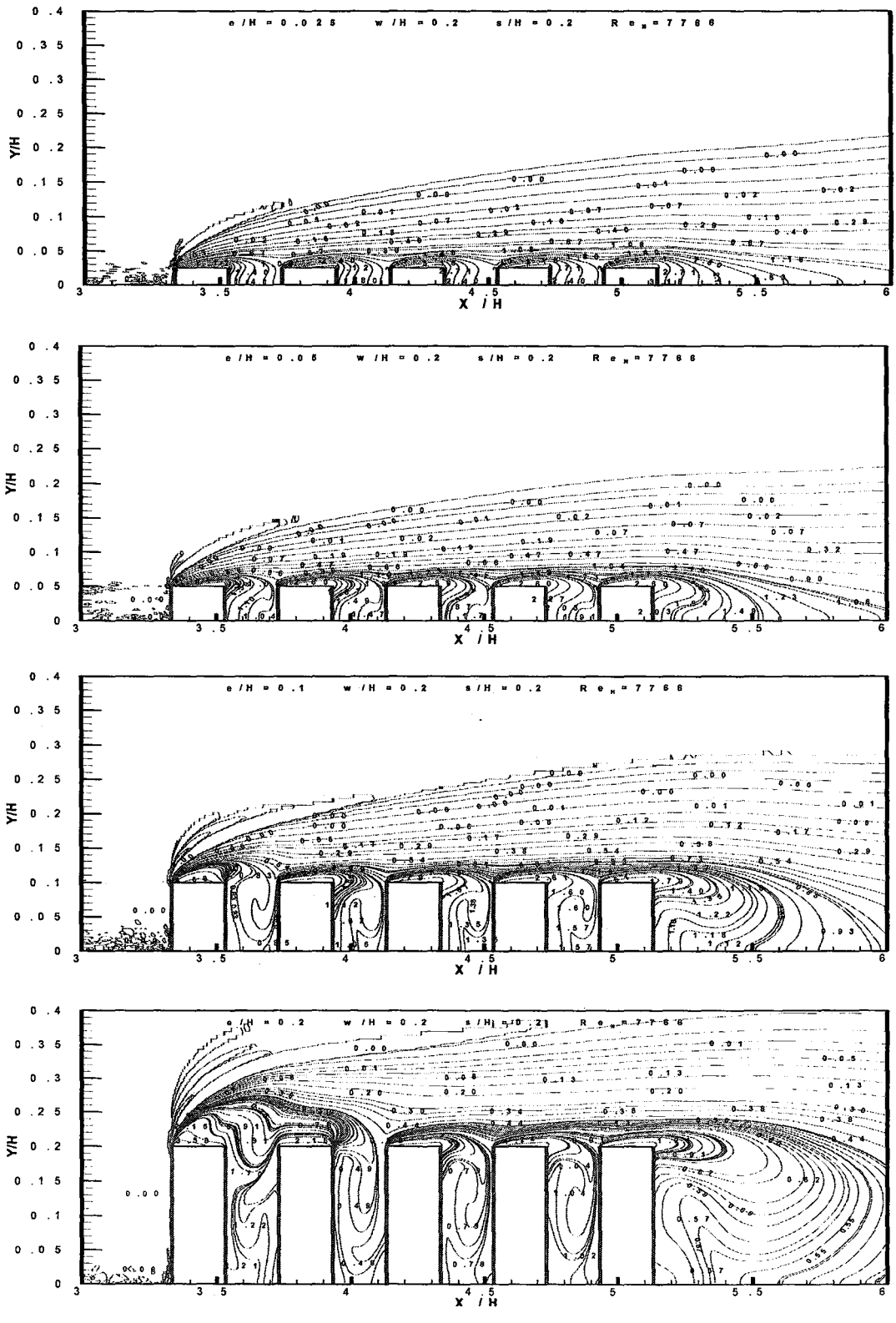

Figure 4.10 Dimensionless temperature contours at different element height

Figure 4.10 shows the dimensionless temperature contours at different element heights. It is shown that as the element height increases the temperature contours become more distorted in the gaps between two elements. This distortion is the consequence of the circulation zone between two elements, and it manifests itself as the flow swirls faster. The dimensionless temperature contours at $e/H = 0.1$, move away from the surface, decreasing the temperature gradient and consequently the rate of heat transfer and Nusselt number. As e/H increase the thickness of the region of less temperature contours increases and extends to cover the second element at $e/H = 0.2$. This region may be thought as an insulation zone that prevents the cold flow from getting in touch with the element surface and decreases the rate of heat transfer.

In particular increasing, element height has an escalating effect on the rate of heat transfer, with the exception of the first and second rows.

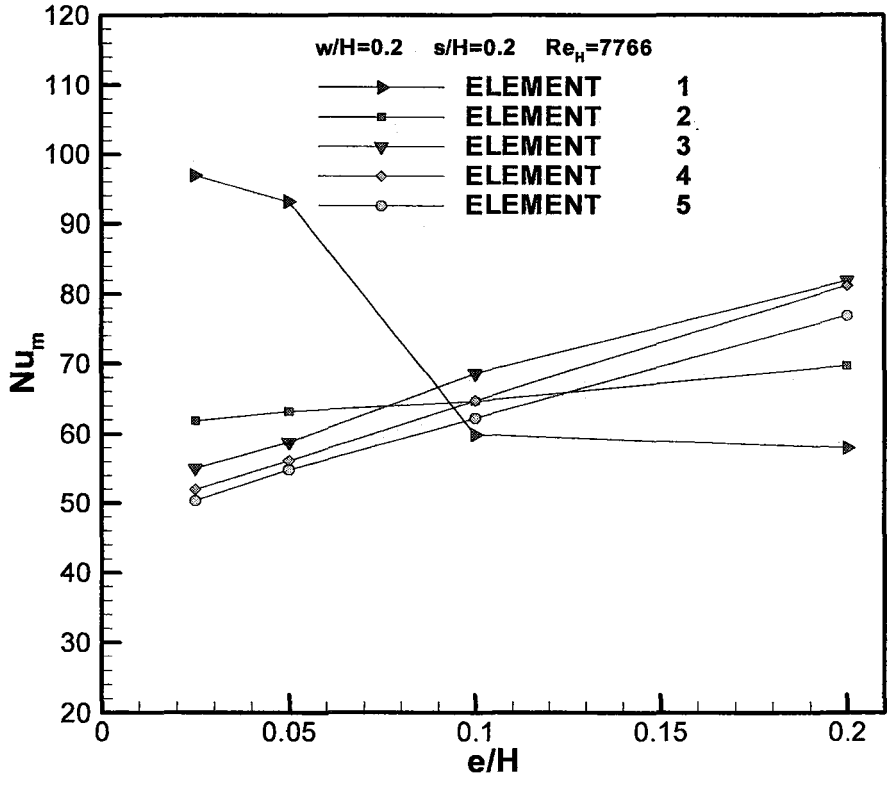

Figure 4.11 Average Nusselt number of a typical geometry for different element heights

The step-up of heat transfer rate is due to a smaller clearance area, C, that forces the flow to accelerate. With higher velocity, the rate of heat transfer and turbulent mixing of the flow field improve. Figure 4.11 depicts the increase of element height in relation to average Nusselt number of each element.

Another look at figure 4.11 justifies that by providing a prone condition to circulation, $e/H = 0.05$, the average Nusselt number on the first element slightly decreases and, when circulation forms, $e/H = 0.1$, heat gets trapped and the average Nusselt number drops rapidly. The circulation zone, when established, $e/H = 0.1$, affects the second row of elements by deflecting the flow above it and lowering the average Nusselt number. Finally, the circulation zone covers the first and second elements entirely, and even lowers further the heat transfer rate.

4.4 Effect of Element Width

To study the effect of element width on the flow and heat transfer field, the other parameters are kept constant at $e/H = 0.1$, $s/H = 0.2$, and $\mathrm{Re}_H = 7766$.

Streamlines contours are shown in figure 4.12 as a function of the element width. It is shown that as element width increases shear layer on top surface of the elements becomes larger and hence boundary layer. Ultimately element width increase breaks the top surface circulation zone and flow tends to stratify.

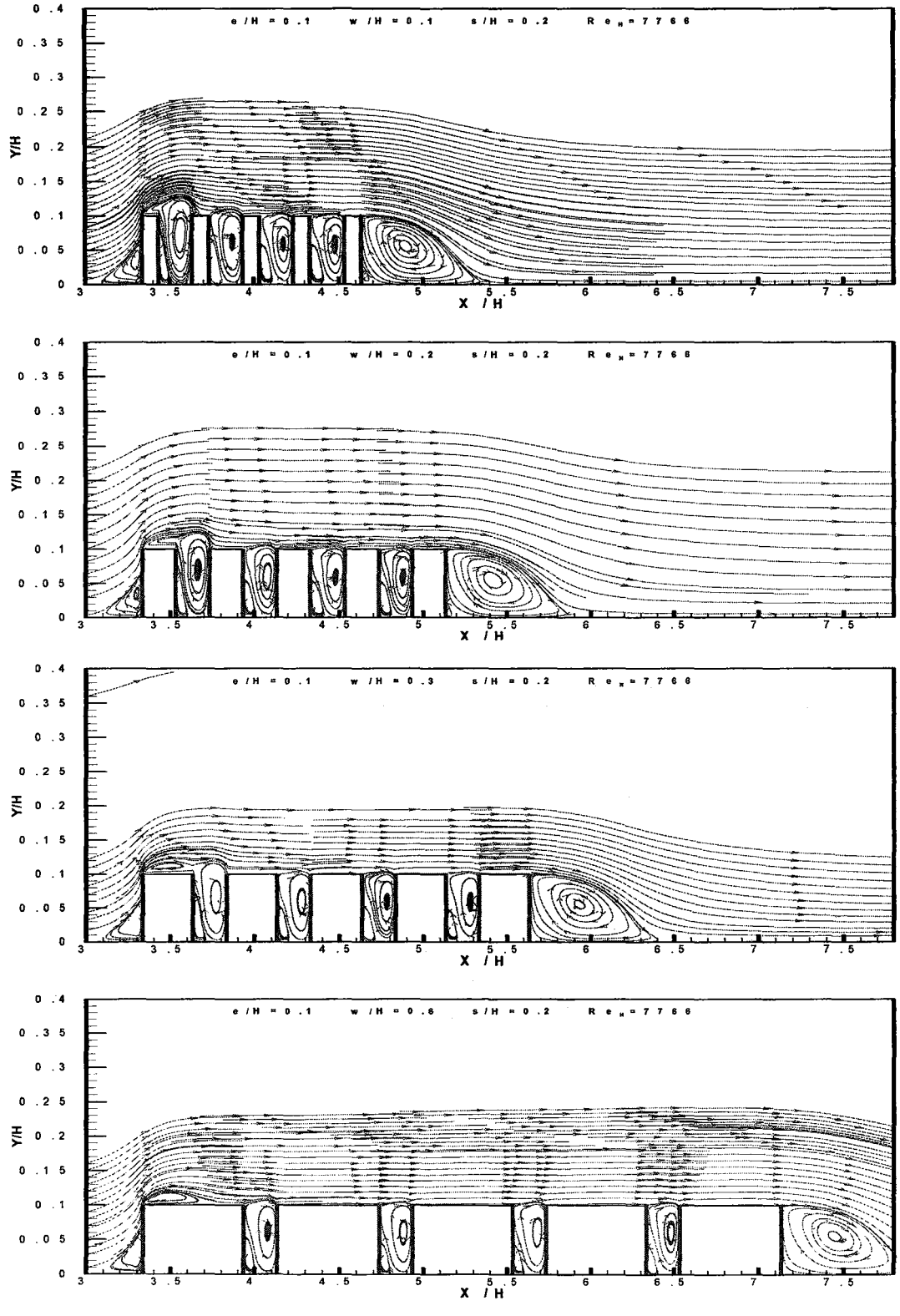

Figure 4.12 Contours of streamlines at different element widths

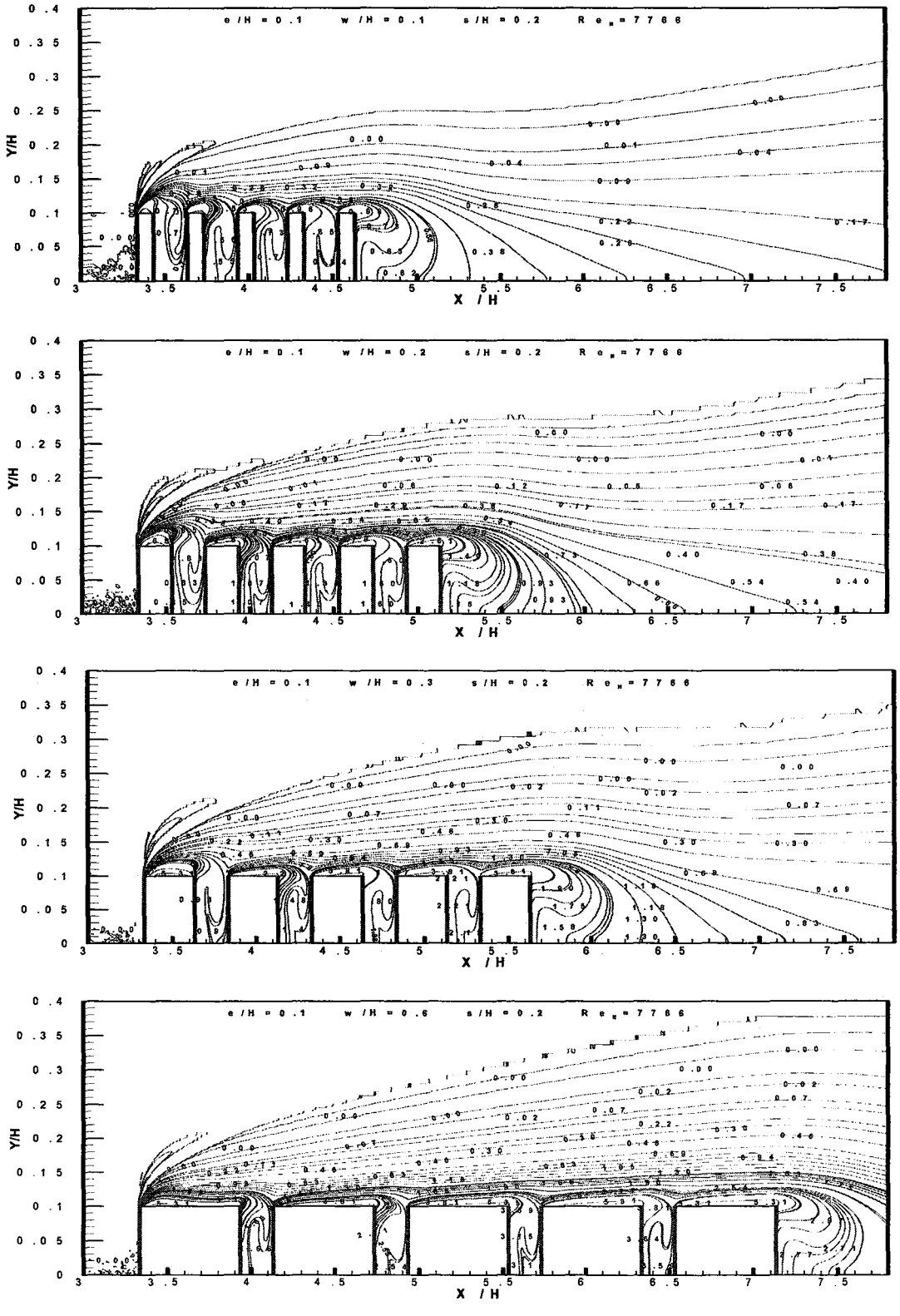

Figure 4.13 Dimensionless temperature contours at different element widths

Figures 4.13, shows that as the element width increases the dimensionless temperature contours at different element widths, with respect to the step width, the flow tends to behave as flow over a flat plate where the thermal boundary layer at the top of each element tends to merge together. This tendency is exhibited by figure 4.13, $w/H = 0.6$.

The effect of the element width on Nusselt number is shown in figure 4.14 for a typical study case. It is shown that the average Nusselt number decreases with the element width without exception for any of the elements.

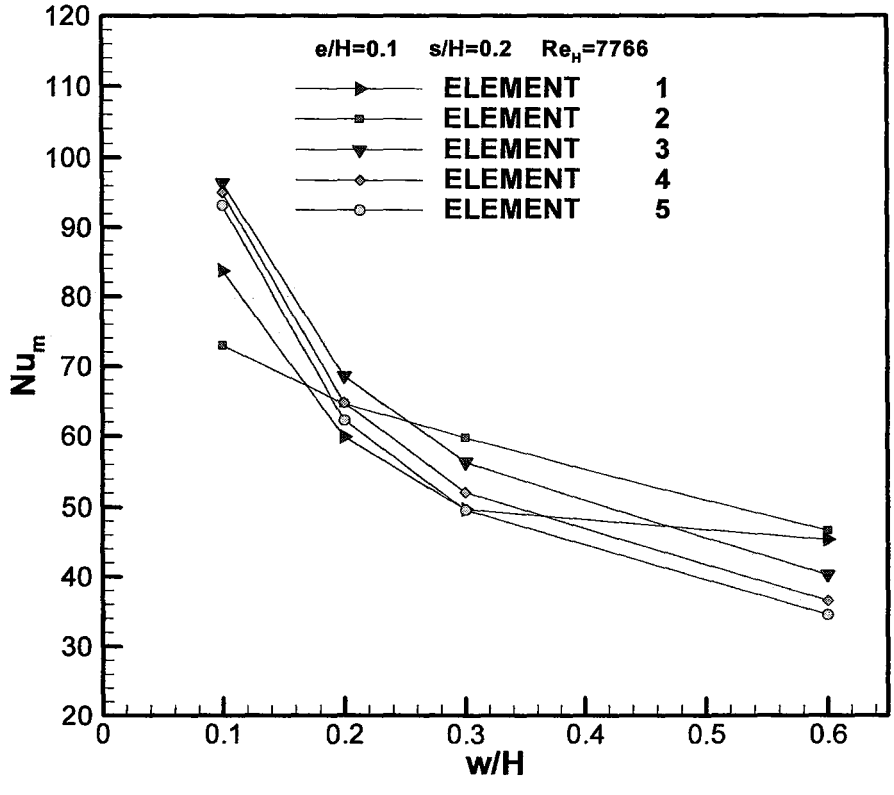

Figure 4.14 Average Nusselt number of a typical geometry over a range of different element widths

By increasing the element width, boundary layer gets enough length to grow and becomes thicker. As a result, the wall shear stress increases on the upper surface of the elements and better resists the adverse pressure gradient, and the circulation zone that traps heat occupies a smaller portion of the element upper surface. This effect improves the heat transfer coefficient on the first and second elements. On the other side the thermal boundary layer thickness increases and the thermal resistance becomes greater for each element which decreases the average Nusselt number.

4.5 Effect of Element Step Width

To study the effect of element step width on the flow and heat transfer field, the parameters are maintained constant except the element step size. Figure 4.15 shows the effect of the element step width on the streamlines in the ribbed channel. As the step size increases, the circulation zone behind each element expands in the flow direction decreasing its height, so the bump that prevents the cold streamlines from touching the following element becomes inflated. This increases the temperature gradient over the surface of the element. In other words, the mainstream flow finds itself closer to the heat sources, and the thermal resistance between them decreases. This improves the removal of heat by the main stream, and the heat transfer increases.

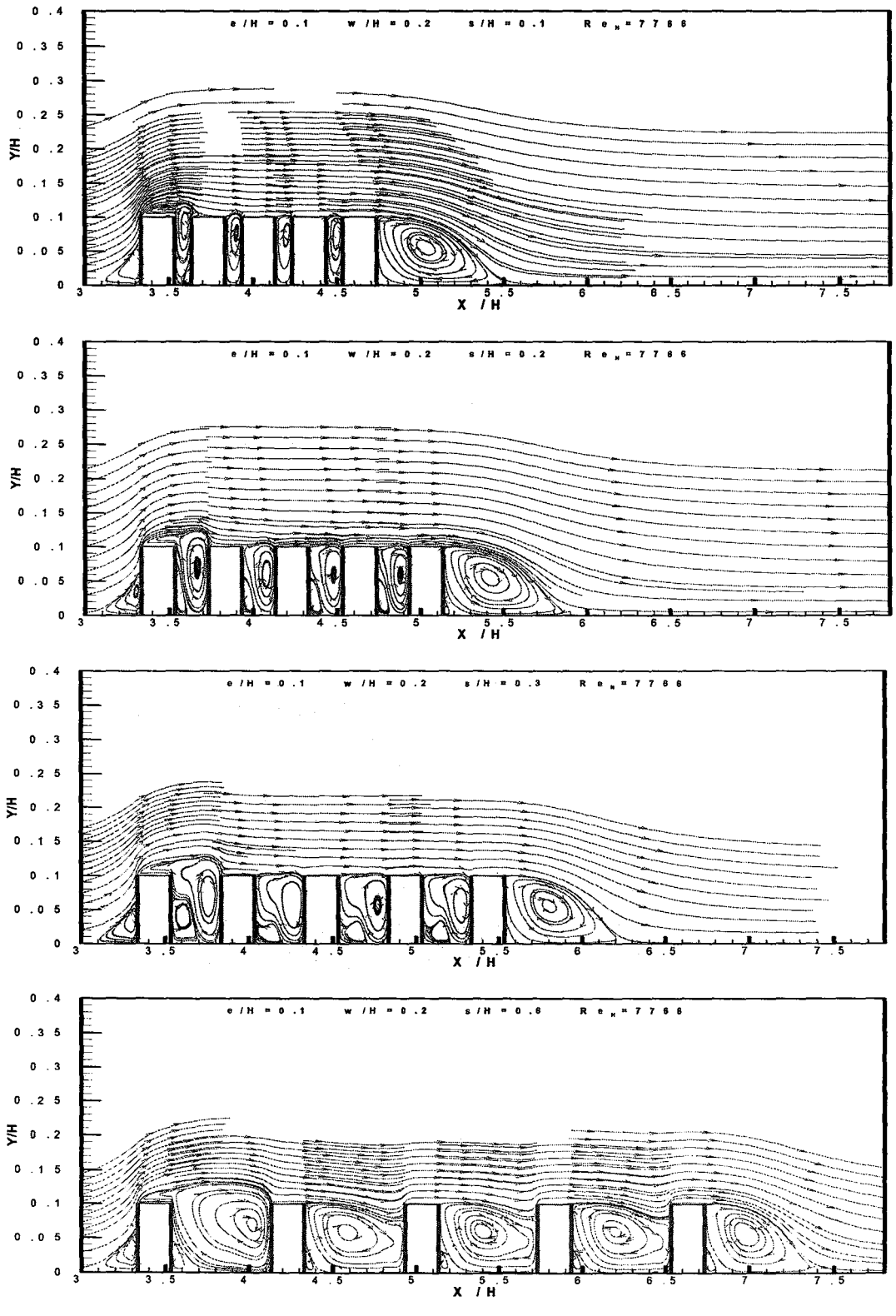

Figure 4.15 Streamlines at different element step widths

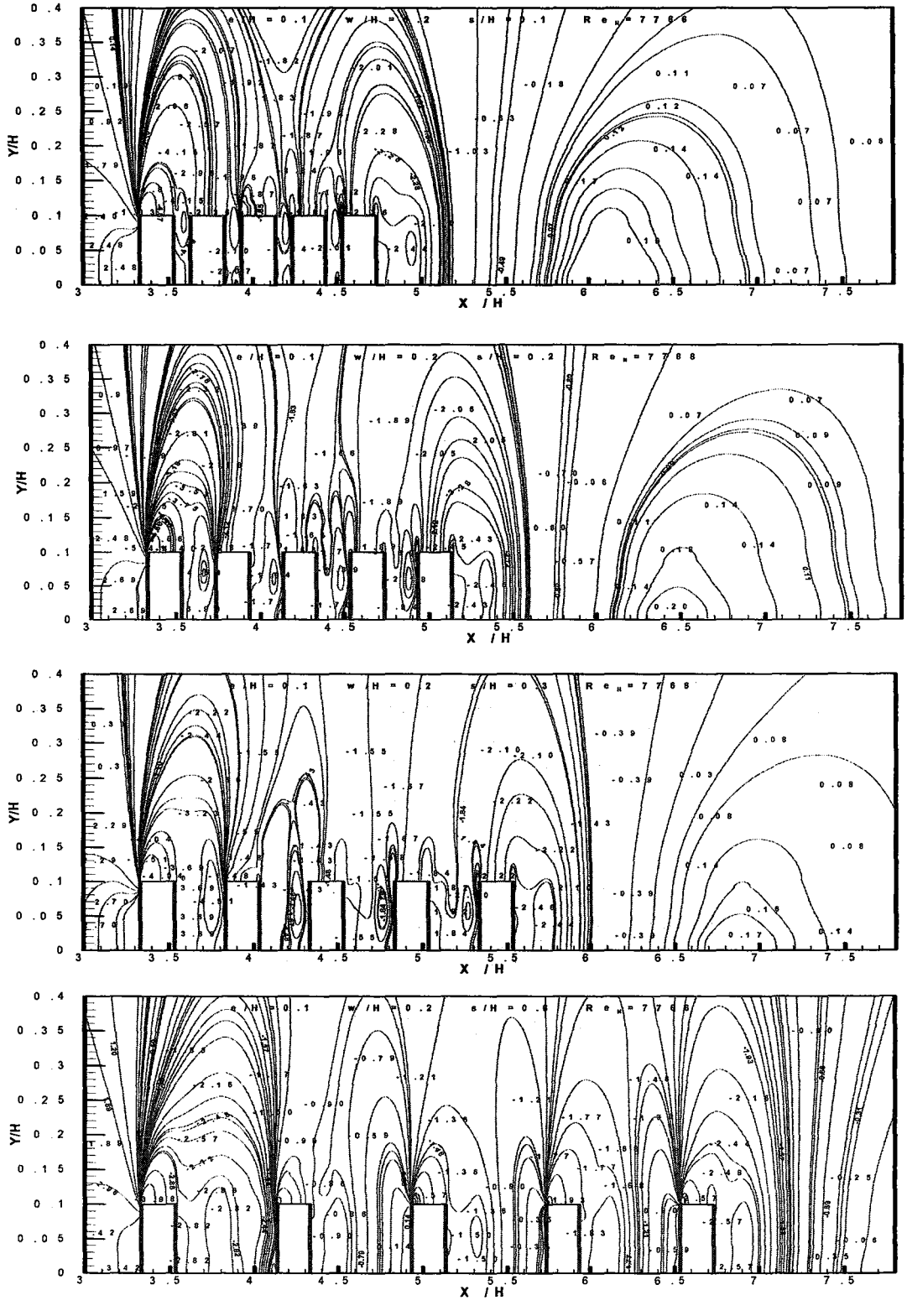

Figure 4.16 Relative pressure contours at different step widths [Pa]

Contours of relative pressure are shown in figure 4.16. By increasing the step-size the pressure in the gap between two elements increases. This increase come as a result of the mainstream higher-pressure air that introduces itself into the space between two elements as gaps enlarge. This trend can be clearly seen at $s/H = 0.6$ where pressure becomes higher on the downstream wall of the step where the outer step flow sees the wall and detours.

Dimensionless temperature contours at different step widths are shown in figure 4.17. As mentioned earlier, the closer these contours are the higher the temperature gradient, which manifest borders of the main heat transfers.

When interruptions of the thermal boundary layer are large enough, a flat plate-like behavior of heat transfer, $s/H = 0.1$, changes, and thermal boundary layer between elements breaks. With further increase of step width, $s/H = 0.6$, the higher temperature contours fall in the step behind the element thermal boundary and another starts to grow on the next element and so on. Since the leading portion of the thermal boundary layer has the higher temperature gradient and higher heat transfer rate so the effect of increasing the step width is to increase the heat transfer coefficient and consequently Nusselt number as shown in figure 4.18.

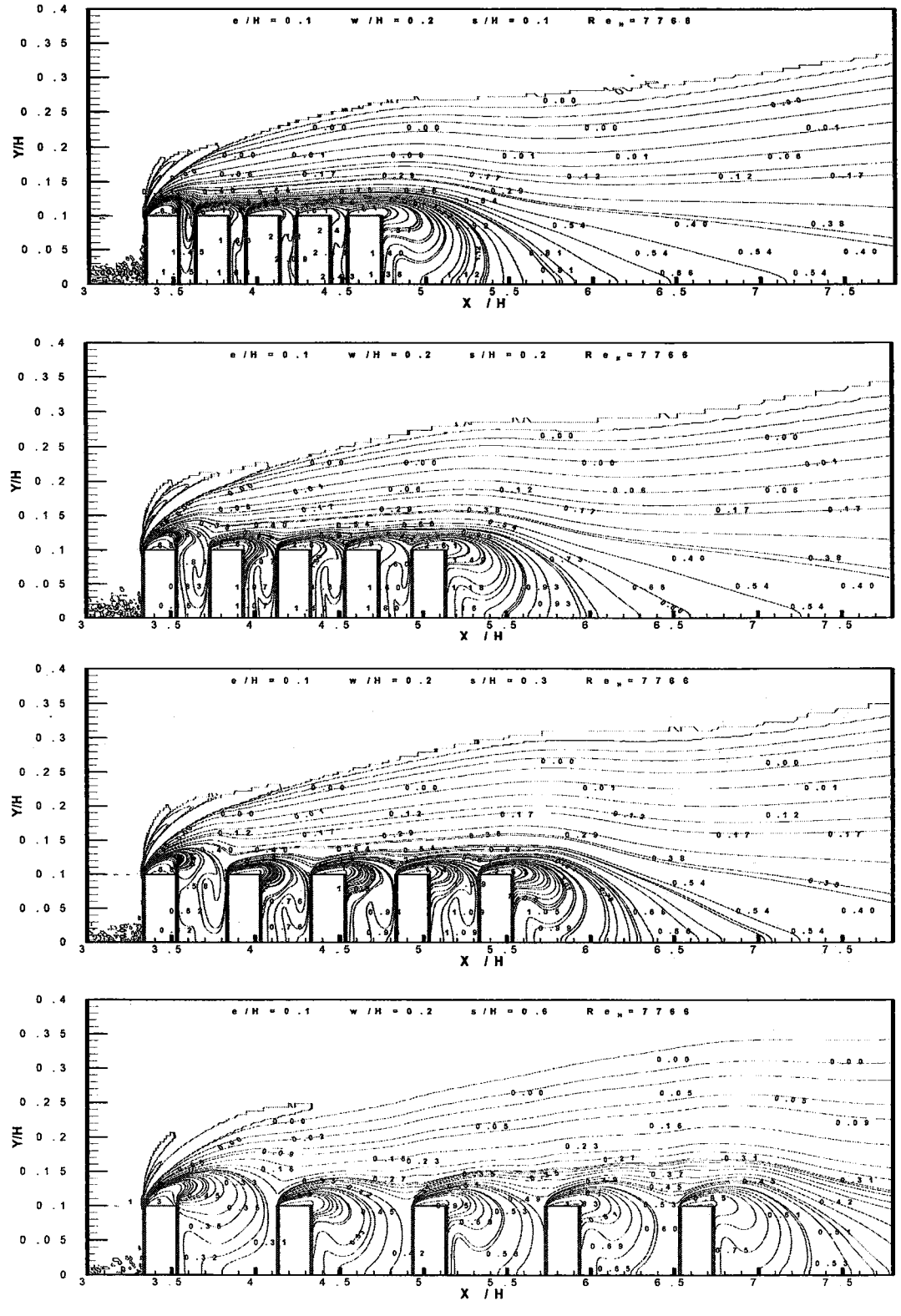

Figure 4.17 Dimensionless temperature contours at different element step widths

Figure 4.18 shows the average Nusselt number of five obstacles with change of step width. All elements show an increase in the average Nusselt number with step size increase. It might be assumed that step width size should not affect the heat transfer rate of the first element, but this is even true for the first row of elements, which show a slight increase in the heat transfer rate. As the step width increases, the circulation region that traps heat between the two elements finds a greater length on its upper side to exchange heat with mainstream flow. In other words, the flow has more time to exchange heat. In addition, as gaps enlarge, mainstream air has more opportunity to be introduced into the distance between the two elements. This opportunity brings fresh outside air into the steps and helps cool the circulating air between the two elements. A slight increase of the first element's average Nusselt number is due to this fact.

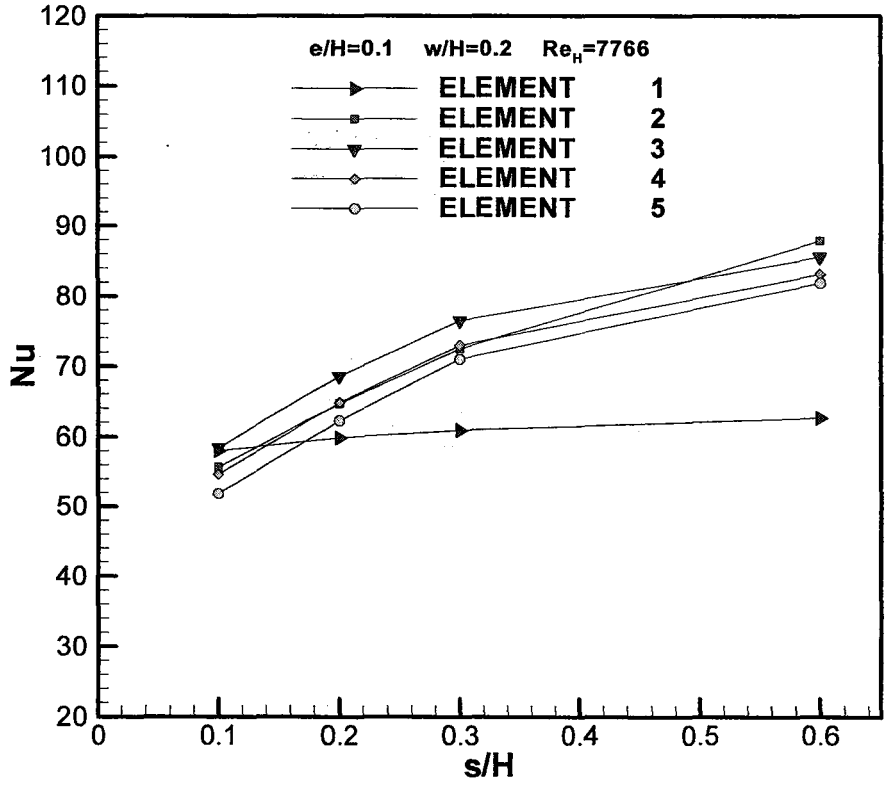

Figure 4.18 Average Nusselt number of a typical geometry at different element step widths

In figure 4.18, the average Nusselt number rank of the second element among the five heaters has improved. This improvement can be understood by looking at streamlines of flow when the step size is increased.

4.6 Combined Effect of Parameters

4.6.1 Effect of Reynolds Number and Element Height

As shown in the previous sections the rate of heat transfer from the ribbed wall increases with increase of mean inlet velocity and element height, with some exceptions. These exceptions are applied to the few leading elements. The reason for this behaviour is referred to the flow that produces a circulation zone above these elements. This circulation zone conserves heat causing the average Nusselt number to drop drastically. After the circulation region becomes fully developed, the heat transfer rate drop dampens. Figure 4.19 shows the effect of both Reynolds number and element height on the average Nusselt number. For instance, on the first element at $\mathrm{Re}_H = 3883$ the average Nusselt number first increases due to element height increase, then slightly drops due to the formation of the circulation zone. This drop continues due to the growth of the circulation zone. This trend is, to some extent, different for $\mathrm{Re}_H = 11649$, where the circulation zone forms at lower element height, $e/H = 0.05$, and its effect increases as the element height increases. Streamlines shown in figure 4.20 confirm this behaviour.

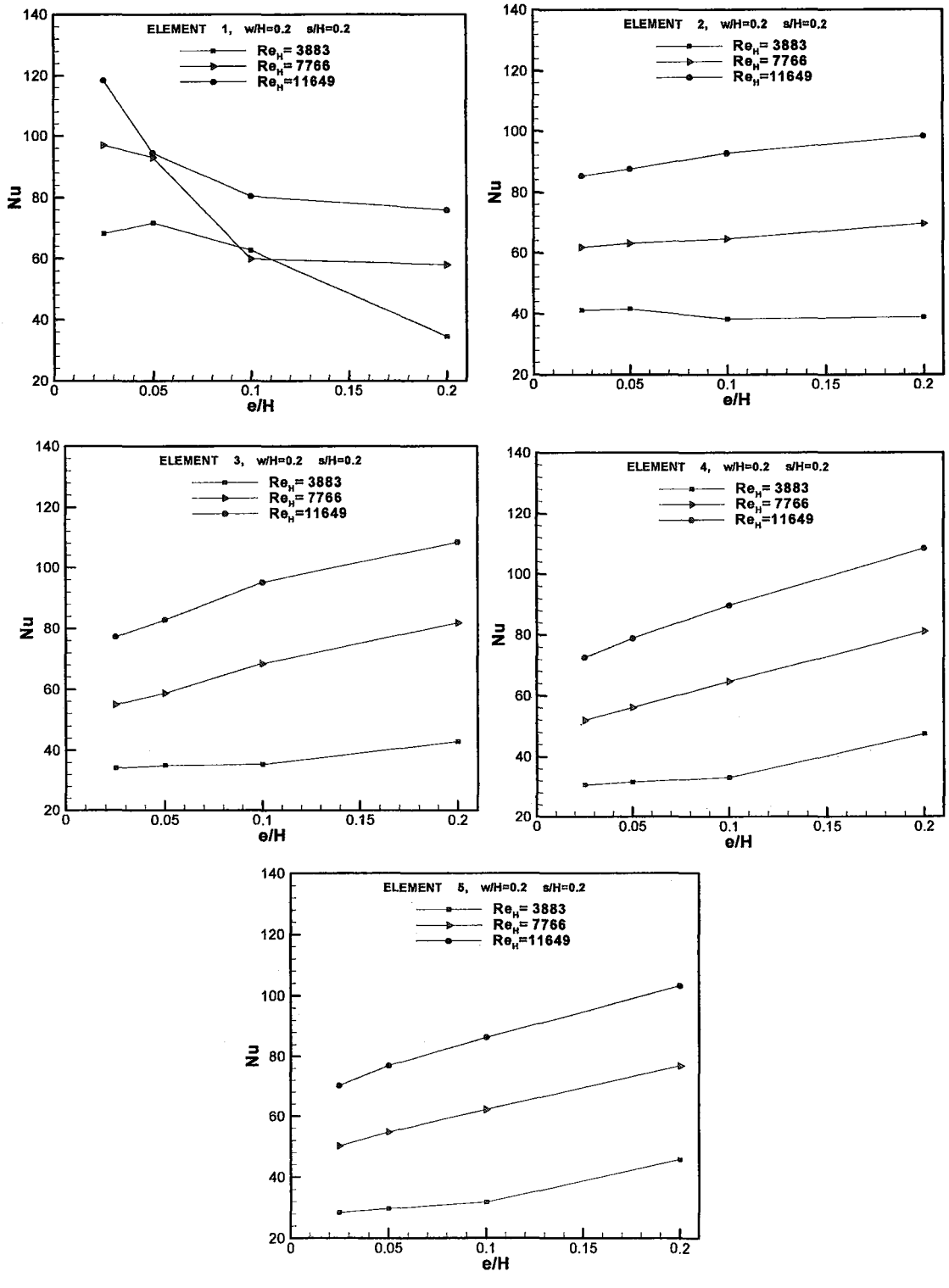

Figure 4.19 The combined effect of Reynolds number and the element height on the average Nusselt number

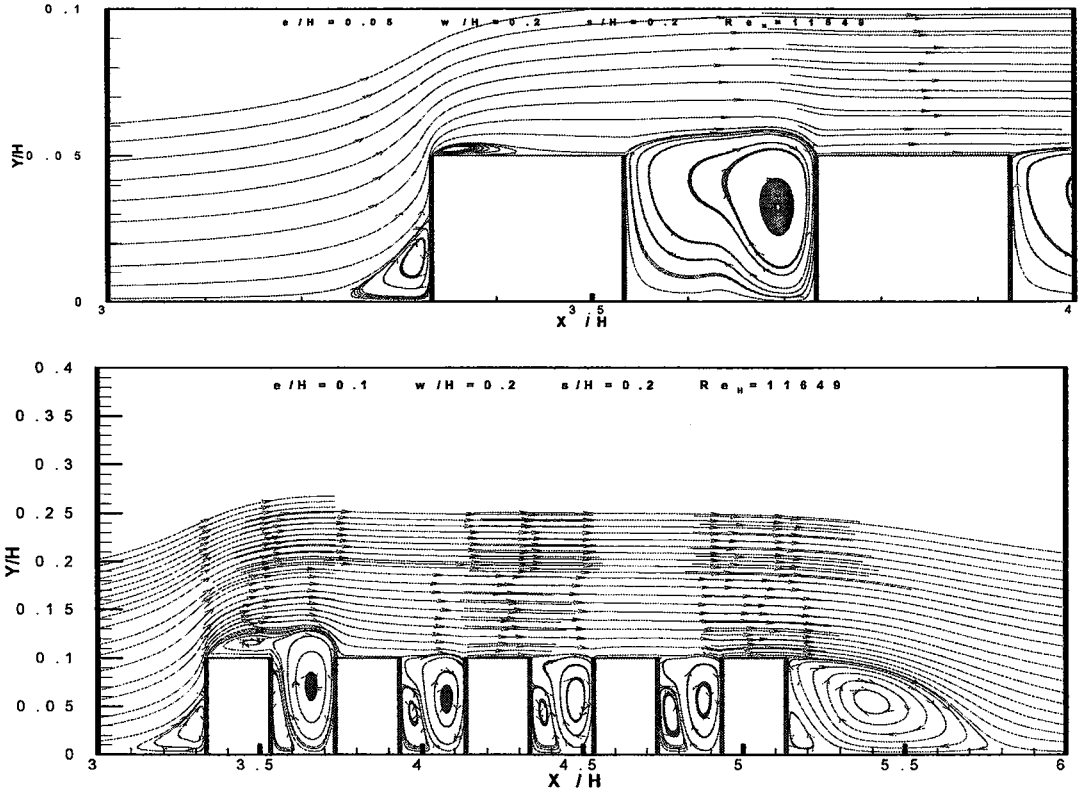

Figure 4.20 The development of the circulation zone on the top surface of the first element at $\mathrm{Re}_H = 11649$ and different element height

Figure 4.21 represents the data of figure 4.19 in a different way. As shown earlier, as the element height increases the heat transfer rate increases. This figure shows that average Nusselt number, Nu_m, decreases with increasing e/H. This might be true for the first element but not for the following ones.

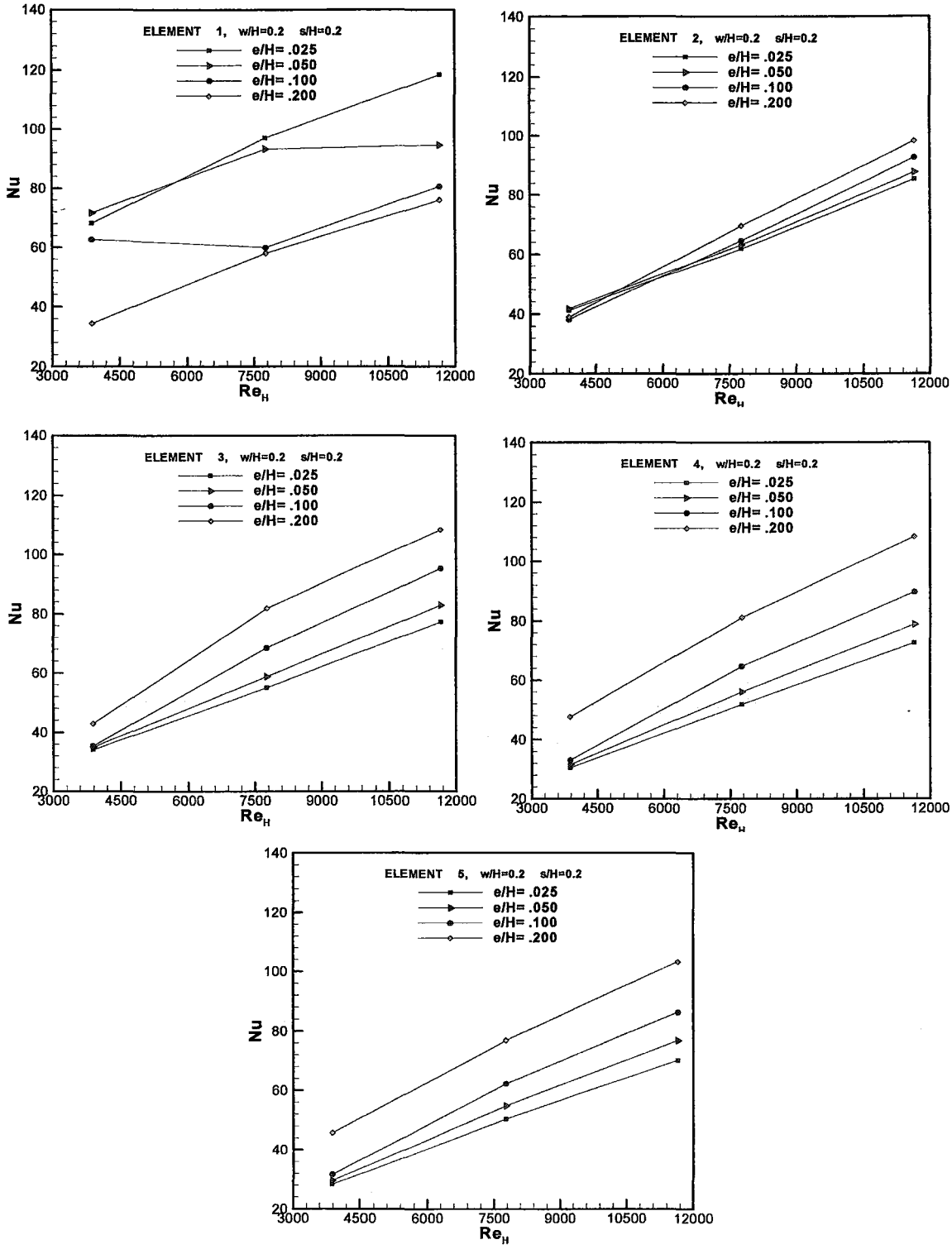

Figure 4.21 Average Nusselt number at different flow rates

4.6.2 Effect of Element Height and Element Width

Figures 4.22 shows the average Nusselt number at different element heights and element widths for each element.

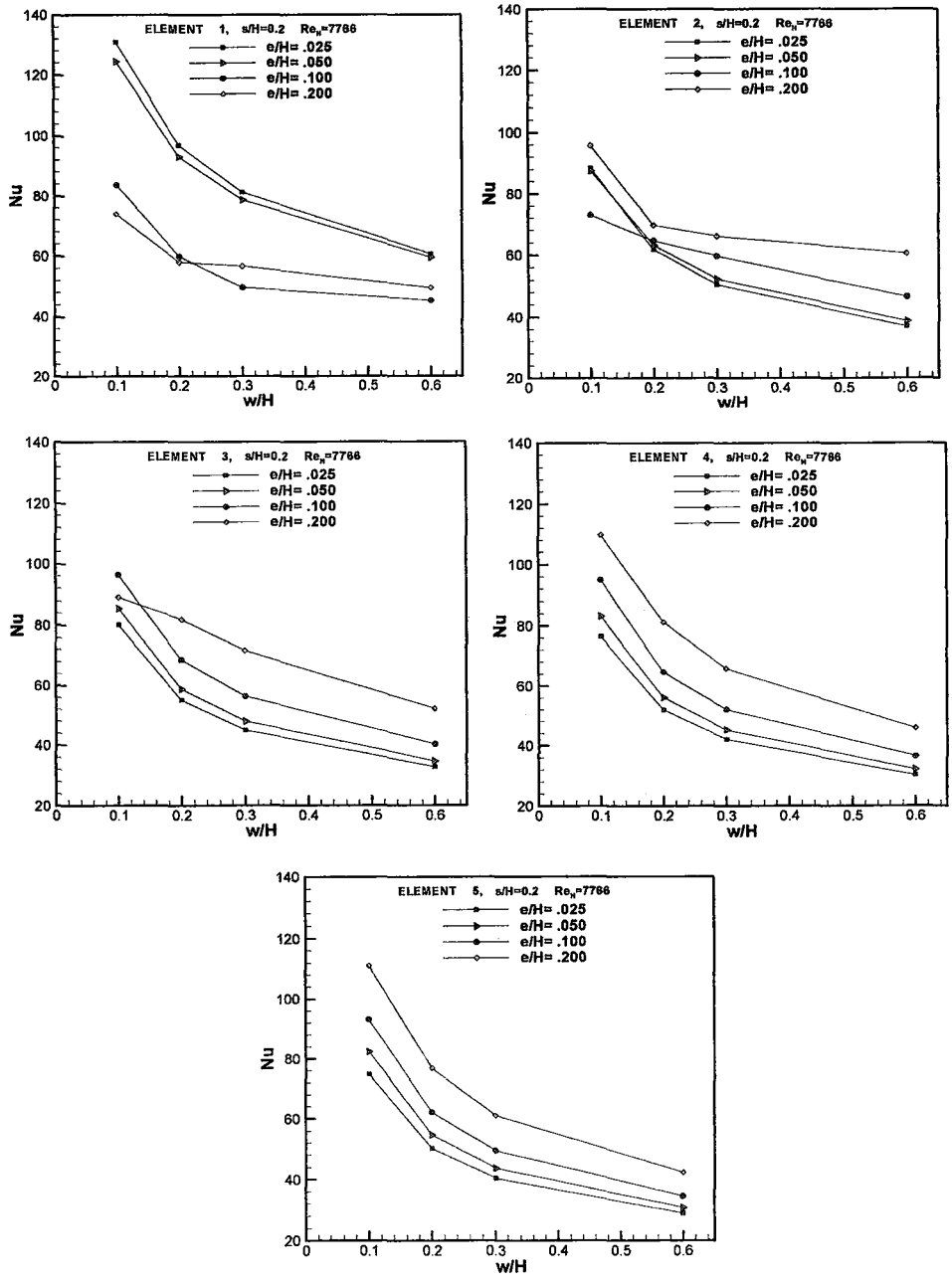

Figure 4.22 The effect of both the element width and height on the average Nusselt number

As shown, the average Nusselt number does not follow the general rule because of the circulation zone above the first and second elements. In figure 4.22, on the first element the rank of the highest average Nusselt number belongs to the lowest element height, $w/H = 0.1$. This is because, with higher element height, the circulation zone is bigger. Later, a shift in this rank happens from $w/H = 0.2$ to $w/H = 0.3$.

Also, Figure 4.22 illustrates the second effect of the circulation zone. In this figure, on the second element $e/H = 0.1$, the heat transfer rate has improved in rank with increase of element width. This order rearrangement is due to the detour of flow by the circulation zone above the first element that has subsided when the element width has increased.

Figures 4.23 and 4.24 show streamlines of this rank displacement for $e/H = 0.2$ and, respectively. As shown in figure 4.23, $w/H = 0.1$, two circulations zones exist above the first and second element, as there is only one in its counterpart figure 4.24, $w/H = 0.1$. These two circulation regions are more capable of trapping heat. But as the element width grows, a turbulent boundary layer better resists the adverse pressure gradient, and the two-circulation zones collapse into one. This is where the average Nusselt number lines of $e/H = 0.2$ and $e/H = 0.1$ switch rank.

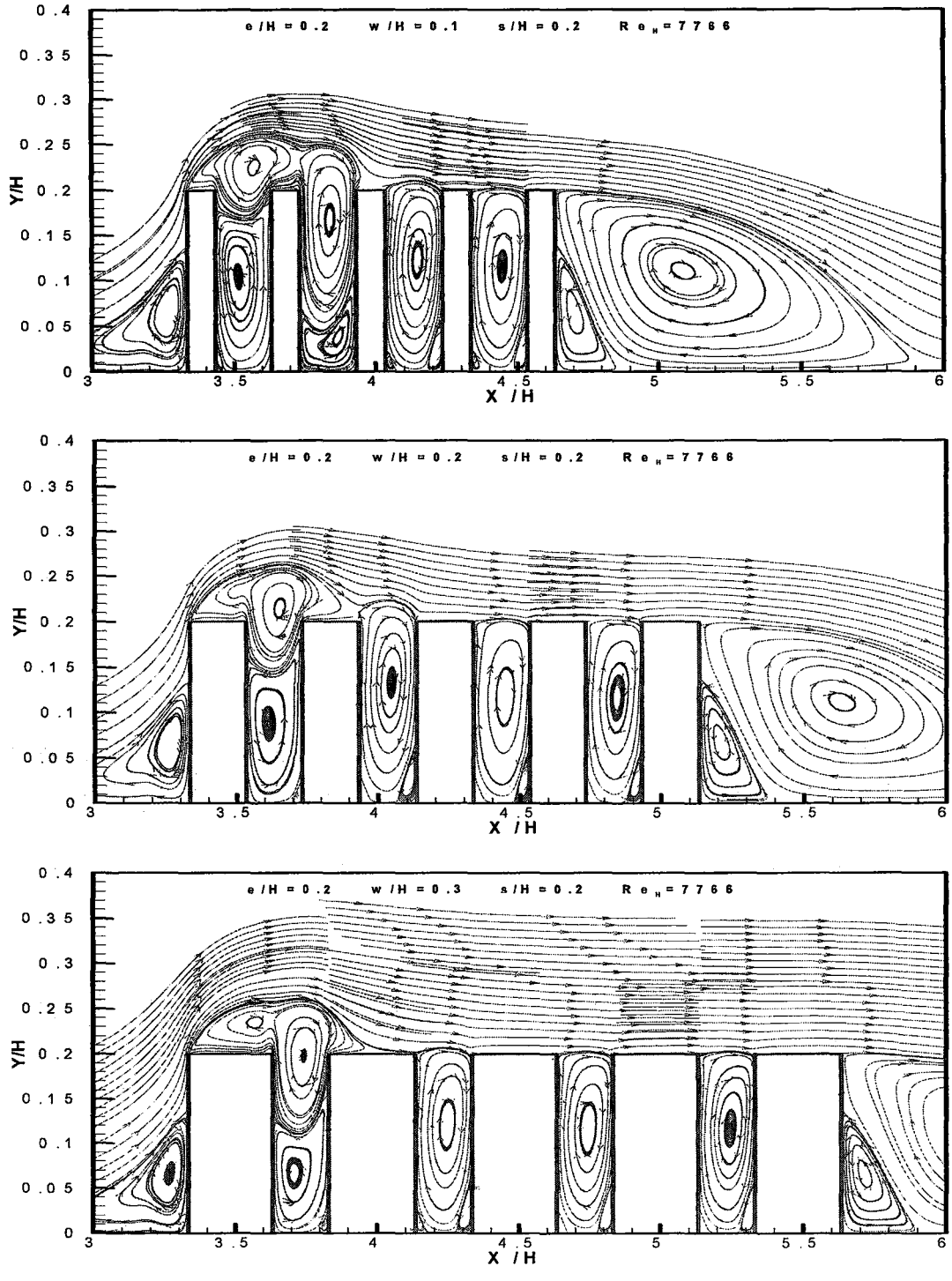

Figure 4.23 Streamlines at different element width, $e/H = 0.2$

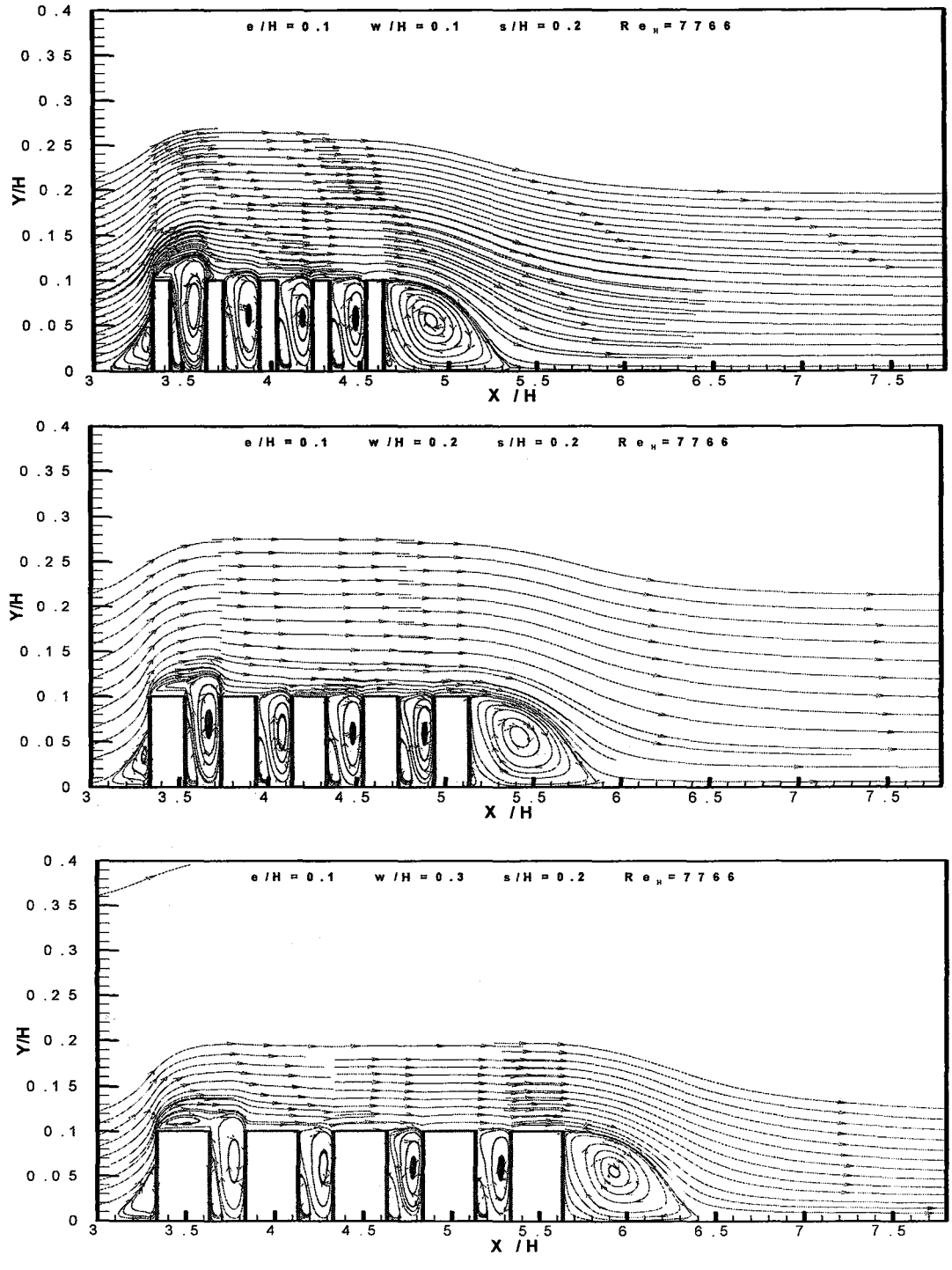

Figure 4.24 Streamlines of different element widths, $e/H = 0.1$

4.6.3 Effect of Element Height and Element Step width

Figures 4.25 and 4.26 show the effect of element step width and height with respect to each other. As shown, an increase of step width has a favourable effect on heat transfer. This increase is clearer with higher element heights.

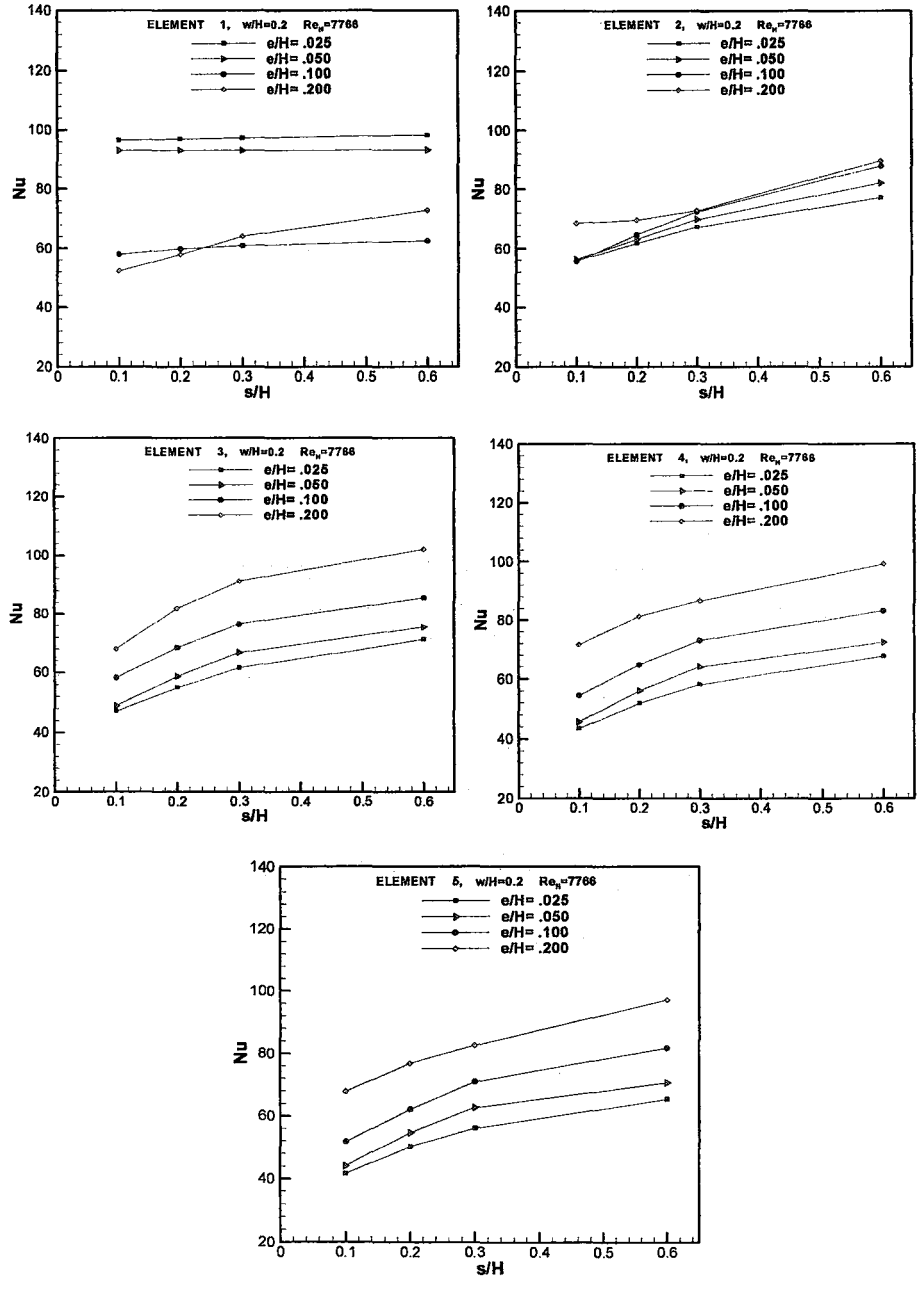

Figure 4.25 Average Nusselt number at different element step widths

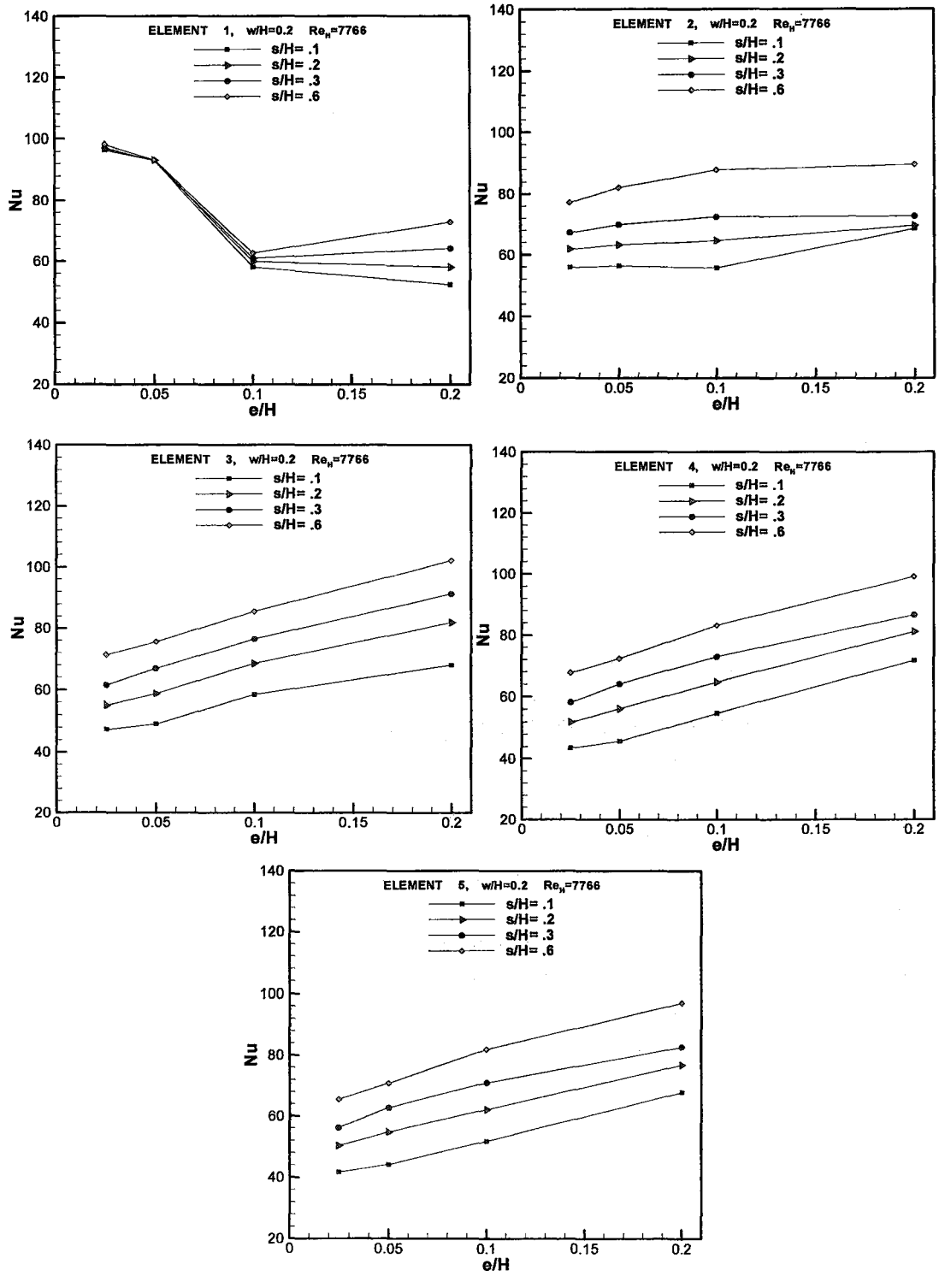

Figure 4.26 Average Nusselt number at different element heights

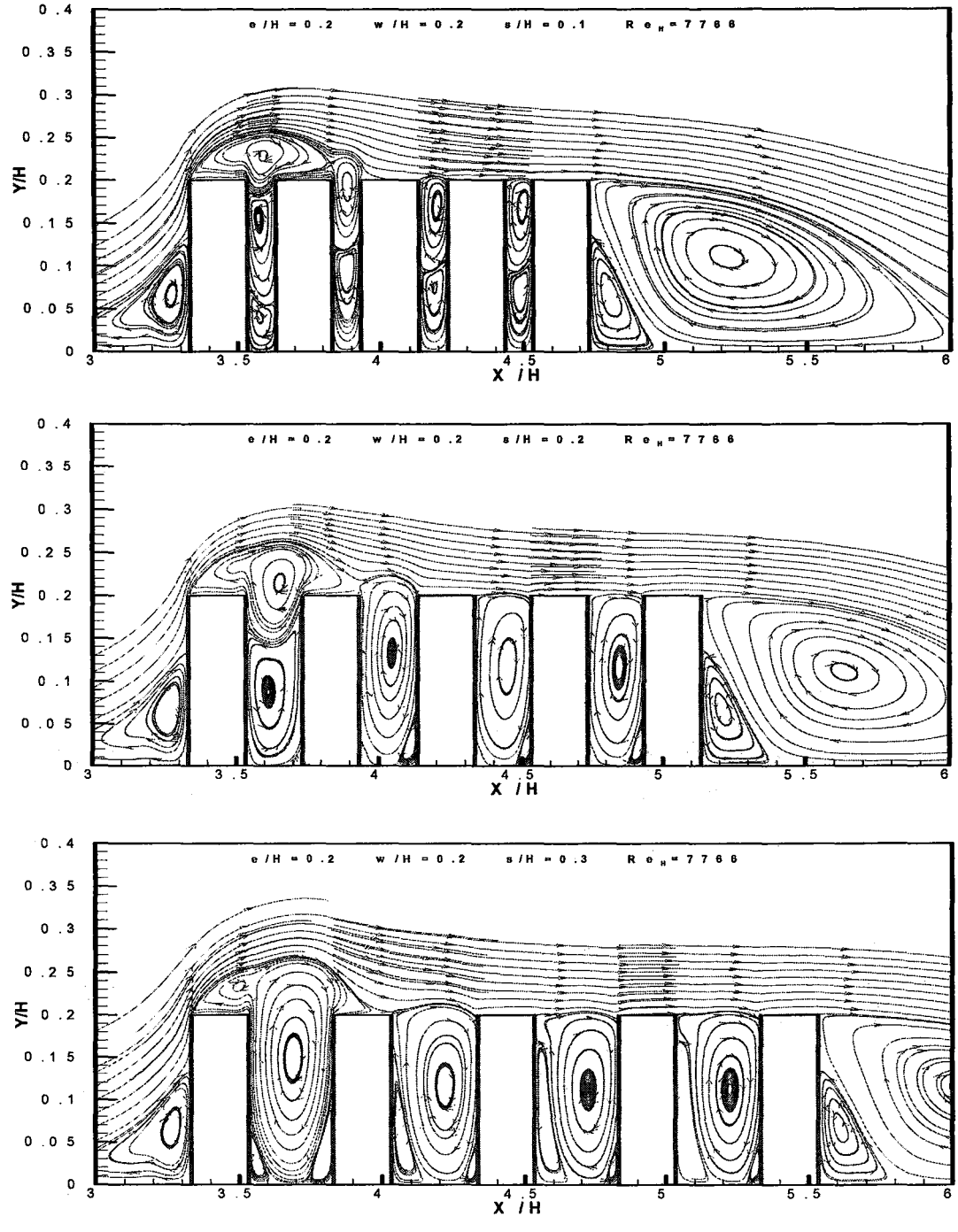

Figure 4.27 Streamlines of different element steps

4.6.4 Effect of Reynolds Number and Element Width

Figures 4.28 and 4.29 show that an increase of flow rate and a decrease of element width have an increasing effect on the average Nusselt number. In figure 4.28, a switch of rank on the first element in the average Nusselt number reminds us that at $\mathrm{Re}_H = 7766$ from $w/H = 0.3$ to $w/H = 0.6$ the circulation zone above the first element is controlled. Also, with higher velocity, the average Nusselt number increases.

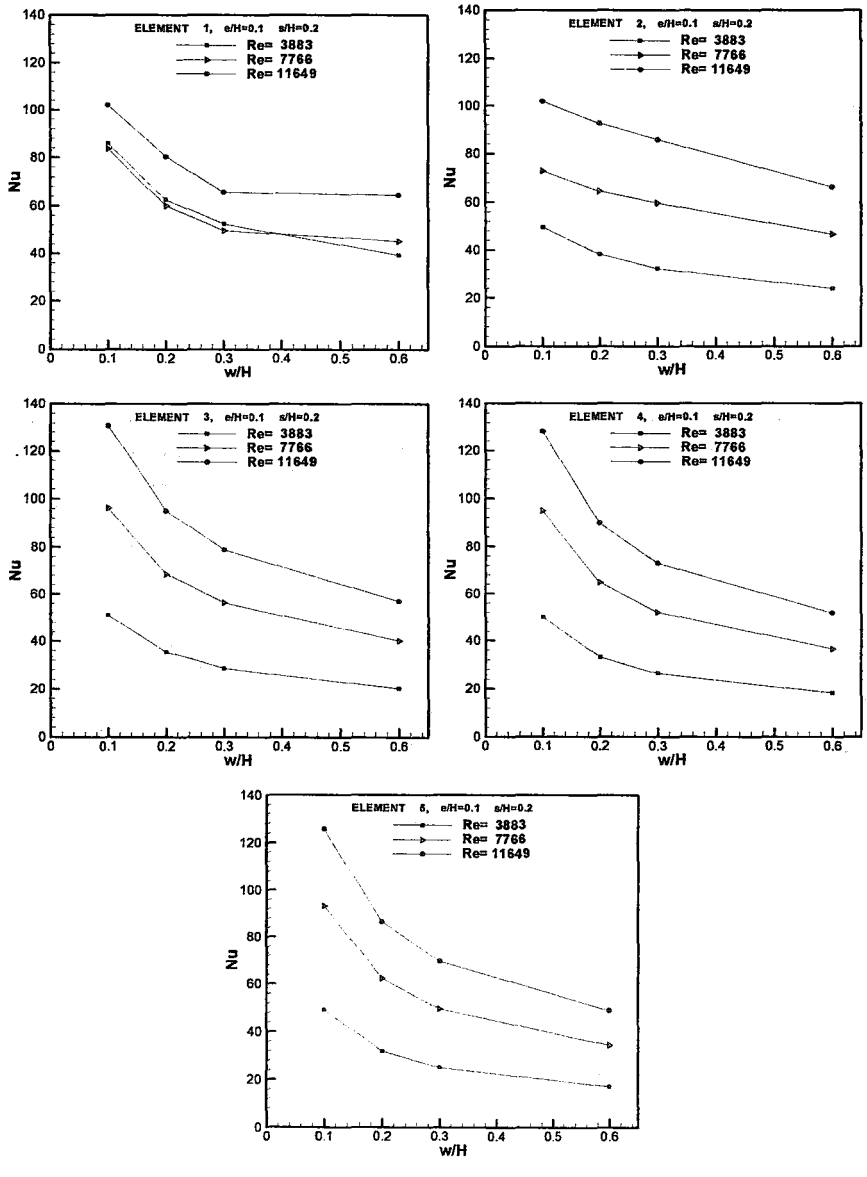

Figure 4.28 Average Nusselt number at different element widths

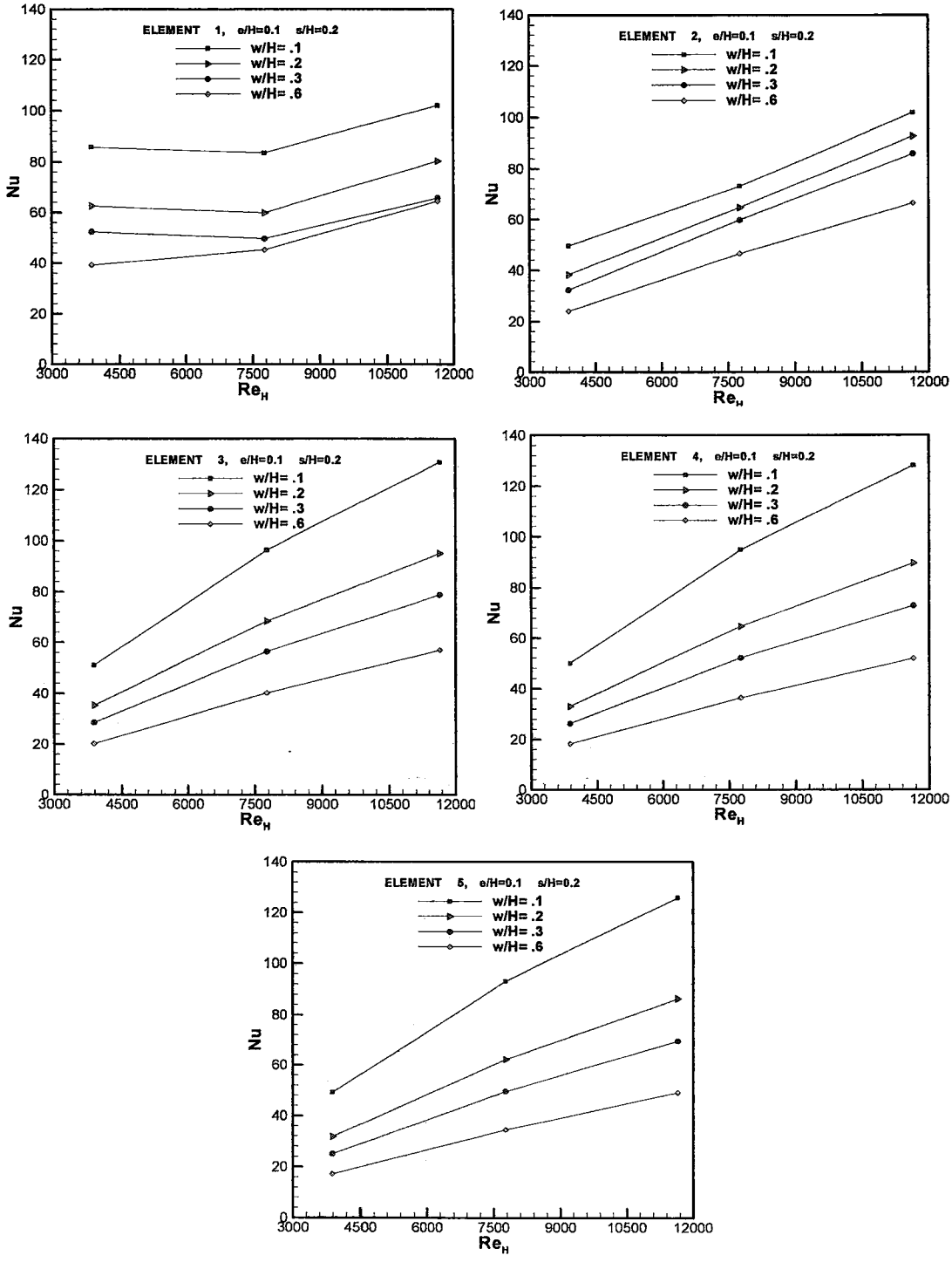

Figure 4.29 Average Nusselt number at different flow rates

Figures 4.30 and 4.31 show the corresponding streamlines.

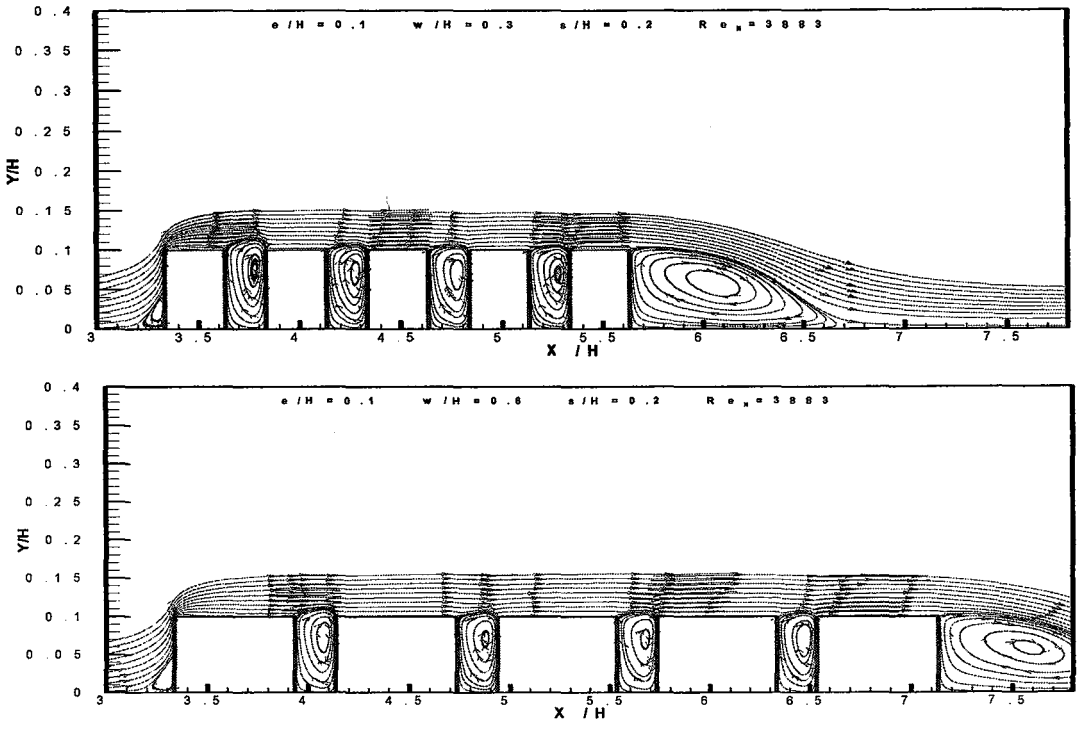

Figure 4.30 Streamlines of different element widths, $\mathrm{Re}_H = 3883$

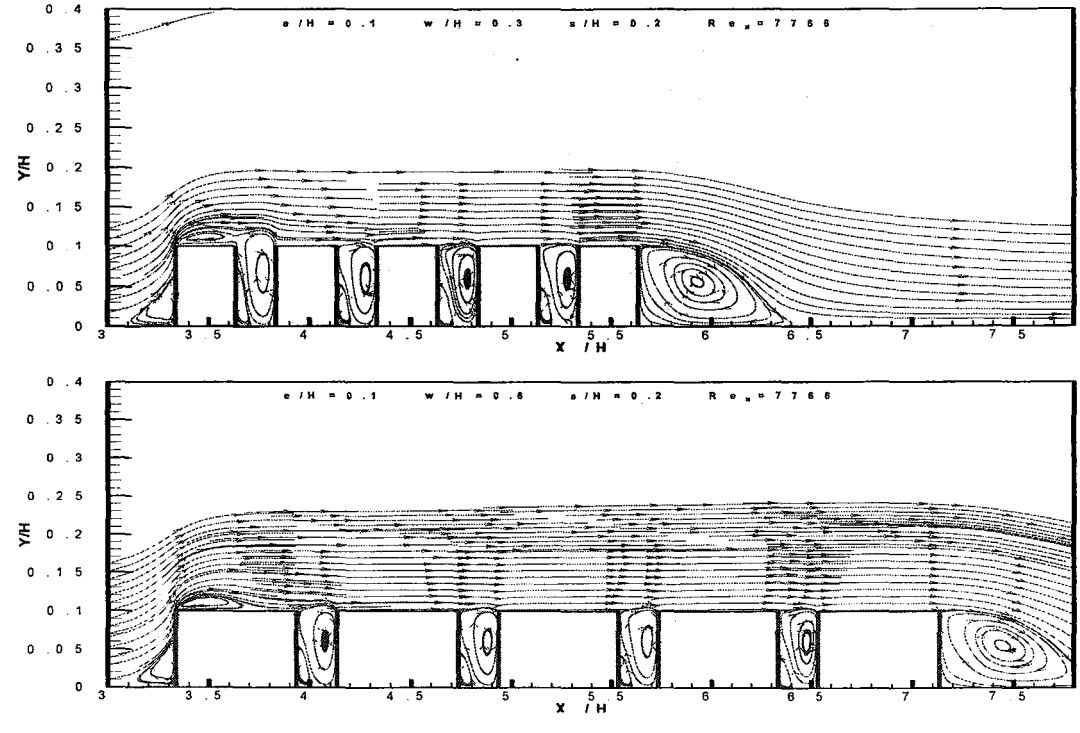

Figure 4.31 Streamlines of different element widths, $\mathrm{Re}_H = 7766$

4.6.5 Effect of Element Width and Element Step Width

An element width increase reduces the heat transfer rate. This increase tends to a limit, as depicted in figure 4.32. That is when geometric conditions resemble a flat plate with constant heat flux.

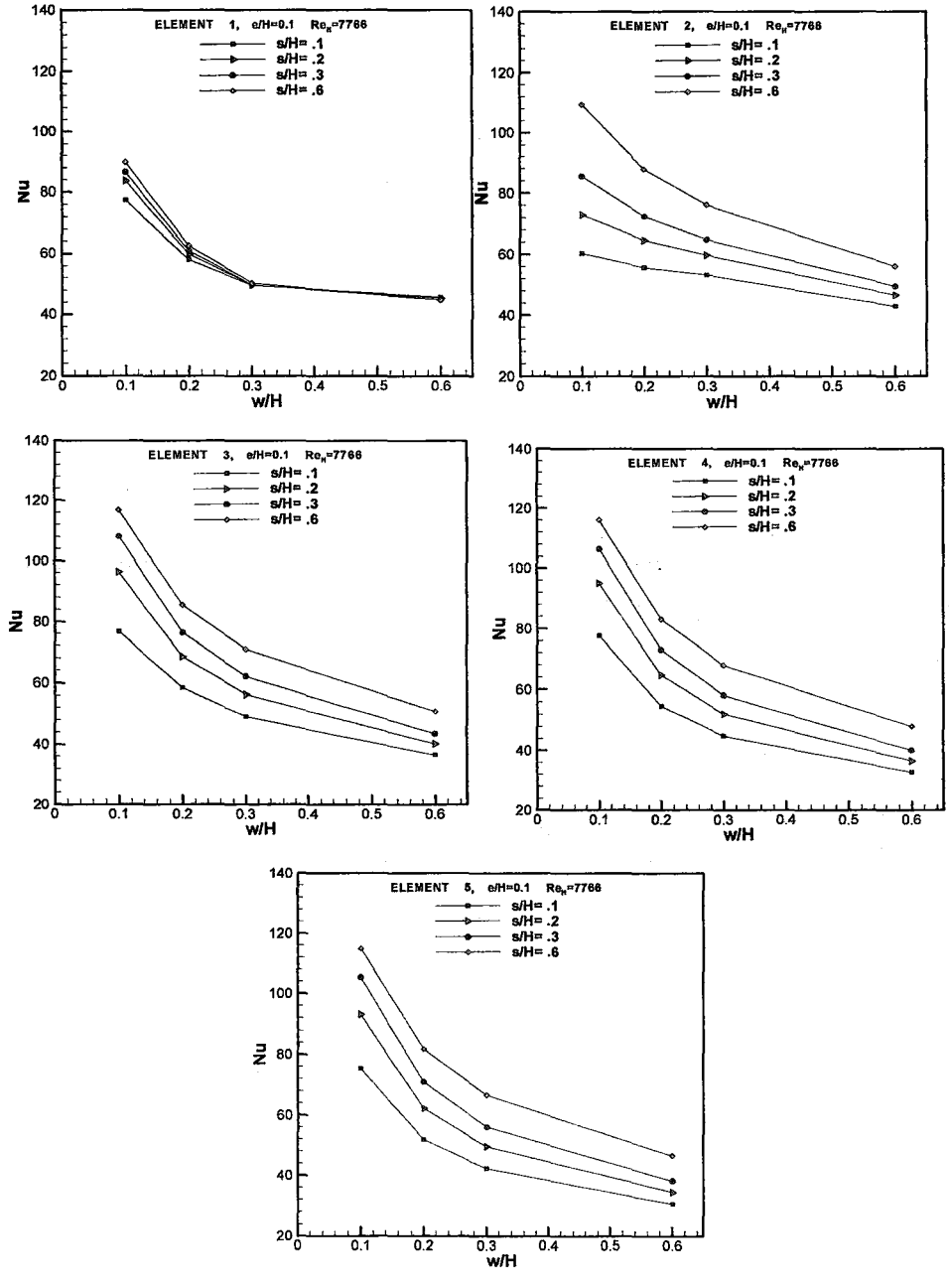

Figure 4.32 Average Nusselt number of different element widths

Figure 4.33 shows that an increase of element step width has a favourable effect on the heat transfer rate. This increase is more obvious in higher element heights.

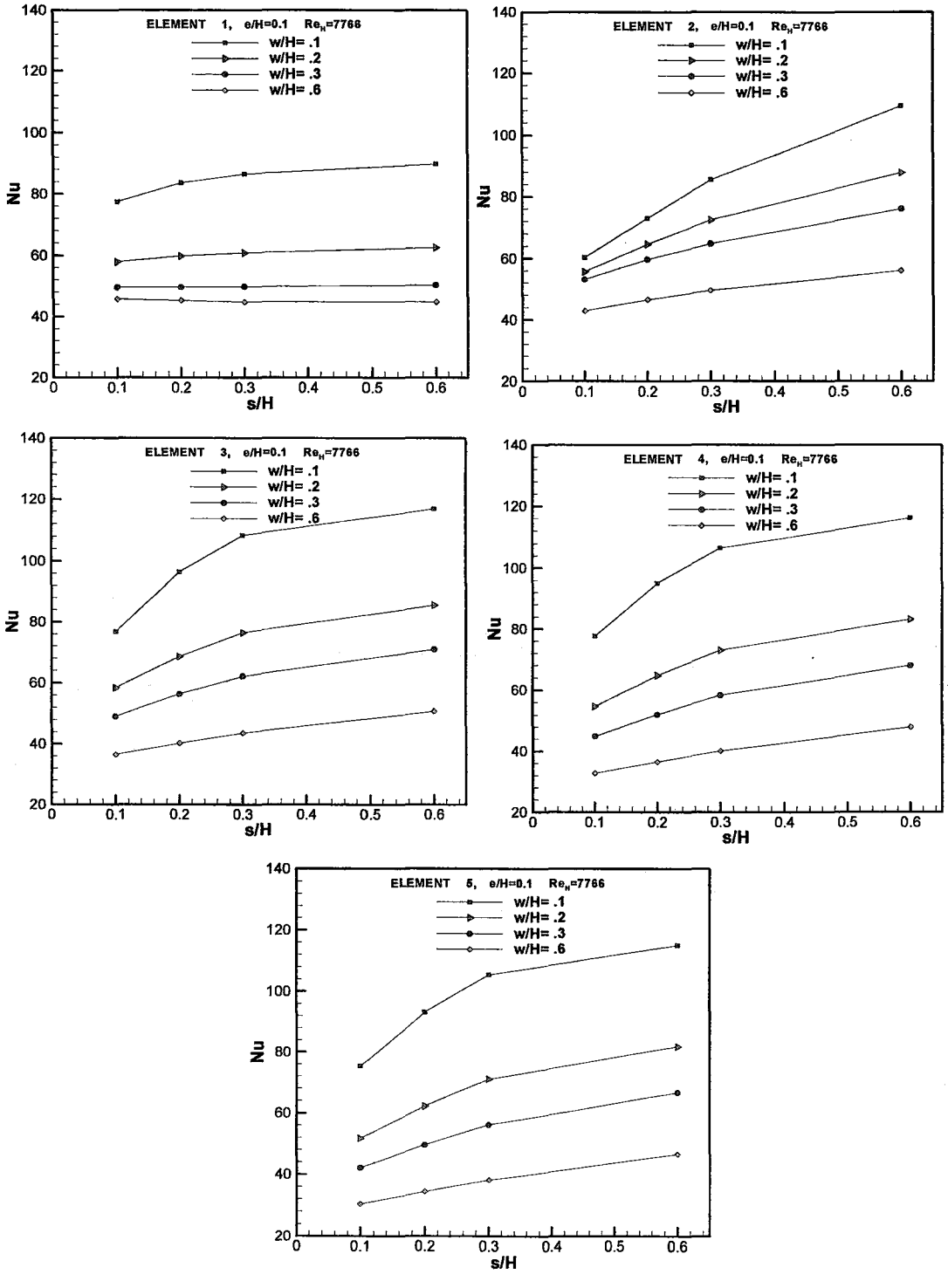

Figure 4.33 Average Nusselt number of different element steps

4.6.6 Effect of Reynolds Number and Element Step Width

The effects of step size and flow rate are depicted in figures 4.34 and 4.35, both of which result in a heat transfer increase.

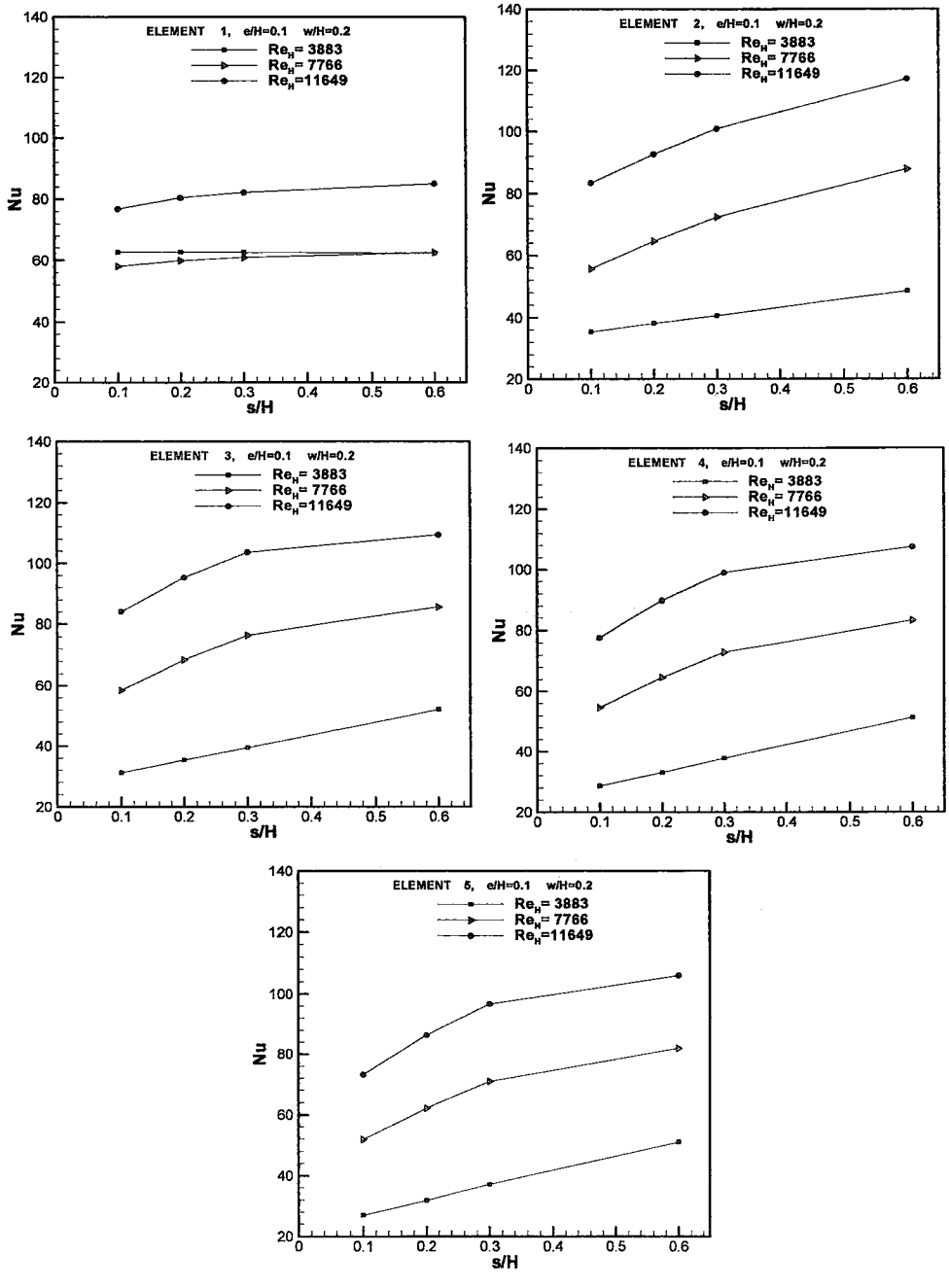

Figure 4.34 Average Nusselt number of different element steps

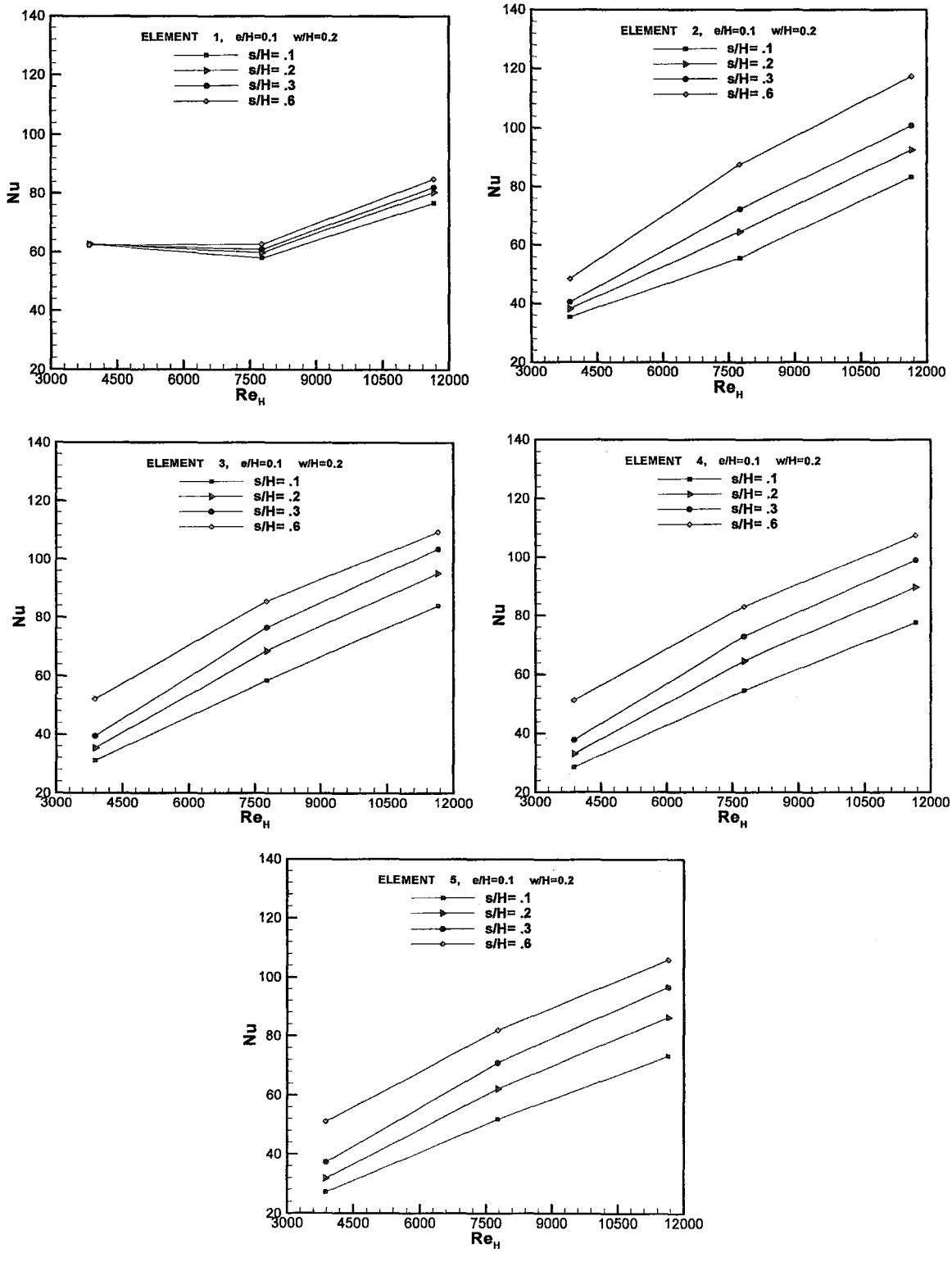

Figure 4.35 Average Nusselt number of different flow rate

Chapter Five

Design Guidelines and Regression Analysis

5.1 Introduction

In this chapter, a correlation for the average Nusselt number of each element depending on geometric parameters and flow rate is derived. As shown in the previous chapter, average Nusselt number is depending on the element height, width, and step size, and on Reynolds number as well. The proposed correlation form

$$Nu_H = m\ \mathrm{Re}_H{}^n \left(\frac{e}{H}\right)^{\alpha}\left(\frac{w}{H}\right)^{\beta}\left(\frac{s}{H}\right)^{\gamma} \tag{5.1}$$

where m, n, α, β, and γ are all constants. The dependent variables in the right hand side of equation 5.1 are in the range of

$$3883 \le \mathrm{Re}_H \le 11649,\ 0.025 \le \left(\frac{e}{H}\right) \le 0.2,\ 0.1 \le \left(\frac{w}{H}\right) \le 0.6,\ 0.1 \le \left(\frac{s}{H}\right) \le 0.6 \tag{5.2}$$

The problem can be summarized in determining the unknown constants in equation 5.1 using Excel 9.0 [44]. Also, a correlation analyses has been performed to avoid highly correlated variables.

5.2 Regression Analysis

The regression analysis on each element is divided into two sections. In the first section, the regression analysis is to be validated for specified values of Reynolds number and in the second section; the regression analysis has considers the entire range of Reynolds number. The data from this analysis are presented in tables 5.1 and 5.2 for each specified values of Reynolds number, where negative values show that an increase of the relevant parameter has a negative effect on the mean Nusselt number and vice versa.

Table 5.1 Regression analysis for each specified values of Reynolds number

Re_H		m	α	β	γ	n	Average Difference of Predicted Values
Element 1	3883	2.603	-0.267	-0.438	0.043	0.214	14%
	7766	2.139	-0.224	-0.358	0.042	0.277	10%
	11649	4.704	-0.156	-0.288	0.041	0.232	8%
Element 2	3883	2.962	-0.014	-0.426	0.170	0.261	8%
	7766	1.226	0.104	-0.364	0.189	0.446	7%
	11649	4.742	0.109	-0.335	0.155	0.316	6%
Element 3	3883	3.181	0.136	-0.501	0.236	0.291	8%
	7766	0.648	0.182	-0.457	0.213	0.525	5%
	11649	5.844	0.173	-0.426	0.164	0.295	5%
Element 4	3883	2.990	0.190	-0.554	0.255	0.303	7%
	7766	1.139	0.196	-0.501	0.226	0.456	4%
	11649	1.966	0.186	-0.469	0.180	0.405	4%
Element 5	3883	2.208	0.206	-0.582	0.273	0.338	6%
	7766	1.068	0.195	-0.526	0.235	0.456	3%
	11649	5.055	0.186	-0.492	0.190	0.299	3%

Table 5.2 Regression analysis for the range of Reynolds number used

Parameters	m	α	β	γ	n	Average Difference of Predicted Values
Element 1	0.468	-0.216	-0.361	0.042	0.450	11%
Element 2	0.061	0.066	-0.375	0.171	0.764	8%
Element 3	0.060	0.163	-0.462	0.204	0.783	6%
Element 4	0.053	0.190	-0.508	0.220	0.793	5%
Element 5	0.047	0.196	-0.534	0.232	0.802	5%

5.3 Analogy with Previous Correlations

Many correlations can be found in the literature [7] for fully developed turbulent flow between two smooth parallel plates. Ditus-Bolter correlation is one of the most known correlations that equation 5.3 has been proposed and used for fully developed turbulent flow [45]. The exponent of Reynolds number in this equation agrees well with the fifth element Reynolds number exponent, n. It can be seen from the agreement between the values of the constants of elements four and five, shown in table 5.2, the flow has already developed.

$$Nu_{Dh} = 0.023 \ \mathrm{Re}_{Dh}^{0.8} \ \mathrm{Pr}^{0.4} \quad , \mathrm{Re}_{Dh} \geq 3000 \text{ (Turbulent Flow)} \tag{5.3}$$

This equation, for air with $\mathrm{Pr} = 0.7$, can be rewritten as

$$Nu_{Dh} = 0.02 \ \mathrm{Re}_{Dh}^{0.8} \tag{5.4}$$

For turbulent forced convection in electronic packaging the following correlation has been also proposed [2].

$$Nu_{w} = 0.0935 \ \mathrm{Re}_{C}^{0.72} \tag{5.5}$$

where Nu_w is the average Nusselt number based on element width, w, and Re_C is the channel Reynolds number based on channel clearance height, C.

$$Nu_{e} = 0.075 \ \mathrm{Re}_{e}^{0.653} \left(\frac{e}{C}\right)^{0.543} \left(\frac{w}{e}\right)^{1.48} \tag{5.6}$$

where Nu_e and Re_e are the average Nusselt number and Reynolds number based on element height, e, respectively.

Experimental work of Vafai et al. [25] suggests equation 5.7 for average Nusselt number on each element. The corresponding values are presented in table 5.3. It can be seen from equation 5.3 to 5.7 that all proposed correlations for average Nusselt number in a channel flow with discrete heat sources are in the form of power law trend. In the limit, which elements are closely located in the stream wise direction, average Nusselt number profile shows to have a limit in the fully developed region of the channel that resembles a uniformly heated channel flow.

$$Nu_H = A\ \mathrm{Re}_{Dh}{}^{B} \qquad T_{ref} = T_{inlet} \tag{5.7}$$

where Nu_H is the average Nusselt number based on channel height, H, and Re_{Dh} is the channel Reynolds number based on hydraulic diameter of the channel.

Table 5.3 Data values of equation 5.7

Parameters	A	B	$\leq \mathrm{Re}_{Dh} \leq$	
Element 1	0.0140	0.940	5000	13000
Element 2	0.0672	0.746	5000	13000
Element 3	0.0212	0.860	5000	13000
Element 4	0.0244	0.833	5000	13000
Element 5	0.0338	0.794	5000	13000

5.4 Data Analysis

5.4.1 Parameters Maximizing and Minimizing Nusselt Number

In this section, the design parameters that maximize minimize Nusselt number values of each element are presented. The values of these parameters are constrained with

in the range of the present parametric study. These values have been obtained by applying excel 9.0 on the data shown in table 5.2 and are shown in table 5.3 and table 5.4, for Reynolds number of 11649 and 3883, respectively.

Table 5.4 Parameters maximizing Nu_m

Parameters	e/H	w/H	s/H	Re_H
Element 1	0.025	0.1	0.6	11649
Element 2	0.2	0.1	0.6	11649
Element 3	0.2	0.1	0.6	11649
Element 4	0.2	0.1	0.6	11649
Element 5	0.2	0.1	0.6	11649

Table 5.5 Parameters minimizing Nu_m

Parameters	e/H	w/H	s/H	Re_H
Element 1	0.2	0.6	0.1	3883
Element 2	0.025	0.6	0.1	3883
Element 3	0.025	0.6	0.1	3883
Element 4	0.025	0.6	0.1	3883
Element 5	0.025	0.6	0.1	3883

Table 5.3 and table 5.4 show that with an exception of the first element an increase of e/H and s/H and a decrease of w/H increases Nusselt number. But from the standpoint of design, it is important to know how a specific parameter, can be changed to gain the best heat transfer rate. In other words, we must determine which parameter is the most affecting one. As an example, assume we are increasing all the element geometric parameters which are initially at: $e/H = 0.1$, $w/H = 0.1$, and $s/H = 0.1$ by 10% and this will be done at $\mathrm{Re}_H = 7766$. The changes of Nusselt number obtained by using the data from table 5.4 in equation 5.1 are shown in table 5.6. This analysis indicates that the most controlling parameter that significantly affects Nusselt

number is w/H. And the best way to increase Nusselt number is by minimizing this parameter to the least acceptable value from the design point of view.

Table 5.6 Percent change of Average Nusselt number with 10% increases of each parameter

Parameters	e/H	w/H	s/H
Element 1	-14%	-22%	3%
Element 2	5%	-23%	13%
Element 3	12%	-27%	15%
Element 4	14%	-30%	17%
Element 5	15%	-31%	17%
Average	6%	-27%	13%

Chapter Six

Summary and Concluding Remarks

6.1 Summary

The present parametric study is focusing on electronic packages. The study starts with investigating the most appropriate turbulent model which is able to capture heat transfer and flow fields in ribbed channels which simulates the electronic package and use this model to investigate the influence of geometric and flow parameters affecting the rate of heat transfer in this configuration.

Two parallel plates form the geometry of the present study, and turbulent flow is allowed through the resulting passage. The upper plate is smooth, and the two plates are a distant H (channel height) apart. The lower plate has five identical ribs of height e, length w, and distance s between two successive ribs. The parametric study in this research involves four parameters. Three of these are normalized geometric parameters: $0.025 \le e/H \le 0.2$, $0.1 \le w/H \le 0.6$, and $0.1 \le s/H \le 0.6$. The fourth parameter which is the mean inlet air velocity concerns the hydrodynamic aspects of the flow field. The parameter changes from 2 to 6 m/s, which is equivalent to Reynolds number based on channel height of $3883 \le \mathrm{Re}_H \le 11649$. Figure 6.1 shows the geometry of the present study.

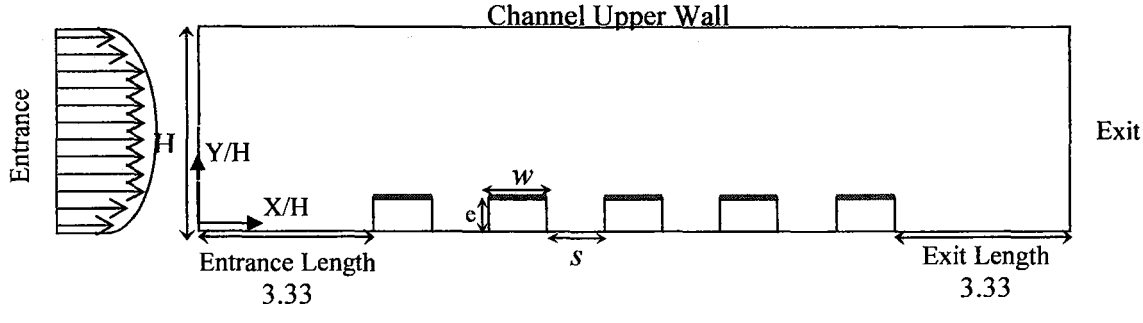

Figure 6.1 Geometry of parametric study

6.2 Conclusion

The present investigation leads to the following conclusions:

- The standard $k-\varepsilon$ and RNG $k-\varepsilon$ turbulent models (with use of wall function) were unable to capture the flow and temperature field in a ribbed forced convection channel for the range of Reynolds number used in this study, $3883 \leq \mathrm{Re}_H \leq 11649$. The Lack of sensitivity of these models to the adverse pressure gradients, separation, and, hence, their ability to capture phenomena such as those occurring in two-dimensional ribbed channel flow (recirculation for example) is mainly due to the fact that the $k-\varepsilon$ and *RNG* $k-\varepsilon$ models use wall functions to bridge the viscous sub-layer with the buffer layer rather than solve for it.

- Both the Omega Reynolds Stress Model (*ω-RSM*) and Shear Stress Transport model (*SST*) exhibit a good prediction of flow and thermal fields for the cases investigated in the current study with separation, circulation, and reattachment. The preference of Reynolds stress model over SST model shown in this investigation was not that high keeping in mind the time consumed in solving the extra transport equations involved in Reynolds stress model.

- Although the Stress Transport (*SST*) model is sometimes insensitive to the velocity gradient $\frac{\partial \overline{V}}{\partial x}$. It is in our opinion; the most appropriate model to conduct a parametric study of too many parameters such that done in the present work in a less time is the SST model. The model needs to be further validated in more complex flow regimes, such as those arise with more populated boards at different heat fluxes and element heights, as in the case of real electronic packages.

- For all the cases studied in this research ($0.025 \le e/H \le 0.2, 0.1 \le w/H \le 0.6$, $0.1 \le s/H \le 0.6$, and $3883 \le \mathrm{Re}_H \le 11649$) It was found that the heat transfer rate for the first element decreases by increasing either the element height (e) or the element width (w) or both, and increases by increasing Reynolds number (Re_H), and step size (s).

- With an exception of the first element, the heat transfer rate increases by increasing Reynolds number (Re_H), element height (e), and step size (s), while it decreases by increasing the element width (w).

- The recirculation zone formed on the top surface of the first element locks and traps heat from being removed by the cold free stream. Increasing the width of the first element helps in increasing the strength of the top surface shear layer and delays or dampens separation on this element, which in turn helps the transfer of heat into the core flow. Further increase, however thickens, the boundary layer on the later elements and increases thermal resistance causing heat transfer to diminish. The size and strength of the circulation zone on the top surface of the first element increases by increasing the step width (s), the element height (e), and the mean inlet velocity (U_m) regardless of the *attack angle*.

- Increasing the element height narrows the flow passage and accelerates the flow increasing its ability to remove more heat in a shorter time. In addition, increasing the element height augments more turbulence in the flow field.

- Increasing the step width promotes more circulation in the flow which subsequently increases the rate of heat transfer from the elements.

Chapter Seven

Recommendation for Future Work

7.1 Future work

The parametric study done in the present work creates some issues that is recommended to be taken into considerations in any further investigation related this work. These issues are:

- Consideration of the three dimensionality effect.

- Thinking of a new design that improves the flow patterns on the first row of elements suggesting that the upper edge of these elements is better being convex instead of sharp ending to dampen separation on this surface. It is recommended to consider different channel geometries.

- The SST model needs to be further tested in more complex flow geometries.

- It was shown, in the present work that flow becomes more stable, tending to be, if it is right to say, fully developed after some distance from the beginning of the ribbed portion. This distance needs more accurate determination and its dependency on the geometry and flow parameters needs to be considered. In this case the effect of the number of elements should be included.

- Applications of ribbed channel flow can be extended to such as those occurring in heat exchangers with different fluid medium (for example; oil, and water) by taking into account the effect of Prandtl number.

Appendix A

Detailed Results of the Parametric Study:

Table A.1 Study Cases of the Parametric Study

Study Case	$e\ [mm]$	$w\ [mm]$	$s\ [mm]$	$U_m\ [m/s]$	Re_H	Dissipating Power (Watts)
1	0.75	3	3	2	3883	15
2	0.75	3	3	4	7766	15
3	0.75	3	3	6	11649	15
4	0.75	3	6	2	3883	15
5	0.75	3	6	4	7766	15
6	0.75	3	6	6	11649	15
7	0.75	3	9	2	3883	15
8	0.75	3	9	4	7766	15
9	0.75	3	9	6	11649	15
10	0.75	3	18	2	3883	15
11	0.75	3	18	4	7766	15
12	0.75	3	18	6	11649	15
13	0.75	6	3	2	3883	30
14	0.75	6	3	4	7766	30
15	0.75	6	3	6	11649	30
16	0.75	6	6	2	3883	30
17	0.75	6	6	4	7766	30
18	0.75	6	6	6	11649	30
19	0.75	6	9	2	3883	30
20	0.75	6	9	4	7766	30
21	0.75	6	9	6	11649	30
22	0.75	6	18	2	3883	30
23	0.75	6	18	4	7766	30
24	0.75	6	18	6	11649	30
25	0.75	9	3	2	3883	45
26	0.75	9	3	4	7766	45
27	0.75	9	3	6	11649	45
28	0.75	9	6	2	3883	45
29	0.75	9	6	4	7766	45
30	0.75	9	6	6	11649	45
31	0.75	9	9	2	3883	45
32	0.75	9	9	4	7766	45
33	0.75	9	9	6	11649	45
34	0.75	9	18	2	3883	45
35	0.75	9	18	4	7766	45
36	0.75	9	18	6	11649	45
37	0.75	18	3	2	3883	90
38	0.75	18	3	4	7766	90
39	0.75	18	3	6	11649	90
40	0.75	18	6	2	3883	90
41	0.75	18	6	4	7766	90
42	0.75	18	6	6	11649	90
43	0.75	18	9	2	3883	90
44	0.75	18	9	4	7766	90
45	0.75	18	9	6	11649	90
46	0.75	18	18	2	3883	90

Table A.1 Study Cases of the Parametric Study-Continued

Study Case	$e\ [mm]$	$w\ [mm]$	$s\ [mm]$	$U_m\ [m/s]$	Re_H	Dissipating Power (Watts)
47	0.75	18	18	4	7766	90
48	0.75	18	18	6	11649	90
49	1.5	3	3	2	3883	15
50	1.5	3	3	4	7766	15
51	1.5	3	3	6	11649	15
52	1.5	3	6	2	3883	15
53	1.5	3	6	4	7766	15
54	1.5	3	6	6	11649	15
55	1.5	3	9	2	3883	15
56	1.5	3	9	4	7766	15
57	1.5	3	9	6	11649	15
58	1.5	3	18	2	3883	15
59	1.5	3	18	4	7766	15
60	1.5	3	18	6	11649	15
61	1.5	6	3	2	3883	30
62	1.5	6	3	4	7766	30
63	1.5	6	3	6	11649	30
64	1.5	6	6	2	3883	30
65	1.5	6	6	4	7766	30
66	1.5	6	6	6	11649	30
67	1.5	6	9	2	3883	30
68	1.5	6	9	4	7766	30
69	1.5	6	9	6	11649	30
70	1.5	6	18	2	3883	30
71	1.5	6	18	4	7766	30
72	1.5	6	18	6	11649	30
73	1.5	9	3	2	3883	45
74	1.5	9	3	4	7766	45
75	1.5	9	3	6	11649	45
76	1.5	9	6	2	3883	45
77	1.5	9	6	4	7766	45
78	1.5	9	6	6	11649	45
79	1.5	9	9	2	3883	45
80	1.5	9	9	4	7766	45
81	1.5	9	9	6	11649	45
82	1.5	9	18	2	3883	45
83	1.5	9	18	4	7766	45
84	1.5	9	18	6	11649	45
85	1.5	18	3	2	3883	90
86	1.5	18	3	4	7766	90
87	1.5	18	3	6	11649	90
88	1.5	18	6	2	3883	90
89	1.5	18	6	4	7766	90
90	1.5	18	6	6	11649	90
91	1.5	18	9	2	3883	90
92	1.5	18	9	4	7766	90

Table A.1 Study Cases of the Parametric Study-Continued

Study Case	$e\ [mm]$	$w\ [mm]$	$s\ [mm]$	$U_m\ [m/s]$	Re_H	Dissipating Power (Watts)
93	1.5	18	9	6	11649	90
94	1.5	18	18	2	3883	90
95	1.5	18	18	4	7766	90
96	1.5	18	18	6	11649	90
97	3	3	3	2	3883	15
98	3	3	3	4	7766	15
99	3	3	3	6	11649	15
100	3	3	6	2	3883	15
101	3	3	6	4	7766	15
102	3	3	6	6	11649	15
103	3	3	9	2	3883	15
104	3	3	9	4	7766	15
105	3	3	9	6	11649	15
106	3	3	18	2	3883	15
107	3	3	18	4	7766	15
108	3	3	18	6	11649	15
109	3	6	3	2	3883	30
110	3	6	3	4	7766	30
111	3	6	3	6	11649	30
112	3	6	6	2	3883	30
113	3	6	6	4	7766	30
114	3	6	6	6	11649	30
115	3	6	9	2	3883	30
116	3	6	9	4	7766	30
117	3	6	9	6	11649	30
118	3	6	18	2	3883	30
119	3	6	18	4	7766	30
120	3	6	18	6	11649	30
121	3	9	3	2	3883	45
122	3	9	3	4	7766	45
123	3	9	3	6	11649	45
124	3	9	6	2	3883	45
125	3	9	6	4	7766	45
126	3	9	6	6	11649	45
127	3	9	9	2	3883	45
128	3	9	9	4	7766	45
129	3	9	9	6	11649	45
130	3	9	18	2	3883	45
131	3	9	18	4	7766	45
132	3	9	18	6	11649	45
133	3	18	3	2	3883	90
134	3	18	3	4	7766	90
135	3	18	3	6	11649	90
136	3	18	6	2	3883	90
137	3	18	6	4	7766	90
138	3	18	6	6	11649	90

Table A.1 Study Cases of the Parametric Study-Continued

Study Case	$e\ [mm]$	$w\ [mm]$	$s\ [mm]$	$U_m\ [m/s]$	Re_H	Dissipating Power (Watts)
139	3	18	9	2	3883	90
140	3	18	9	4	7766	90
141	3	18	9	6	11649	90
142	3	18	18	2	3883	90
143	3	18	18	4	7766	90
144	3	18	18	6	11649	90
145	6	3	3	2	3883	15
146	6	3	3	4	7766	15
147	6	3	3	6	11649	15
148	6	3	6	2	3883	15
149	6	3	6	4	7766	15
150	6	3	6	6	11649	15
151	6	3	9	2	3883	15
152	6	3	9	4	7766	15
153	6	3	9	6	11649	15
154	6	3	18	2	3883	15
155	6	3	18	4	7766	15
156	6	3	18	6	11649	15
157	6	6	3	2	3883	30
158	6	6	3	4	7766	30
159	6	6	3	6	11649	30
160	6	6	6	2	3883	30
161	6	6	6	4	7766	30
162	6	6	6	6	11649	30
163	6	6	9	2	3883	30
164	6	6	9	4	7766	30
165	6	6	9	6	11649	30
166	6	6	18	2	3883	30
167	6	6	18	4	7766	30
168	6	6	18	6	11649	30
169	6	9	3	2	3883	45
170	6	9	3	4	7766	45
171	6	9	3	6	11649	45
172	6	9	6	2	3883	45
173	6	9	6	4	7766	45
174	6	9	6	6	11649	45
175	6	9	9	2	3883	45
176	6	9	9	4	7766	45
177	6	9	9	6	11649	45
178	6	9	18	2	3883	45
179	6	9	18	4	7766	45
180	6	9	18	6	11649	45
181	6	18	3	2	3883	90
182	6	18	3	4	7766	90
183	6	18	3	6	11649	90
184	6	18	6	2	3883	90

Table A.1 Study Cases of the Parametric Study-Continued

Study Case	$e\ [mm]$	$w\ [mm]$	$s\ [mm]$	$U_m\ [m/s]$	Re_H	Dissipating Power (Watts)
185	6	18	6	4	7766	90
186	6	18	6	6	11649	90
187	6	18	9	2	3883	90
188	6	18	9	4	7766	90
189	6	18	9	6	11649	90
190	6	18	18	2	3883	90
191	6	18	18	4	7766	90
192	6	18	18	6	11649	90

Table A.2 Average Nusselt Number

Study Case	Dimensionless Parameters				Average Nusselt Number				
	e/H	w/H	s/H	Re_H	Element 1	Element 2	Element 3	Element 4	Element 5
1	0.025	0.1	0.1	3883	92.10	55.29	45.71	40.73	37.83
2	0.025	0.1	0.1	7766	130.59	79.41	67.79	62.28	59.73
3	0.025	0.1	0.1	11649	157.42	103.64	92.85	87.20	84.26
4	0.025	0.1	0.2	3883	92.76	60.40	51.27	46.44	43.69
5	0.025	0.1	0.2	7766	130.92	88.41	80.13	76.53	74.92
6	0.025	0.1	0.2	11649	157.36	119.46	110.77	105.24	102.67
7	0.025	0.1	0.3	3883	93.34	64.31	55.59	50.93	48.35
8	0.025	0.1	0.3	7766	131.37	96.29	90.02	86.15	83.94
9	0.025	0.1	0.3	11649	157.84	128.33	118.73	113.30	110.67
10	0.025	0.1	0.6	3883	94.50	72.22	64.53	60.62	58.98
11	0.025	0.1	0.6	7766	132.85	110.40	103.98	99.73	97.23
12	0.025	0.1	0.6	11649	159.66	137.72	129.68	124.93	122.16
13	0.025	0.2	0.1	3883	67.78	38.05	30.98	27.35	25.25
14	0.025	0.2	0.1	7766	96.54	55.84	47.36	43.50	41.73
15	0.025	0.2	0.1	11649	118.19	75.17	66.29	61.51	58.97
16	0.025	0.2	0.2	3883	68.23	41.19	34.19	30.55	28.46
17	0.025	0.2	0.2	7766	96.94	61.83	55.03	51.94	50.32
18	0.025	0.2	0.2	11649	118.38	85.36	77.35	72.65	70.24
19	0.025	0.2	0.3	3883	68.59	43.69	36.84	33.24	31.25
20	0.025	0.2	0.3	7766	97.27	67.24	61.57	58.19	56.16
21	0.025	0.2	0.3	11649	118.78	91.48	83.10	78.41	75.94
22	0.025	0.2	0.6	3883	69.33	49.10	42.79	39.69	38.38
23	0.025	0.2	0.6	7766	98.30	77.17	71.38	67.72	65.53
24	0.025	0.2	0.6	11649	120.16	98.79	91.57	87.32	84.80
25	0.025	0.3	0.1	3883	56.71	30.80	24.95	21.94	20.20
26	0.025	0.3	0.1	7766	81.00	46.00	39.20	36.11	34.57
27	0.025	0.3	0.1	11649	100.34	63.03	55.28	51.06	48.82
28	0.025	0.3	0.2	3883	57.02	33.05	27.18	24.13	22.40
29	0.025	0.3	0.2	7766	81.30	50.58	44.88	42.09	40.48
30	0.025	0.3	0.2	11649	100.46	70.70	63.44	59.25	57.04
31	0.025	0.3	0.3	3883	57.30	34.90	29.08	26.05	24.37
32	0.025	0.3	0.3	7766	81.60	54.66	49.59	46.53	44.70
33	0.025	0.3	0.3	11649	100.75	75.18	67.75	63.56	61.27
34	0.025	0.3	0.6	3883	57.83	39.05	33.57	30.94	29.82
35	0.025	0.3	0.6	7766	82.38	62.51	57.21	53.94	51.99
36	0.025	0.3	0.6	11649	101.80	81.21	74.57	70.69	68.37
37	0.025	0.6	0.1	3883	41.89	21.85	17.63	15.46	14.23
38	0.025	0.6	0.1	7766	60.47	34.22	29.68	27.26	25.84
39	0.025	0.6	0.1	11649	76.85	48.06	41.98	38.69	36.91
40	0.025	0.6	0.2	3883	42.03	23.03	18.76	16.58	15.37
41	0.025	0.6	0.2	7766	60.63	37.01	32.79	30.35	28.89
42	0.025	0.6	0.2	11649	76.83	52.43	46.56	43.25	41.43
43	0.025	0.6	0.3	3883	42.15	24.04	19.77	17.61	16.47
44	0.025	0.6	0.3	7766	60.74	39.46	35.31	32.78	31.27
45	0.025	0.6	0.3	11649	76.83	55.08	49.23	45.92	44.03

Table A.2 Average Nusselt Number -Continued

Study Case	Dimensionless Parameters				Average Nusselt Number				
	e/H	w/H	s/H	Re_H	Element 1	Element 2	Element 3	Element 4	Element 5
46	0.025	0.6	0.6	3883	42.41	26.47	22.38	20.58	19.86
47	0.025	0.6	0.6	7766	61.11	44.28	39.88	37.30	35.74
48	0.025	0.6	0.6	11649	77.41	59.08	53.58	50.43	48.51
49	0.05	0.1	0.1	3883	98.06	56.28	46.79	41.90	39.14
50	0.05	0.1	0.1	7766	124.84	77.68	69.47	65.22	63.31
51	0.05	0.1	0.1	11649	120.17	98.10	97.60	93.21	90.48
52	0.05	0.1	0.2	3883	98.05	60.28	52.37	48.05	45.83
53	0.05	0.1	0.2	7766	124.44	87.51	85.54	83.24	82.40
54	0.05	0.1	0.2	11649	119.81	116.59	118.69	114.95	113.45
55	0.05	0.1	0.3	3883	98.06	63.25	56.97	53.36	52.05
56	0.05	0.1	0.3	7766	124.16	96.79	97.30	94.60	93.69
57	0.05	0.1	0.3	11649	119.78	129.46	128.06	124.25	123.00
58	0.05	0.1	0.6	3883	98.28	72.00	69.64	68.30	67.76
59	0.05	0.1	0.6	7766	124.23	114.49	106.41	103.31	101.54
60	0.05	0.1	0.6	11649	119.89	143.89	125.00	123.91	121.22
61	0.05	0.2	0.1	3883	71.58	38.82	31.71	28.13	26.13
62	0.05	0.2	0.1	7766	93.08	56.27	49.13	45.76	44.20
63	0.05	0.2	0.1	11649	94.65	76.15	69.95	65.40	62.86
64	0.05	0.2	0.2	3883	71.76	41.70	35.03	31.58	29.74
65	0.05	0.2	0.2	7766	93.14	63.18	58.80	56.14	54.82
66	0.05	0.2	0.2	11649	94.48	87.71	82.95	78.89	76.93
67	0.05	0.2	0.3	3883	71.86	43.96	37.89	34.72	33.30
68	0.05	0.2	0.3	7766	93.05	69.86	66.87	64.10	62.83
69	0.05	0.2	0.3	11649	94.34	96.67	90.99	86.95	85.22
70	0.05	0.2	0.6	3883	72.15	49.89	46.04	44.67	44.14
71	0.05	0.2	0.6	7766	93.28	82.13	75.56	72.39	70.81
72	0.05	0.2	0.6	11649	94.74	105.64	93.91	90.76	88.88
73	0.05	0.3	0.1	3883	59.56	31.42	25.54	22.57	20.91
74	0.05	0.3	0.1	7766	78.62	46.94	40.95	38.04	36.51
75	0.05	0.3	0.1	11649	83.56	65.34	58.52	54.21	51.88
76	0.05	0.3	0.2	3883	59.73	33.62	27.89	24.94	23.36
77	0.05	0.3	0.2	7766	78.70	52.36	47.94	45.27	43.86
78	0.05	0.3	0.2	11649	83.32	74.03	68.04	64.05	62.01
79	0.05	0.3	0.3	3883	59.88	35.39	29.94	27.12	25.78
80	0.05	0.3	0.3	7766	78.76	57.25	53.77	51.11	49.77
81	0.05	0.3	0.3	11649	83.40	80.36	74.35	70.48	68.65
82	0.05	0.3	0.6	3883	60.14	39.97	35.95	34.57	34.08
83	0.05	0.3	0.6	7766	79.02	67.22	61.56	58.57	57.05
84	0.05	0.3	0.6	11649	83.93	87.74	78.77	75.38	73.60
85	0.05	0.6	0.1	3883	43.61	22.32	18.09	15.91	14.71
86	0.05	0.6	0.1	7766	59.46	35.53	31.08	28.50	27.04
87	0.05	0.6	0.1	11649	68.48	50.63	44.32	40.71	38.80
88	0.05	0.6	0.2	3883	43.71	23.54	19.29	17.11	15.97
89	0.05	0.6	0.2	7766	59.47	38.74	34.70	32.22	30.84
90	0.05	0.6	0.2	11649	68.23	55.56	49.69	46.20	44.33

Table A.2 Average Nusselt Number -Continued

Study Case	Dimensionless Parameters				Average Nusselt Number				
	e/H	w/H	s/H	Re_H	Element 1	Element 2	Element 3	Element 4	Element 5
91	0.05	0.6	0.3	3883	43.80	24.58	20.39	18.29	17.32
92	0.05	0.6	0.3	7766	59.47	41.73	38.03	35.64	34.32
93	0.05	0.6	0.3	11649	68.08	59.42	53.77	50.37	48.59
94	0.05	0.6	0.6	3883	43.98	27.34	23.88	22.74	22.25
95	0.05	0.6	0.6	7766	59.68	48.18	43.77	41.24	39.84
96	0.05	0.6	0.6	11649	68.47	64.69	58.54	55.41	53.72
97	0.1	0.1	0.1	3883	86.15	46.71	43.37	41.03	39.50
98	0.1	0.1	0.1	7766	77.46	60.35	76.82	77.60	75.35
99	0.1	0.1	0.1	11649	86.22	91.72	106.48	109.20	105.49
100	0.1	0.1	0.2	3883	85.88	49.56	51.04	49.95	49.25
101	0.1	0.1	0.2	7766	83.71	72.99	96.43	95.05	93.20
102	0.1	0.1	0.2	11649	102.13	101.83	130.88	128.22	125.85
103	0.1	0.1	0.3	3883	85.70	51.86	58.59	59.03	59.56
104	0.1	0.1	0.3	7766	86.55	85.52	108.27	106.46	105.42
105	0.1	0.1	0.3	11649	107.68	115.10	142.69	140.04	138.95
106	0.1	0.1	0.6	3883	85.54	63.92	77.90	77.10	77.01
107	0.1	0.1	0.6	7766	89.82	109.44	116.88	116.15	114.98
108	0.1	0.1	0.6	11649	114.09	139.88	142.43	144.46	142.78
109	0.1	0.2	0.1	3883	62.62	35.45	31.15	28.61	27.11
110	0.1	0.2	0.1	7766	58.01	55.70	58.49	54.72	51.88
111	0.1	0.2	0.1	11649	76.81	83.38	84.01	77.62	73.29
112	0.1	0.2	0.2	3883	62.67	38.29	35.40	33.11	31.84
113	0.1	0.2	0.2	7766	59.89	64.65	68.56	64.76	62.25
114	0.1	0.2	0.2	11649	80.51	92.66	95.23	89.80	86.39
115	0.1	0.2	0.3	3883	62.56	40.62	39.51	37.84	37.27
116	0.1	0.2	0.3	7766	60.93	72.48	76.47	72.98	71.02
117	0.1	0.2	0.3	11649	82.15	100.89	103.60	99.05	96.71
118	0.1	0.2	0.6	3883	62.34	48.54	52.22	51.35	51.05
119	0.1	0.2	0.6	7766	62.62	87.85	85.58	83.17	81.91
120	0.1	0.2	0.6	11649	85.03	117.23	109.49	107.53	106.05
121	0.1	0.3	0.1	3883	52.42	29.94	25.77	23.38	21.97
122	0.1	0.3	0.1	7766	49.66	53.21	49.19	44.94	42.30
123	0.1	0.3	0.1	11649	66.04	78.28	70.69	63.93	60.01
124	0.1	0.3	0.2	3883	52.51	32.35	28.71	26.36	25.08
125	0.1	0.3	0.2	7766	49.71	59.75	56.36	52.13	49.63
126	0.1	0.3	0.2	11649	65.75	85.88	78.96	72.95	69.55
127	0.1	0.3	0.3	3883	52.58	34.31	31.41	29.34	28.46
128	0.1	0.3	0.3	7766	49.89	64.83	62.17	58.28	56.17
129	0.1	0.3	0.3	11649	65.74	91.26	85.37	80.28	77.68
130	0.1	0.3	0.6	3883	52.46	40.30	40.71	39.88	39.54
131	0.1	0.3	0.6	7766	50.40	76.15	70.97	68.03	66.64
132	0.1	0.3	0.6	11649	66.59	103.02	93.06	89.78	88.15
133	0.1	0.6	0.1	3883	39.28	22.53	18.91	16.87	15.74
134	0.1	0.6	0.1	7766	45.75	42.96	36.55	32.73	30.58
135	0.1	0.6	0.1	11649	65.30	61.93	52.21	46.90	43.99

Table A.2 Average Nusselt Number -Continued

Study Case	Dimensionless Parameters				Average Nusselt Number				
	e/H	w/H	s/H	Re_H	Element 1	Element 2	Element 3	Element 4	Element 5
136	0.1	0.6	0.2	3883	39.37	23.94	20.33	18.29	17.25
137	0.1	0.6	0.2	7766	45.34	46.65	40.24	36.54	34.53
138	0.1	0.6	0.2	11649	64.46	66.35	56.98	51.85	49.11
139	0.1	0.6	0.3	3883	39.45	25.16	21.67	19.79	18.98
140	0.1	0.6	0.3	7766	44.84	49.61	43.63	40.10	38.25
141	0.1	0.6	0.3	11649	63.50	69.79	61.19	56.52	54.11
142	0.1	0.6	0.6	3883	39.47	28.74	26.91	26.10	25.64
143	0.1	0.6	0.6	7766	44.83	56.12	50.91	48.00	46.60
144	0.1	0.6	0.6	11649	63.60	76.38	69.19	65.58	63.87
145	0.2	0.1	0.1	3883	45.68	32.82	41.30	43.14	49.42
146	0.2	0.1	0.1	7766	62.94	74.37	85.97	80.52	92.01
147	0.2	0.1	0.1	11649	82.18	102.82	116.61	105.87	120.81
148	0.2	0.1	0.2	3883	52.28	47.51	50.30	63.98	68.52
149	0.2	0.1	0.2	7766	73.87	95.74	89.20	109.85	111.24
150	0.2	0.1	0.2	11649	93.31	119.10	117.78	142.10	144.62
151	0.2	0.1	0.3	3883	56.45	60.90	58.64	76.57	77.14
152	0.2	0.1	0.3	7766	79.13	108.37	107.84	122.12	121.45
153	0.2	0.1	0.3	11649	98.98	137.20	137.07	156.43	155.86
154	0.2	0.1	0.6	3883	64.37	58.57	93.28	91.98	91.03
155	0.2	0.1	0.6	7766	90.70	100.33	140.00	136.86	135.90
156	0.2	0.1	0.6	11649	110.70	131.80	177.79	171.77	171.45
157	0.2	0.2	0.1	3883	31.21	29.88	32.93	38.89	38.88
158	0.2	0.2	0.1	7766	52.31	68.61	68.04	71.76	67.94
159	0.2	0.2	0.1	11649	71.47	96.32	92.25	97.51	93.06
160	0.2	0.2	0.2	3883	34.54	38.95	42.86	47.58	45.79
161	0.2	0.2	0.2	7766	57.98	69.66	81.92	81.21	76.89
162	0.2	0.2	0.2	11649	75.98	98.25	108.41	108.37	103.25
163	0.2	0.2	0.3	3883	36.54	39.79	51.68	52.96	50.72
164	0.2	0.2	0.3	7766	64.13	72.77	91.30	86.67	82.77
165	0.2	0.2	0.3	11649	80.72	98.47	120.39	114.28	109.81
166	0.2	0.2	0.6	3883	44.88	48.42	65.42	63.03	61.43
167	0.2	0.2	0.6	7766	72.86	89.65	102.15	99.17	97.12
168	0.2	0.2	0.6	11649	94.03	118.30	132.40	128.63	126.38
169	0.2	0.3	0.1	3883	26.27	28.31	33.33	33.73	31.48
170	0.2	0.3	0.1	7766	51.96	60.97	64.93	59.82	54.76
171	0.2	0.3	0.1	11649	71.93	85.07	88.91	82.60	75.83
172	0.2	0.3	0.2	3883	28.98	30.35	40.32	38.52	35.80
173	0.2	0.3	0.2	7766	56.73	66.16	71.62	65.88	61.16
174	0.2	0.3	0.2	11649	75.64	91.02	96.75	89.49	83.47
175	0.2	0.3	0.3	3883	31.42	32.70	44.36	41.48	38.87
176	0.2	0.3	0.3	7766	60.20	70.54	75.87	70.27	66.18
177	0.2	0.3	0.3	11649	78.80	95.88	101.38	94.30	89.32
178	0.2	0.3	0.6	3883	36.76	45.00	52.90	50.21	48.45
179	0.2	0.3	0.6	7766	65.06	82.88	85.20	81.62	79.32
180	0.2	0.3	0.6	11649	86.75	110.02	111.87	107.68	105.01

Table A.2 Average Nusselt Number -Continued

Study Case	Dimensionless Parameters				Average Nusselt Number				
	e/H	w/H	s/H	Re_H	Element 1	Element 2	Element 3	Element 4	Element 5
181	0.2	0.6	0.1	3883	24.13	29.01	27.41	23.91	21.70
182	0.2	0.6	0.1	7766	49.78	56.94	48.55	42.14	38.43
183	0.2	0.6	0.1	11649	70.85	78.81	67.64	58.97	53.95
184	0.2	0.6	0.2	3883	25.19	31.42	29.64	26.02	23.77
185	0.2	0.6	0.2	7766	49.47	60.56	52.06	45.88	42.29
186	0.2	0.6	0.2	11649	70.68	82.82	71.60	63.54	58.85
187	0.2	0.6	0.3	3883	25.73	33.48	31.57	27.99	25.82
188	0.2	0.6	0.3	7766	49.12	63.23	54.74	48.97	45.65
189	0.2	0.6	0.3	11649	70.31	85.75	74.70	67.41	63.16
190	0.2	0.6	0.6	3883	26.82	39.38	37.00	34.01	32.25
191	0.2	0.6	0.6	7766	49.31	69.78	62.03	57.90	55.62
192	0.2	0.6	0.6	11649	70.41	93.83	83.66	78.64	75.88

Table A.3 Air properties Used in the Parametric Study

Density	1.185 [kg m^-3]
Dynamic Viscosity	1.831E-05 [kg m^-1 s^-1]
Molar Mass	28.96 [kg kmol^-1]
Thermal Conductivity	2.61E-2 [W m^-1 K^-1]
Specific Heat Capacity	1.0044E+03 [J kg^-1 K^-1]

References

[1] D. D. Luo, C. W. Leung, T. L. Chan, and W. O. Wong, "Flow and Forced-Convection Characteristics Flow Trough Parallel Plates with Periodic Transverse Ribs", Numerical Heat Transfer, Part A, Vol. 48, 2005

[2] L. T. Yeh, R. C. Chu, "Thermal Management of Microelectronic Equipment", ASME Press, New York, 2002

[3] R. Schmidt, "Challenges in Electronic Cooling-Opportunities for Enhanced Thermal Management Techniques-Microprocessor Liquid Cooled Mini-channel Heat Sink", Heat Transfer Engineering, Vol.25 (3), 2004

[4] Intel Corporation: http://www.intel.com/technology/silicon/mooreslaw/

[5] P. Rodgers, V. Eveloy, and M. G. Pecht, "Limits of Air-Cooling: Status and Challenges", 21st IEEE SEMI-THERM Symposium, 2005

[6] "Managing Power Requirements in the Electronics Industry", Electronic Cooling Magazine, December 2000

[7] A. Bejan, Allan D. Kraus, "Heat Transfer Handbook", John Wiley & Sons, 2003

[8] V. Eveloy, P. Rogers, and M.S.J. Hashmi, "Numerical Prediction Of Electronic Component Heat Transfer: An Industry Perspective", 19th IEEE SEMI-THERM Symposium, 2003

[9] K. K. Dhinsa, C. J. Bailey, K. A. Pericleous, "Turbulent Modeling And It's Impact On CFD Predictions For Cooling Of Electronic Components", Intersociety Conference on Thermal Phenomena, 2004

[10] M. Behnia, W. Nakayama, and J. Wang, " CFD Simulations of Heat Transfer From A Heated Module In An Air Stream: Comparison With Experiments And A Parametric Study", Intersociety Conference on Thermal Phenomena, 1998

[11] Y. T. Yang, and S. Yang, "Numerical Study Of Turbulent Flow in Two-Dimensional Channel With Surface Mounted Obstacle", Int. J. Heat And Mass Transfer, Vol. 37, No. 18, 1994

[12] T. J.Young, and K. Vafai, " Convective Flow And Heat Transfer In a Channel Containing Multiple Heated Obstacles", Int. J. Heat And Mass Transfer, Vol. 41, 1998

[13] V. Eveloy, J. Lohan, and P. Rodgers, "A Benchmark Study Of Computational Fluid Dynamics predictive Accuracy For Component-Printed Circuit Board Heat Transfer", IEEE Transaction On Components And Packaging Technologies, Vol. 23, No. 3, 2000

[14] J. Bredberg, L. Davidson, and H. Iacovides, "Comparison Of Near-Wall Behaviour And Its Effect On Hear Transfer For $k-\omega$ And $k-\varepsilon$ Turbulent Models In Rib-Roughened 2D Channels", 3rd Int. Symposium On Turbulence Heat And Mass Transfer, 2000

[15] K. W. Low, and, C. Yap, "Heat Transfer Coefficient For Flat And Ribbed Surface With Interrupted Heating", Electronic Packaging Technology Conference, 2000

[16] V. Eveloy, P. Rodgers, and M. S. Hashmi, "Numerical Prediction Of Electronic Component Operational Temperature: A Perspective", IEEE Transaction On Components And Packaging Technologies, Vol. 27 No. 2, 2004

[17] P. Rodgers, and V. Eveloy, "Application of Low-Reynolds Number Turbulent Flow Model To The Prediction Of Electronic Component Heat Transfer", Intersociety Conference On Thermal Phenomena, 2004

[18] K. Dhinsa, C. Bailey, and K. Pericleous, "Investigation Into Performance of Turbulence Models for Fluid Flow And Heat Transfer Phenomena In Electronic Applications", IEEE Transaction On Components And Packaging Technologies, Vol. 28 No. 4, 2005

[19] D. D. Luo, C. W. Leung, T. L. Chan, and W. O. Wong, " Flow And Forced Convection Characteristics Of Turbulent Flow Through Parallel Plates With Periodic Transverse Ribs", Numerical Heat Transfer, Part A, Vol. 48, 2005

[20] A. B. McEntire and B. W. Webb, "Local Forced Convective Heat Transfer From Protruding And Flush-Mounted Two-Dimensional Discrete Heat Sources", Int. J. Heat and Mass transfer, Vol.33, No. 7, 1990

[21] J. Hacohen, T. W. Chinu, and A. A. Wragg, "Forced And Free Convective Heat Transfer Coefficient For A Model Printed Circuit Board Channel Geometry", Experimental Thermal And Fluid Science, Vol.10, 1995

[22] B. A. Jubran, S. A. Swiety, And M. A. Hamdan, "Convective Heat Transfer And Pressure Drop Characteristics Of Various Array Configurations To Simulate The Cooling Of Electronic Modules", Int. J. Heat Mass Transfer, Vol. 39, No. 16, 1996

[23] C. W. Leung, And H. J. Kang, "Convective Heat Transfer From Simulated Air-Cooled Printed Circuit Board On Horizontal or Vertical Orientation", Int. Comm. Heat Mass Transfer, Vol. 25, No. 1, 1998

[24] Y. Wang, and K. Vafai, "Heat Transfer And Pressure loss Characterization In A Channel With Discrete Flush And Protruding Heat Sources", Experimental Heat Transfer, Vol. 12, 1999

[25] T. J. Young, And K. Vafai, " experimental And Numerical Investigation Of Forced Convective Characteristics Of Array Of Channel Mounted Obstacles", Transaction Of ASME, Vol. 121, 1999

[26] S. Chen, Y. Liu, S. F. Chan, C. W. Leung, and T. L. Chan, "Experimental Study Of Optimum Spacing Problem In The Cooling Of Simulated Electronic Package", Int. J. Heat And Mass Transfer, Vol. 37, 2001

[27] S. Y. Yoo, J. H. Park, and M. H. Chung, "Local Heat Transfer Characteristics In Simulated Electronic Modules", Transaction Of The ASME, 2003

[28] ANSYS-CFX User Manual Version 10.0

[29] L. Davidson, "An Introduction to Turbulence Models", CHALMERS, 2003

[30] W. Vieser, T. Esch, and F. Menter, "Heat Transfer Predictions Using Advanced Two-Equation Turbulence Models", CFX Technical Memorandum, CFX-VAL10/0602, 2002

[31] Fluent User Manual Version 6.0

[32] D. C. Wilcox, "Turbulence modeling for CFD", DCW Industries Inc., 1994

[33] H. K. Versteeg, and W. Malalasekera, "An introduction to computational fluid dynamics", Pearson Education Limited, 1995

[34] F. R. Menter, "Improved Two-Equation $k-\omega$ Turbulent Models for Aerodynamic Flows", NASA Technical Memorandum 103975, 1992

[35] F. R. Menter, "Influence of Free stream Values on $k-\omega$ Turbulence Model Predictions", AIAA Journal, Vol. 30, No. 6, 1992

[36] Y. Nagano, H. Hattori, T. Houra, "DNS of velocity and thermal fields in turbulent channel flow with transverse-rib roughness", International Journal of Heat and Fluid Flow, Vol.25, 2004

[37] J. D. Wolf, "Measurements of the Heat Transfer Coefficient Distribution On Flat and Ribbed Surfaces with Interrupted Heating Using Thermo chromic Liquid Crystals", B.S. Thesis, United States Air Force Academy, University of California Davis, 1998

[38] T. J. Young, K. Vafai, "Experimental and Numerical Investigation of Forced Convection Characteristics of Array of Channel Mounted Obstacles", Transaction of ASME, Vol. 121, 1999

[39] E. R. Meinders, K. Hanjalic, and R. J. Martinuzzi, "Experimental Study of the Local Convection Heat Transfer From A Wall-Mounted Cube In Turbulent Channel Flow", Transaction of ASME, Journal of Heat Transfer, 1999

[40] T.M. Liou, J.J. Hwang, and S.H. Chen, "Simulation and Measurement of Enhanced Turbulent Heat Transfer in a Channel with Periodic Ribs on One Principal Wall", Int. J. Heat Mass Transfer, Vol. 36, 1993

[41] R. L. Simpson, "Turbulent Boundary-Layer Seperation", Annual Review Fluid Mechanics, 1989

[42] ANSYS-CFX Technical brief," Innovative Turbulence Modeling: SST Model in ANSYS-CFX", TS05May_CFX_SST

[43] P. K. Kundu, "Fluid Mechanics", Second Edition, Academic Press, 2002

[44] D. M. Bourg, "Excel Scientific and Engineering Cookbook", O'Reilly, January 2006

[45] J. H. Lau, C. P. Wong, J. L. Prince, W. Nakayama, "Electronic Packaging: Design, Materials, Process, And Reliability", McGraw-Hill, 1998